THE UNIVERSITY of EDINBURGH

| | |
|---|---|
| **Title** | Physical properties and composition of vega-type disks |
| **Author** | Sheret, Ian |
| **Qualification** | PhD |
| **Year** | 2004 |



**Digitisation Notes:**

- Pages iv, 20, 96, 112 are blank - not scanned

# The Physical Properties and Composition of Vega-Type Disks

Ian Sheret

Institute for Astronomy
School of Physics


University of Edinburgh
Doctor of Philosophy

February 2004

# Abstract

Vega excess stars are main sequence stars which are surrounded by a cool dust disk, left as a remnant of the massive disk produced early in the star's formation. Vega-type disks are typically optically thin, contain little or no gas, and are roughly 100 AU in radius with a cleared region close to the star. This thesis presents a programme of observational studies which aimed to determine the basic physical properties of nearby Vega-type disks, and the detailed modelling and analysis that were required to interpret these observations.

The first part of the thesis presents new sub-mm observations of Vega excess stars, and modelling for all known Vega excess stars which have sub-mm data, using dust grain models with realistic optical properties. Analysis of the resolved targets showed that different objects require very different dust grain properties in order to simultaneously fit the image data and spectral energy distribution (SED). Fomalhaut and Vega require solid dust grains, whilst HR4796 and HD141569 can only be fitted using porous grains. The older stars tend to have grains which are less porous than younger stars, which may indicate that collisions in the disks have reprocessed the initially fluffy grains into a more solid form. $\epsilon$ Eri appears to be deficient in small dust grains compared to the best fitting model, which may be due to factors which affect the size distribution of grains close to the radiation pressure blowout limit. When the model is applied to the unresolved targets, an estimate of the disk size can be made. However, the large diversity in dust composition for the resolved disks means that it is impossible to make a reliable assumption as to the composition of the grains in the unresolved disks, and there is a corresponding uncertainty in the estimated disk size. In addition, the poor fit for $\epsilon$ Eri shows that the model cannot always account for the SED even if the disk size is known. These two factors mean that it may not be possible to determine a disk's size without actually resolving it.

The second part of the thesis describes mid-IR observations designed to directly resolve the disks around several nearby main sequence stars, and hence obtain a direct

measurement of the disk size. An analytical model of the telescope point spread function (PSF) was developed and fitted to observations of standard stars, and this model was used to establish whether the science observations were consistent with a point source, or if they showed evidence for a resolved disk. Though the observations failed to resolve any of the targets, techniques were developed to reduce imaging data of marginally resolved disks, and the observations have provided a clearer idea of what is required for a successful program in the future. The key requirements are regular monitoring of the PSF (i.e. interleaved PSF star observations), a high quality flatfield and fairly narrow band filters. In addition, 20 $\mu$m observations are probably needed in most cases. Ultimately, the technique is limited by the stability of the PSF, and on the difference in colour between the PSF star and the debris disk.

Finally, in the third part of the thesis I present the results of a search for molecular hydrogen using MICHELLE, the mid-IR echelle spectrometer at the UK Infrared Telescope. The aim of these observations was to investigate the controversial *ISO* detection of $H_2$ around Vega excess stars, as reported by Thi et al. (2001, Nature, v. 409, p. 60). Due to weather constraints, the observations focused on two pre-main sequence stars, AB Aur and CQ Tau. No significant emission lines were detected from either star, and the upper limits on line flux were significantly smaller than those measured from the *ISO* observations, which suggests that the emission detected by *ISO* is extended on scales of at least 6 arcsec, and does not come from the disk as previously thought. This result indicates that the *ISO* detection of large amounts of $H_2$ in Vega-type disks may also be unreliable, and further observations are needed to determine their true gas content.

# Declaration

I declare that this thesis is not substantially the same as any that I have submitted for a degree or diploma or other qualification at any other University. I further state that no part of my thesis has already been or is being concurrently submitted for any such degree, diploma or other qualification.

This thesis is the outcome of my own work except where specifically indicated in the text.

Ian Sheret
Edinburgh,
February 2004.

# Acknowledgements

My supervisors Mark Wyatt, Bill Dent and Peter Brand are undoubtedly the people I must thank most for their work and time over the last three years. Their encouragement, enthusiasm and sound advice are what made this PhD a success, and I'm very grateful. I'd also like to thank Suzie Ramsay for inviting me to work on the the $H_2$ observations of AB Aur and CQ Tau, and encouraging me to write the work up in a paper. Alistair Glasse and the staff at the JAC provided essential support for the observations, and I'd particularly like to thank Jim Hodge for showing me the sights from the top of the JCMT, and for remaining remarkably calm whilst teaching me to drive on Mauna Kea: in my defence, that particular vehicle had four pedals and no hand-brake.[1]

The Royal Observatory has been a great place to work, and lots of people have contributed to that. My fellow students are an amazing set of people and spending time with them has been mind and soul expanding, albeit likely to leave me with a hangover. Staff and students alike have been endlessly helpful whenever I've needed advice or encouragement, or distraction from my own work. I'd particularly like to thank Alan Heavens for two acts of kindness: firstly for explaining how to estimate the uncertainty on a weighted mean, and secondly for giving me a lift to pick up my passport when the door staff wouldn't let me into the pub to celebrate Ali Higgins passing his viva, on the grounds that I didn't look like I was eighteen. With even greater heroism, indeed despite seemingly insurmountable obstacles, Ben Panter obtained a comfortable office chair for me, without which this work may never have been completed.

I've got lots of friends in Edinburgh, but ultimately my flatmates Dan Burkey and Olivia Johnson are the ones who made my stay here such a good time. Being able to go to the pub, the absence of soap opera, these are things I think I'll always look back

[1] Determining the technique required to set off in such a vehicle whilst on an upward incline is left as an exercise to the reader; my only advice is that you don't pull up too closely behind someone who is about to test their solution.

on and smile.

For the last six months of writing up I've been working at the Leeds astronomy department, scavenging off their computing (and indeed seating) resources, and generally being a nuisance. Though there's been no good reason to put up with me, everyone has been extremely friendly and welcoming and I've been made me feel as if I'm part of the department. This is especially surprising given that I turned up at the start of September asking if I could use a terminal and claiming that I'd be done in a few weeks (I should make it clear that this was a genuine heartfelt delusion, I wasn't merely being dishonest).

Finally, I'll mention my wife and family. Though they haven't contributed much to my work over the last three years, they've contributed a lot to everything else, and I know which of the two is more important.

# Contents


**1 Introduction** **1**

1.1 Planet formation and circumstellar disks . . . . . 1

1.2 Vega excess disks . . . . . 2

1.2.1 Discovery of the Vega excess phenomenon . . . . . 2

1.2.2 Continuous dust creation . . . . . 3

1.2.3 Definition of a Vega excess star . . . . . 4

1.3 Stars, planets, and the Vega phenomenon . . . . . 5

1.3.1 Star formation in molecular clouds . . . . . 5

1.3.2 Planet building in a circumstellar disk . . . . . 6

1.3.3 Grain growth in pre-main sequence star disks . . . . . 8

1.3.4 Extra-solar planets . . . . . 9

1.4 Surveys for Vega excess stars . . . . . 10

1.4.1 IRAS surveys . . . . . 10

1.4.2 ISO surveys . . . . . 11

1.4.3 Survey results . . . . . 11

1.5 Techniques for observing dust disks . . . . . 12

1.5.1 Scattered light coronography . . . . . 12

1.5.2 Mid-IR photometry and imaging . . . . . 13

1.5.3 Sub-millimetre single dish photometry and imaging . . . . . 15

1.5.4 Millimetre and sub-millimetre interferometry . . . . . 17

1.6 Observations of gas in debris disks . . . . . 17

1.7 Morphology of Vega-type disks . . . . . 18

1.8 Overview of thesis . . . . . 19

**2 Theory of dusty circumstellar disks** **21**

2.1 Introduction . . . . . 21

2.1.1 Overview of a dusty disk . . . . . 21
2.2 Dynamics in a dust disk . . . . . 22
2.2.1 Orbits due to gravity and radiation pressure . . . . . 22
2.2.2 Blowout diameter . . . . . 23
2.2.3 Poynting-Robertson drag . . . . . 24
2.2.4 Gas drag . . . . . 24
2.2.5 Other forces . . . . . 26
2.3 Grain size distribution and the collisional cascade . . . . . 26
2.3.1 Collisionally dominated vs. PR dominated disks . . . . . 27
2.4 Dust grain optical models . . . . . 28
2.4.1 Calculating the optical properties of a dust grain . . . . . 29
2.5 Thermal emission from a dust disk . . . . . 30
2.5.1 Temperature of a dust grain . . . . . 30
2.5.2 Observable emission . . . . . 32

**3 Sub-mm observations and modelling 35**
3.1 Introduction . . . . . 35
3.2 Observations . . . . . 36
3.3 Data reduction . . . . . 40
3.3.1 Maps . . . . . 40
3.3.2 Photometry data . . . . . 44
3.4 Results . . . . . 46
3.5 SED modelling . . . . . 49
3.5.1 Photometric data . . . . . 49
3.5.2 Dust grain properties . . . . . 49
3.5.3 Size distribution . . . . . 52
3.5.4 Spatial distribution . . . . . 52
3.5.5 Stellar parameters . . . . . 52
3.5.6 Modelling method . . . . . 53
3.6 Modelling results . . . . . 56
3.6.1 Fomalhaut . . . . . 56
3.6.2 HR4796 . . . . . 56
3.6.3 $\epsilon$ Eri . . . . . 58
3.6.4 Vega . . . . . 59
3.6.5 $\beta$ Pic . . . . . 62

3.6.6 HD141569 . . . . . 63
3.6.7 HD109085 . . . . . 65
3.6.8 HD38393 . . . . . 65
3.6.9 $\sigma$ Boo . . . . . 66
3.6.10 HD48682 . . . . . 67
3.6.11 HD207129 . . . . . 69
3.7 Discussion . . . . . 69
3.8 Conclusion . . . . . 71

**4 Mid-IR imaging of debris disks** **73**
4.1 Introduction . . . . . 73
4.2 Selection criteria . . . . . 74
4.3 Observations . . . . . 76
4.3.1 Observation details . . . . . 76
4.3.2 Observing method . . . . . 78
4.4 Data reduction . . . . . 80
4.4.1 Flatfielding mid-IR arrays . . . . . 80
4.4.2 Method . . . . . 82
4.5 Analysis . . . . . 85
4.5.1 PSF model . . . . . 86
4.5.2 Determining the final PSF model . . . . . 88
4.5.3 Fitting the science targets . . . . . 88
4.6 Results . . . . . 89
4.7 Discussion . . . . . 91
4.8 Conclusion . . . . . 95

**5 Observations of $H_2$ in circumstellar disks** **97**
5.1 Gas in young and old disks . . . . . 97
5.2 Observations and data reduction . . . . . 99
5.3 Results . . . . . 103
5.4 Discussion . . . . . 104

**6 Conclusion** **107**
6.1 Future observations . . . . . 108
6.2 Future theory . . . . . 109
6.3 Final word . . . . . 110

# Chapter 1

# Introduction

## 1.1 Planet formation and circumstellar disks

Planet formation is a key problem for modern science. An understanding of the planet formation process is needed both to explain the origin of our solar system, and to understand the formation of planetary systems around stars other than the Sun. Ultimately, the existence of life in the universe depends on the details of planet formation: how likely planet formation is, what type of planets are formed, and in what types of orbits.

Investigations of our own solar system have produced a 'standard model' of how planet formation occurred. However, planet formation is a stochastic process and there is good reason to believe that the final outcome of other planetary systems could be wildly different, even if they start from very similar initial conditions. The only way to fully understand planet formation is by observing many different systems. In recent years, it has finally become possible to detect certain types of planet around other stars, and in the next decade this capacity will increase to the point where Earth-like planets will become detectable. This will answer the question of how common planets are, what types of system are formed, and whether they are suitable for life. The significance of these developments can hardly be overstated, but knowing the final state of nearby planetary systems will not reveal everything we want to know about the planet formation process itself.

The next crucial step will be to extend our specific picture of planet formation in the solar system into a general picture of planet formation in the galaxy, and to do this

we must observe the process of planet formation in action. Observing nascent planetary systems give us the opportunity to get direct information on planet formation, and determine the timescale and relative importance of different processes. Such observations also allow us to examine the effect that the star formation environment has on the planet formation process, and how planetary systems evolve in the immediate aftermath of their formation.

The work in this thesis is mainly concerned with Vega excess stars. These are main sequence stars that are surrounded by a debris disk of dust and solid bodies, left over from the formation of the star. These systems provide some of the best evidence that the processes which produced planets in our system are also at work around other nearby stars. Though observations of these dust disks are challenging, understanding the Vega excess phenomenon has the potential to provide insights into planet formation that no other method can access. These debris disks are the fossil record of the events which took place around the star during its formation, and their existence is intimately linked with the planet formation process. In addition, the gravitational effects of any planets embedded in the disk can cause perturbations in the dust distribution that may be easier to detect than the planets themselves.

The purpose of this chapter is to give an overview of the Vega excess phenomenon in the context of star and planet formation, and describe the observational tools that can be used to probe dust disks around nearby stars.

## 1.2 Vega excess disks

### 1.2.1 Discovery of the Vega excess phenomenon

In 1983 the IRAS satellite was launched, with a mission to survey the entire sky in four IR bands from 12 to 100 $\mu$m. However, early in the mission a routine calibration observation of Vega revealed a large excess at 60 and 100 $\mu$m, an order of magnitude brighter than expected from the star's photosphere alone (Aumann et al. 1984). The only plausible explanation was that Vega was surrounded by orbiting dust grains, the first such discovery for a star which was not very young or undergoing mass loss. Aumann et al. argued that the dust was a remnant from the formation of the star, and that the dust must be far larger than interstellar dust grains in order to survive into the main sequence lifetime of Vega. Here then was the first evidence for large, solid material orbiting a star other than the Sun, and proof that the processes which led to planet formation in our own solar system was also at work around nearby stars.

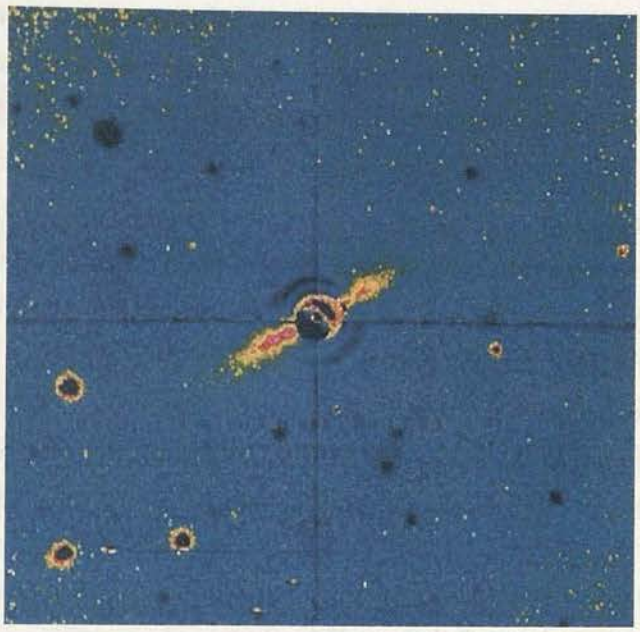

**Figure 1.1:** The first image of $\beta$ Pic's dust disk, from Smith and Terrile (1984).

The initial discovery was confirmed by Kuiper Airborne Observatory measurements (Harvey et al. 1984), and soon IRAS observations detected similar IR emission around three other main sequence stars: Fomalhaut, $\beta$ Pic and $\epsilon$ Eri (Gillett 1986). This confirmed that the Vega excess was not due to a spurious background source, and that the phenomenon was in fact commonplace. After the announcement of the excess from $\beta$ Pic, coronagraph observations made using an instrument designed for observing planetary rings provided dramatic evidence that $\beta$ Pic's dust was in an edge-on disk (Smith and Terrile 1984, Figure 1.1). This flat geometry was further evidence for the link with our solar system, and Smith and Terrile suggested that the $\beta$ Pic disk was a site for ongoing or recent planet formation.

### 1.2.2 Continuous dust creation

A key aspect of the Vega phenomenon is that the dust cannot simply be left over from the formation phase of the star, but in fact must be created continuously. This is because the timescale for removal of the dust grains by radiation forces is often significantly less than age of the star (Section 2.2.3). This shows that the dust grains must have been created recently, and implies that dust production is a continuous process.

There are two models to explain the continuous dust creation observed in Vega-

type disks: collisional dust production, or emission of dust grains by evaporating comets (Weissman 1984). In the first model, small dust grains are created by collisions between larger bodies (Artymowicz 1989, 1997). In systems like $\beta$ Pic, this mode of dust creation is inevitable: the amount of material in the disk ensures that collisions are frequent, and the high collisional velocity (inferred from the vertical thickness of the disk) means that these collisions must be destructive. Unfortunately, for most other debris disks the collisional velocity is unknown, and so the amount of dust created in collisions cannot be determined with complete confidence.

The alternative to collisional dust production is that dust is produced by sublimation of comet like bodes (Harper et al. 1984; Knacke et al. 1993; Lecavelier Des Etangs et al. 1996). This model has the advantage that it also predicts the release of gas into the disk, as observed around $\beta$ Pic (see Section 1.6). However, for systems like Fomalhaut and $\epsilon$ Eri, the solid material is too cool for sublimation to be an efficient process.

It is actually quite possible that both mechanisms are important to varying degrees in different systems. For example, interplanetary dust in the solar system is a mixture of dust from asteroid collisions and comets, with both sources making a significant contribution (Dermott et al. 1996).

### 1.2.3 Definition of a Vega excess star

The basic observational definition of a Vega excess star is a main sequence star (i.e. MK luminosity class V) with IR excess due to circumstellar dust. Vega excess disks differ markedly from the disks found around very young stars (T-Tauri and HAeBes) in that they tend to have low gas content, with total gas mass similar or less than the dust mass, whereas young stellar disks have a composition that is similar to ISM, i.e. 100 times more gas than dust. Also, Vega excess disks tend to be optically thin to radiation from the central star, unlike T-Tauri and HAeBe disks. This results in a low IR excess luminosity, usually less than about 1% of the stellar luminosity. Inevitably, there will be some overlap between the Vega excess class and the T-Tauri/HAeBe class, as these objects are thought to form an evolutionary sequence, so in cases where it is not clear which class a particular object is in, the term 'transition object' can be used.

Though the above criteria are observational, they have important implications for the physical processes which are taking place in the disk. Low optical depth means that starlight penetrates the whole of the disk, so radiation forces affect all of the dust grains. Low gas content means that the collisional velocity between dust grains will not

be damped by gas drag, allowing destructive collisions to occur. Broadly, we can say that Vega excess stars are surrounded by debris disks, which have left the constructive (i.e. planetesimal building) phase of their evolution, and entered a destructive phase.

## 1.3 Stars, planets, and the Vega phenomenon

Perhaps the most fundamental question about Vega-type disks is what their formation mechanism is. This question has been partly answered by our understanding of star formation: circumstellar disks are very common around young stars, and it seems that Vega-type disks are the remnants of these young disks. The second key question concerns the origin of the small dust grains in Vega disks, which require the existence of large parent bodies. In this case, a potential answer comes from the theory of planet formation, which requires the formation of large solid bodies as a stepping-stone to the formation of planets. Though the details of Vega disk formation and dust production are still unresolved, it seems that both star formation theory and planet formation theory must be included in our picture of Vega excess disks.

### 1.3.1 Star formation in molecular clouds

The current paradigm of star formation is that stars form by gravitational collapse in molecular clouds (Shu et al. 1987). The process begins in dense clumps within the molecular cloud, which are supported by magnetic fields and turbulence. Gradually, the neutral atoms and molecules slip relative to the magnetically supported ions, and the core undergoes gravitational collapse. This collapse occurs 'inside out', which means that material near the centre of the core collapses quickly, while outlying material rains down over a longer period. A small protostar forms at the centre of the core, supported by its own pressure; this protostar will gradually gain mass from the in-falling material. Due to rotation within the original clump, the gas and dust falling inwards have some transverse velocity and will fall in on a parabolic path. This material will form a disk, and practically none of it will fall straight onto the protostar. The disk will therefore gain material much more quickly than the protostar. This quickly becomes an unstable situation. Disks need to be stabilised by a more massive central object or else they will become 'self gravitating' (Adams and Lin 1993). If this happens, any small density fluctuation will start a density wave in the disk. The tidal interaction between the disk and the star will then transport a lot of angular momentum outwards, and the protostar can then gain enough mass to stabilise the disk again. This is therefore a

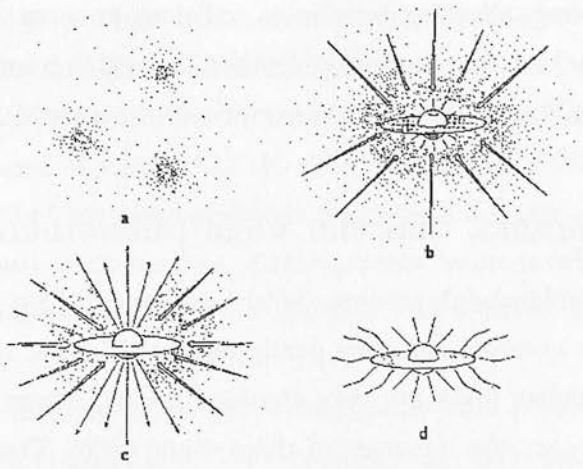


**Figure 1.2:** Schematic of star formation, from Shu et al. (1987). a) Clump in the molecular core collapses under its own gravity. b) Infalling material forms a disk around the protostar. c) Stellar wind breaks out at the poles. d) Inflow is completely halted by stellar wind, leaving a T Tauri star.

self-regulating mechanism. If the disk becomes too massive, the rate of mass transport will increase to compensate. When the in-fall is halted by the stellar wind, we will be left with a star surrounded by a less massive disk (Figure 1.2).

A wealth of observations support the existence of disks around newly formed stars. For low mass stars (F type and cooler), the star will become visible as a T Tauri object, typically with an IR excess due to thermal emission from the disk, and variability and emission lines due to continuing accretion from the disk. For higher mass stars, a Herbig Ae/Be star will be produced, also known as a HAeBe. Observations of these objects are more difficult, however there is now good evidence that these stars also have disks, at least in the case of Herbig Ae stars (e.g. Piétu et al. 2003).

### 1.3.2 Planet building in a circumstellar disk

The current theory of planet formation is based on the idea that planets form by the gradual accretion of dust grains into larger and larger bodies within a circumstellar disk, and so this model automatically produces the comet and asteroid type bodies required for Vega-type disks. This theory comes almost entirely from observations of our own solar system, simply because data from elsewhere have not been available until very recently. Already it is apparent that the basic model may not be able to account for the observed properties of extrasolar planets, but the theory of planet formation outlined below is extremely successful in explaining the detailed observed properties of

our solar system, and it is likely to be the basis of extrasolar planet formation theories, at least for certain types of extrasolar planet. A review of current planet formation theory is given by Lissauer (1993), see also de Pater and Lissauer (2001) and Mannings et al. (2000).

The key observational constraints for any theory of planet formation are given by the current observed state of the solar system (Lissauer 1993). Four terrestrial planets and four gas giants must be formed, most with satellite systems, plus the asteroid belt, the Kuiper belt (including the Pluto-Charon system), and short and long period comets. The planets must all have prograde orbits which are nearly circular and coplanar and have gradually increasing separation, and should be in the same direction as the Sun's rotation. Planetary rotation must be somewhat random in orientation and speed, though with a bias towards the prograde direction. The observed composition, mass, and density of all these bodies must be explained, as well as the surface features of the planets, including the cratering record. Laboratory analysis of material from the Earth, Moon and meteorites has revealed isotopic composition, and radioactive clocks put constraints on the timescale of various different stages of planet building, which must also be accommodated (Grady 2003). Finally, in theories which couple the formation of the planets to the formation of the Sun, certain solar properties must also be explained, in particular the Sun's low angular momentum in comparison to the planets.

The only theory which can presently explain all these facts is the planetesimal accretion model (Hayashi et al. 1977, and references therein). In this model, planet formation begins with sub-micron sized dust grains, which collide and stick together in the disk surrounding a newly formed star. Close to the star, the dust grains are primarily silicates and iron compounds, but at larger distances ices can also condense out of the gas. Gas drag and inelastic collisions cause the dust grains to settle out to the mid-plane of the disk, greatly increasing the collision rate (Weidenschilling 1980). As particles continue to collide and stick, large fluffy dust grains are produced, held together by van der Waals forces (Beckwith et al. 2000). Grain growth will continue in this fashion until kilometre sized bodies are formed. At this point gravitational forces become important, increasing the number of collisions, and also helping to hold the planetesimal together. Because of the gravitational focusing effect, the largest planetesimal in a region of the disk can accrete matter more efficiently than all other planetesimals. This phenomenon is called runaway growth, and leads to one large planetesimal dominating each radial section of the disk. At this stage, collisions and

gravitational interactions between very large planetesimals occur, and these determine the final state of the solar system.

The outer planets have access to ices during their formation, which can provide much more mass than the rocky grains which form the terrestrial planets, so they become more massive. In addition, Jupiter and Saturn have enough mass to trap large amounts of gas from the disk (Mizuno 1980). Once the planets have formed, the remaining gas is removed from the disk. The exact process which removes the gas is not clear, but candidates include photoevaporation caused by light from the central star or nearby massive stars, viscous accretion onto the star, or removal by the stellar wind (Hollenbach et al. 2000).

### 1.3.3 Grain growth in pre-main sequence star disks

The dense, dusty disks observed around pre-main sequence stars should be the perfect environment for planetesimal building, so a key question is whether the process of grain growth can be detected in T Tauri and HAeBe disks. Some evidence for grain growth can be found from the spectral energy distribution (SED) of these stars, in particular the spectral index of dust thermal emission at millimetre and sub-mm wavelengths (Beckwith and Sargent 1991; Mannings and Emerson 1994; Koerner et al. 1995). Here, the slope of the emission spectrum depends strongly on the size of the dust grains, as larger dust grains are more efficient emitters at these wavelengths. However, other parameters such as the temperature and surface density profile of the disk can also affect the sub-mm spectral slope, so such measurements cannot conclusively detect grain growth (Beckwith et al. 2000). Other evidence for grain growth in pre-main sequence disks comes from the optical and infrared images of disks silhouettes in the Orion Nebula. Dust disks become more transparent at longer wavelengths, but this effect depends of the size of the dust grains, so measuring the size of a disk at different wavelengths can constrain grain size (Throop et al. 2001; Shuping et al. 2003). However, due to the small size of the disks (the largest is only $\sim$ 2 arcsec in diameter) these measurements are extremely challenging, and the evidence for grain growth is not conclusive.

Grain growth can also be inferred from mid-IR spectroscopy of silicate emission bands (van Boekel et al. 2003; Przygodda et al. 2003). The width of a feature depends on the size of the dust grains that produce it, though unfortunately the grain composition also affects the width. There is evidence for an inverse correlation between the strength of silicate features and their width, which is most easily explained by grain growth, as

larger grains naturally have weaker silicate emission.

### 1.3.4 Extra-solar planets

In the last decade, over 100 extrasolar planets have been discovered using the Doppler-wobble technique (Marcy and Butler 1998, and references therein). The observed properties of these planets have proved extremely surprising: many of the planets have a mass similar to Jupiter, but are much closer to their star than the giant planets in our solar system, with orbital periods of only a few days. In addition most planets have quite eccentric orbits, unlike the nearly circular orbits of the solar planets. These observations present significant problems for existing planet formation theory, which predicts that planets should not form close to the star, and should not have elliptical orbits (Bodenheimer and Lin 2002). The key question is therefore how did these planets form? If they formed in a similar way to the gas giants in our system (i.e. planetesimal accretion followed by gas capture), then it seems that they must have undergone migration to gain their current orbital parameters (Lin et al. 1996). The alternative hypothesis is that the observed extrasolar planets formed by an entirely different process, i.e. gravitational collapse during the formation of the star, or fragmentation of a massive circumstellar disk due to gravitational instability. These processes are attractive because they can naturally produce eccentric orbits, though the gravitational collapse scenario seems to be unable to produce planets of less than about 10 Jupiter masses (Adams and Benz 1992; Boss 1997). As well as a mechanism for forming extra-solar planets, the disk fragmentation model has been put forward as a possible formation mechanism for the Jupiter and the other gas giants in our solar system, with subsequent photoevaporation from nearby OB stars removing most of the hydrogen from Uranus and Neptune (Boss 2003).

A particularly interesting topic is the relationship between extrasolar planets and debris disks. Unfortunately, very few stars with a planet also have a debris disk. This is at least partly due to the selection biases involved: debris disks tend to be found around hot A type stars because their high luminosity makes the dust easier to detect, whereas extrasolar planets are only found around cool stars because the narrow lines in their spectra are essential for radial velocity studies. In addition, disks are more prevalent around young stars, but these stars tend to be more active, making radial velocity measurements more difficult. The one exception is the cool (K2V) star $\epsilon$ Eri, which has both a debris disk and a planet with a mass of around one Jupiter mass and a semi-major axis of 3.4 AU (Hatzes et al. 2000).

## 1.4 Surveys for Vega excess stars

### 1.4.1 IRAS surveys

Since the discovery of the Vega excess phenomenon in 1984, many searches for stars with IR excess have been undertaken, and most of these have been based on the IRAS all sky survey. Two point source catalogues were produced from the IRAS data, the Point Source Catalog (PSC, Beichman et al. 1988a) and the Faint Source Catalog (FSC, Moshir 1989). The difference between the two arises from the way that sources were detected in the data. IRAS scanned the sky in strips, and the survey was designed so that each point in the sky was scanned several times. For the FSC, the data from all scans were coadded before source detection was attempted, whereas for the PSC a source had to be bright enough to be detected in a single scan. The PSC is more reliable, i.e. it contains almost no spurious detections, but the FSC is about 2.5 times more sensitive, though up to 5% of the detections may be spurious. Both catalogues give broad band fluxes in four bands (12, 25, 60 and 100 $\mu$m).

Several different surveys have been made to find Vega excess stars in the IRAS catalogues. Walker and Wolstencroft (1988) searched the PSC by cross correlating the SAO catalogue and the Catalog of Nearby Stars (Gliese 1969). They looked for candidates with 60:100 $\mu$m colours similar to the prototype Vega excess objects, and which were spatially resolved in at least one band. These strict criteria produced 34 candidates (including the four prototypes), though only about half of these are known to be main sequence stars. Subsequent surveys have tended to drop the requirement for extended emission, and have looked for stars with excess emission in any band (Stencel and Backman 1991; Oudmaijer et al. 1992). Mannings and Barlow (1998) focused specifically on finding main sequence stars with an IR excess by using the luminosity class information from the Michigan Spectral Catalog (MSC). This was a very successful approach which found many new candidates, partly because of the survey used the more sensitive IRAS FSC rather than the PSC. Unfortunately, the MSC only covered about half of the sky at the time, which limited the number of systems detected. More recently, the 2MASS Point Source Catalog has been used to search for main sequence stars with an excess at 12 $\mu$m (Fajardo-Acosta et al. 2000), and eight possible examples were found.

### 1.4.2 ISO surveys

The Infrared Space Observatory (ISO) was launched in 1995, and operated until 1998. ISO did not make an all sky survey but instead made pointed observations, and several projects aimed to look for Vega excess stars. Because of the improved detectors and longer integration times, ISO surveys have the potential to be much more sensitive than surveys of the IRAS data.

A key aim of the ISO surveys was to examine the evolution of circumstellar disks. Habing et al. (2001) observed a sample of nearby main sequence stars at 60 and 170 $\mu$m, having carefully estimated the age of the stars using a variety of means. They found a significant difference in disk frequency between young and old stars, and concluded that most stars reach the main sequence with a disk, but by 400 Myr most of these disks are gone. Spangler et al. (2001) concentrated on finding disks within groups of stars, primarily young open clusters. This has the advantage that the age of a cluster can be determined much more accurately than the age of an individual star, but the disadvantage that typical targets are more distant than stars in the Habing et al. sample. Robberto et al. (1999) also looked at groups of stars, but were unable to detect disks around stars older than about 10 Myr. However, their results did confirm that the disk fraction around stars younger than 10 Myr is high.

Two surveys looked for warm disks around main sequence stars by searching for an excess at 25 or 20 $\mu$m (Laureijs et al. 2002; Fajardo-Acosta et al. 1999, respectively). Both surveys found that excess emission at 20–25 $\mu$m is rarer than at 60 $\mu$m, with Laureijs et al. detecting disks around only 6% of their sample. Fajardo-Acosta et al. detected disks around 14% of their sample stars, but according to Laureijs et al. these detections are inconclusive and require further confirmation.

### 1.4.3 Survey results

When trying to determine the statistical properties of the Vega excess population, the difficult problem is not simply finding objects, but finding objects within a well defined sample. The survey with the most rigorously defined sample is Habing et al. (2001), who examined only stars which were close and bright enough for the photosphere to be detected at 60 $\mu$m. The primary results of this paper are that about half of all stars younger than 400 Myr have a disk, whereas for stars older than 400 Myr this fraction falls to one in ten. Overall 17% of the sample were detected. The existence of a sharp cutoff at 400 Myr is controversial, and Spangler et al. (2001) did not find

this effect, instead finding a smooth decrease in disk flux with time. The origin of the 400 Myr timescale may be that Habing et al. choose the photospheric flux as the limit of their search. Choosing the photospheric flux as the cutoff for detecting a disk is a reasonable thing to do (in particular it make disks around different temperature stars equally detectable), but there is actually nothing special about this value. If a deeper search were undertaken, it seems likely that the number of disks detected would increase. This suggests that the 400 Myr timescale may be the timescale for disk flux to fall below photospheric flux, and not really the timescale for disk removal.

A surprising result from the Habing et al. survey is that a significant number of very old (i.e. $> 5$ Gyr) stars had detectable disks. This effect was noted by Greaves and Wyatt (2003), who showed that disks can survive for the entire main sequence lifetime of a star, regardless of the star's spectral type. However, accurate age estimates for individual stars are difficult to obtain, particularly for cool stars (i.e. G stars and cooler), so the statistics for the incidence of old stars with a disk may be unreliable.

## 1.5 Techniques for observing dust disks

### 1.5.1 Scattered light coronography

Scattered light imaging of Vega-type disks is extremely challenging, due to the huge contrast between the bright central star and the faint disk, and some form of coronagraph is needed in all cases. However, the excellent resolution possible with this technique makes the images particularly useful when they can be obtained. The first disk to be detected in scattered light was $\beta$ Pic (Smith and Terrile 1984). This image provided the first evidence that the material around Vega excess stars is in a disk rather than some other configuration. Since then, highly detailed scattered light images of $\beta$ Pic's disk have been obtained using the Hubble Space Telescope (Burrows et al. 1995; Heap et al. 2000) and ground based observations (Paresce and Burrows 1987; Golimowski et al. 1993; Lecavelier Des Etangs et al. 1993; Mouillet et al. 1997a; Larwood and Kalas 2001). The most interesting discovery from these images is that there is an inclined component to the disk, with an angle of about 4° and a radius of around 80 AU. The origin of this component is unclear, but Heap et al. (2000) suggest the observations are consistent with the disk being perturbed by a planet, as does Augereau et al. (2001).

Only two other Vega-type disks have been successfully imaged in scattered light: HD141569 and HR4796. HR4796 has been imaged with NICMOS on the HST (Schneider et al. 1999), whilst HD141569 has been observed with three different HST instru-

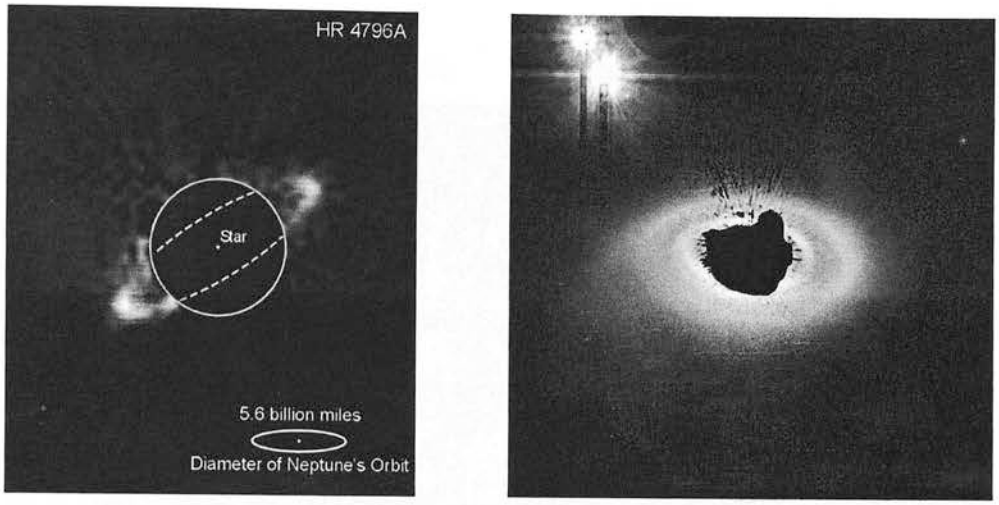


**Figure 1.3:** HST images showing scattered light from two debris disks. On the left is HR4796 imaged with NICMOS (Schneider et al. 1999), and on the right HD141569 imaged with ACS (Clampin et al. 2002).

ments, NICMOS (Augereau et al. 1999a; Weinberger et al. 1999), STIS (Mouillet et al. 2001) and ACS (Clampin et al. 2003), plus some ground based imaging using adaptive optics (Boccaletti et al. 2003). As for $\beta$ Pic, the most interesting features of the HD141569 images are asymmetries in the disk. However, for HD141569 the cause of the asymmetries is somewhat clearer: the ACS image shows that the disk is interacting with a nearby companion star, causing a spiral density wave in the disk. The NICMOS image of HR4796 and the ACS image of HD141569 are shown in Figure 1.3.

### 1.5.2 Mid-IR photometry and imaging

Until quite recently, mid-IR (i.e. 10–20 $\mu$m) observations of Vega-type disks were limited to basic ground based photometry (Sylvester et al. 1996; Fajardo-Acosta et al. 1998), and some low resolution imaging of the largest disks with ISO (Fajardo-Acosta et al. 1997; Heinrichsen et al. 1999; Walker and Heinrichsen 2000) However, with the introduction of sensitive mid-IR array detectors in the last few years, mid-IR imaging has become a particularly fruitful area. Ground based observations are severely limited by the transmission of the Earth's atmosphere, but in good conditions imaging is possible at 10 and 20 $\mu$m. At these wavelengths, thermal emission from a disk can be as bright or brighter than the photospheric emission, so coronographic techniques are not needed. In addition, a 4 or 8 meter class telescope with basic tip/tilt correction can be diffraction limited at these wavelengths, allowing sub-arcsec resolution imaging.

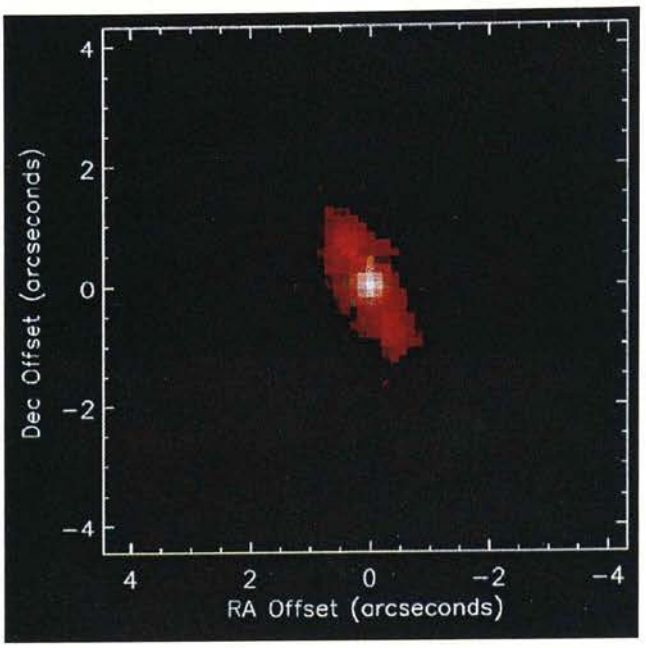


**Figure 1.4:** Mid-IR image of HR4796, taken with MIRLIN on the Keck telescope. This image is a colour composite of images taken at 12 and 20 $\mu$m. From Koerner et al. (1998).

Mid-IR imaging has been undertaken for HD141569 (Fisher et al. 2000; Marsh et al. 2002), HR4796 (Koerner et al. 1998; Jayawardhana et al. 1998; Telesco et al. 2000) and $\beta$ Pic (Lagage and Pantin 1994; Pantin et al. 1997; Wahhaj et al. 2003). The image of HR4796 is shown in Figure 1.4. These observations allow direct measurement of many of the most important properties of the objects. The outer disk can be resolved, which allows the location of the dust to be measured. Also, by measuring the excess at two wavelengths (e.g. 10 and 20 $\mu$m), the temperature of dust grains can be obtained. Since the temperature of a dust grain at a given distance from a star depends on its size, this provides information about the size distribution of the dust grains. Analysis of radiation and collisional processes in the disk can then determine whether the disk is undergoing a collisional cascade. This approach has successfully been employed for all three of the objects that have been imaged so far.

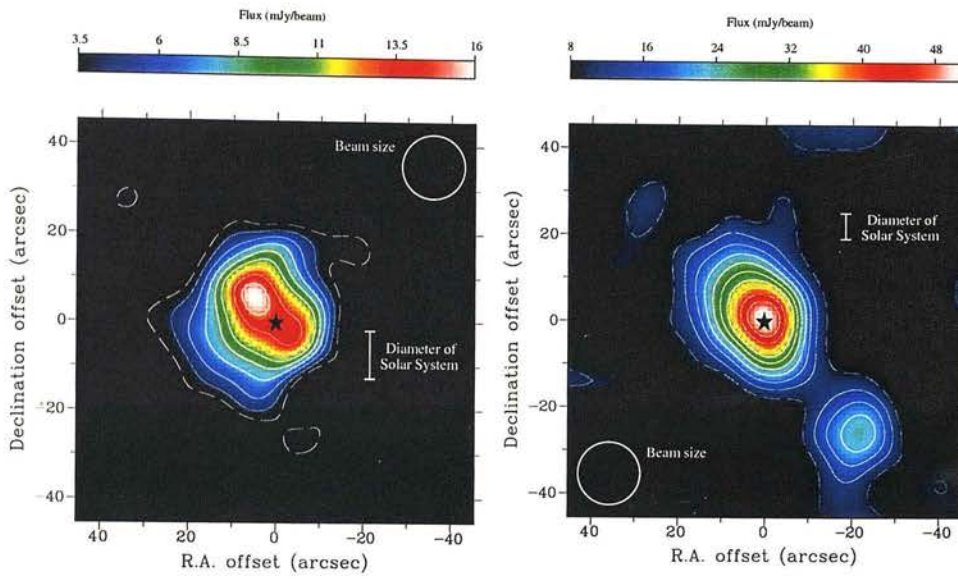


**Figure 1.5:** SCUBA images of Vega (left) and $\beta$ Pic (right) at 850 $\mu$m. From Holland et al. (1998b).

### 1.5.3 Sub-millimetre single dish photometry and imaging

The first sub-mm observations of Vega disks were purely photometric, and these observation produced information about the SED of the disks (Sylvester et al. 1996, 2001). However, instrumental advances have made sensitive sub-mm imaging possible, and observations of Vega disks have been one of the key results of this observational technique. Sub-mm imaging of Vega-type disks has been dominated by one instrument: SCUBA on the 15 meter James Clerk Maxwell Telescope in Hawaii. SCUBA images at 450 and 850 $\mu$m simultaneously, with a resolution of 7 and 14 arcsec respectively. As with mid-IR imaging, the photospheric emission is low at these wavelengths, whereas the Vega disks emit strongly due to their large effective surface area. Sub-mm images of the 'Big four' Vega-type disks (Vega, $\beta$ Pic, $\epsilon$ Eri and Fomalhaut) were produced shortly after SCUBA's commissioning (Holland et al. 1998b; Greaves et al. 1998) and deeper, more detailed images of Fomalhaut have subsequently been taken (Holland et al. 2003). This work has produced excellent constraints on the spatial distribution of the dust, and has shown that material can be contained within an extremely thin and well defined ring, particularly for the disks around $\epsilon$ Eri and Fomalhaut. SCUBA images of these disks are shown in Figures 1.5, 1.6 and 1.7.

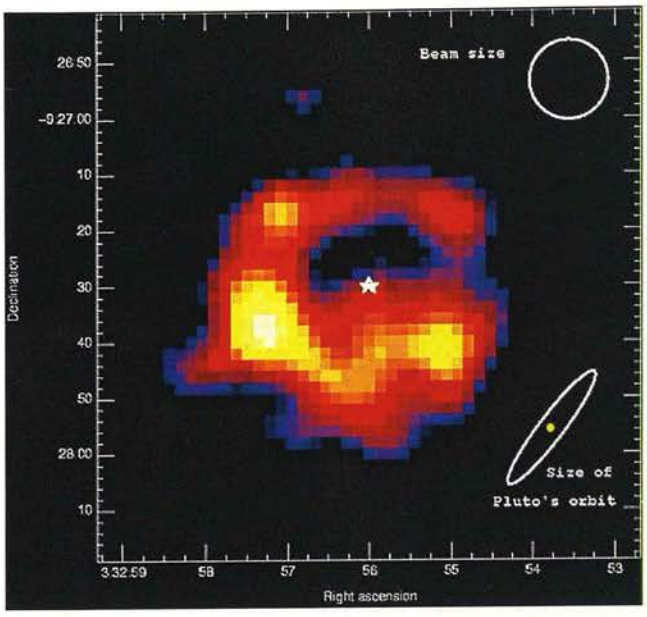


**Figure 1.6:** SCUBA image of $\epsilon$ Eri at 850 $\mu$m. From Greaves et al. (1998).

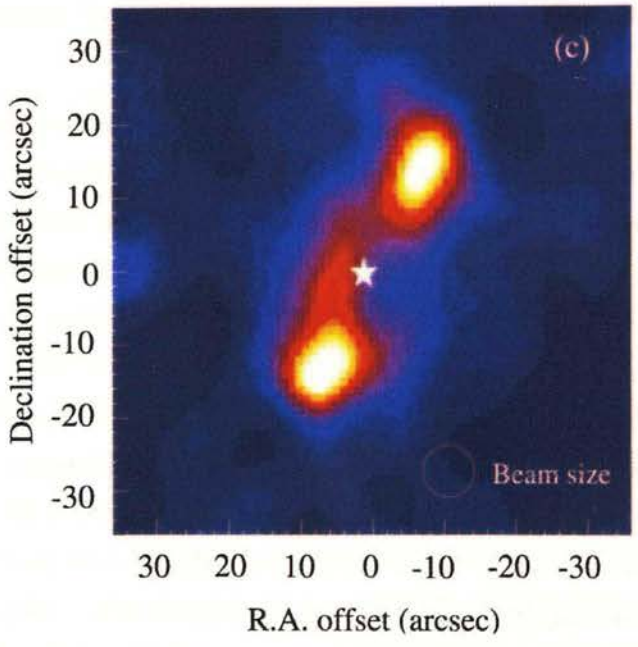


**Figure 1.7:** SCUBA image of Fomalhaut at 450 $\mu$m. This image has been deconvolved with the measured telescope point spread function using the Richardson-Lucy deconvolution technique. From Holland et al. (2003)

### 1.5.4 Millimetre and sub-millimetre interferometry

Millimetre and sub-mm interferometry offers the prospect of sub-arcsec imaging of disks, and will undoubtedly be one of the key tools for observing Vega-type disks in the future. Unfortunately, current instruments lack the sensitivity to image Vega-type disks without very long integration times. However, two separate images of Vega's disk have been made, one using the Owens Valley Radio Observatory (Koerner et al. 2001) and one using the IRAM Plateau de Bure interferometer (Wilner et al. 2002). Both images show that the Vega disk is very clumpy, and whilst the two images are not completely in agreement as to the flux and location of the clumps, they look similar enough confirm that they are real features. The significance of these clumps is discussed in Section 1.7.

## 1.6 Observations of gas in debris disks

The only Vega-type disk with a well studied gas component is $\beta$ Pic. The success in detecting gas in $\beta$ Pic's disk is partly due to the edge-on orientation of the disk, which makes searches for absorption lines much more sensitive. Optical and UV spectroscopy show absorption lines produced by several different atomic species (Kondo and Bruhweiler 1985; Hobbs et al. 1985; Vidal-Madjar et al. 1986; Lagrange et al. 1987, 1995, 1998). In addition, high resolution spectroscopy of resonantly scattered sodium emission lines has shown that this gas is in Keplarian rotation around the central star (Olofsson et al. 2001). These observations detect only tracer elements, and the bulk of the mass (in the form of neutral and molecular hydrogen) remains undetected. However, this gas must be present in order to stop ions like Ca II or Fe II being blown out of the disk by radiation pressure (Lagrange et al. 1998; Olofsson et al. 2001; Brandeker et al. 2004). The actual mass of $H_2$ in the disk of $\beta$ Pic is presently controversial, with some observations suggesting a gas mass significantly higher than the dust mass, on the basis of mid-IR emission lines (Thi et al. 2001a,b) and others suggesting much less, on the basis of UV absorption lines (Lecavelier des Etangs et al. 2001).

For young stars, CO observations are often used to determine the gas content of a disk (e.g. Brittain et al. 2003), and such observations have also been made for Vega-type disks (Yamashita et al. 1993; Savoldini and Galletta 1994; Zuckerman et al. 1995; Dent et al. 1995; Liseau and Artymowicz 1998; Liseau 1999). However, the observations of main sequence stars tend to find little or no CO. Zuckerman et al. (1995) conducted a survey of CO emission from A type stars with ages between $10^6$

and $10^7$ years, and found that the CO is removed on a timescale of about $10^6$ years. This does not necessarily mean that the gas is entirely removed this quickly though; Kamp and Bertoldi (2000) find that in low mass disks around main sequence stars, CO is very likely to be photodissociated or frozen out onto the dust grains, and so CO is a poor tracer of the total gas content in these disk.

## 1.7 Morphology of Vega-type disks

The resolved images of Vega-type disks have revealed detailed dust maps for the closest objects, and two key features have become apparent. Firstly, Vega disks often have a void close to the star, with all the dust held in a ring further out. The SCUBA images of Fomalhaut and $\epsilon$ Eri and the mid-IR image of HR4796 show this effect most clearly. Secondly, the disks tend not to look axisymmetric, with large clumps or asymmetries in the dust distribution. The asymmetries have attracted particular interest because they may be due to the gravitational influence of a planet embedded within the disk. In fact, planets could affect disks in several different ways, including disk warps (Mouillet et al. 1997b), clearing of gaps in a disk (Lagage and Pantin 1994; Wolf et al. 2002), or trapping of dust in resonances (Roques et al. 1994; Lazzaro et al. 1994; Wyatt et al. 1999; Ozernoy et al. 2000; Quillen and Thorndike 2002; Kuchner and Holman 2003; Wyatt 2003). The resonance method is particularly promising, as the location of clumps within a disk can be used to determine the mass, location, and orbital parameters of the perturbing planet. However, clumps within the disk are not the only possible explanation for the observed images. In particular, at 850 $\mu$m there is a significant number of background galaxies at similar brightness to the detected clumps (Scott et al. 2002), and these could explain some of the observed asymmetries in the SCUBA images. However, for some objects the clumps must be real: the clumps in the interferometric images of Vega are very unlikely to be due to background galaxies, because the galaxy counts at 1.3 mm are much lower than at 850 um. The flux of the brightest clump is $4.0 \pm 0.9$ mJy according to Koerner et al. (2001), and the probability of a background galaxy this bright falling within 15 arcsec of Vega (the size of the map in this case) is only 0.8%, using source counts at 1.25 mm made using the MAMBO bolometer array (Thomas Greve, personal communication). Wilner et al. (2002) claim the flux of the brightest clump is actually $7.1 \pm 1.4$ mJy, which would result in an even lower probability of background contamination. The independent detection of clumps significantly brighter than the background population by two separate instruments is

very good evidence that the clumps in Vega's disk are real.

## 1.8 Overview of thesis

This thesis describes three different observational programmes that have been undertaken to probe debris disks around nearby stars, and the detailed modelling and analysis that has been used to interpret these observations. The theoretical background which underpins our understanding of debris disks is described in Chapter 2, including the physical processes that shape the disks, and the thermal emission that a disk will produce. Chapter 3 contains sub-mm observations of debris disks, and detailed modelling of these observations using a realistic model of the dust grains in the disks. Chapter 4 describes mid-IR observations and analysis to determine the disk parameters (in particular disk size) for two dust disks. These observational projects focus on the dust content of debris disks, but gas can also play an important role, and so Chapter 5 describes a search for molecular hydrogen in two pre-main sequence disks. Finally, Chapter 6 summarises the thesis, and outlines the key areas that must be addressed in future work.

# Chapter 2

# Theory of dusty circumstellar disks

## 2.1 Introduction

This chapter covers the theoretical background which underpins our understanding of Vega excess disks. The background comes from several different fields, but the aim here is to give a coherent picture of the processes that affect the long-lived, dust dominated disks found around main sequence stars. Ultimately, observation must be reconciled with theory, and this means firstly understanding the physics that shape the disks, and secondly understanding how the observable properties of a disk depend on its structure.

### 2.1.1 Overview of a dusty disk

Dust disks are composed of dust grains. These dust grains are heated by radiation from the central star, and so they emit thermal radiation in the mid and far IR; also, some of the light from the central star is scattered by the grains, making the disk detectable in the visible and near-IR. So long as the disk is optically thin, the radiation emitted and scattered by the whole dust disk is simply the sum of the radiation emitted and scattered by each of the dust grains. The dust grains have a range of sizes, from sub-micron grains up to a millimetre and larger. In fact the size range can extend far beyond this, up to asteroids or comet type bodies hundreds of kilometres across. Though clearly it's difficult to think of such large objects as being dust grains, there

is no difference between a large dust grain and a small asteroid or comet, and the size distribution is a continuous function over the entire range of sizes.

Dust disks are dynamic objects. Dust grains are continuously being produced and destroyed in catastrophic collisions, and grains typically have a short lifetime compared to the lifetime of the disk. Several different forces affect the dynamics of the dust grains. As well as the gravitational attraction of the central star, forces due to radiation are also important. For some dust grains, the radiation forces can be greater than the gravitational attraction of the central star, so these grains are blown out of the disk as soon as they are created. Other grains can remain bound to the system, but will have orbits which evolve either inwards or outwards with time.

The observed properties of the dust disk depend on several factors. The optical properties of a single dust grain depends on its size and its composition, so the emission of a dust disk will depend on the size distribution of the dust grains, and on the details of the grains' construction. The optical properties of the grains also affects their dynamics, because radiation forces depend on how efficiently a grain absorbs and scatters light. The optical properties also determine the temperature of the grains, and the thermal emission spectrum produced by the grains.

The outline of this chapter is as follows. First, the forces which affect dust grains are described, followed by a discussion of the collisional destruction and creation of bodies in the disk. Then, the optical properties of dust grains are discussed in the context of a model of the grains in protoplanetary disks, and finally the procedure for calculating the expected thermal emission from a dust disk is described. The material covered in this chapter is discussed in more depth elsewhere: a good reference for radiation forces is Burns et al. (1979), for gas drag forces see Beckwith et al. (2000) and Supulver and Lin (2000), calculation of dust grain optical properties is described in Laor and Draine (1993), and collisional cascade theory is discussed by Tanaka et al. (1996), Durda and Dermott (1997) and Krivov et al. (2000).

## 2.2 Dynamics in a dust disk

### 2.2.1 Orbits due to gravity and radiation pressure

For any particle orbiting a star, the dominant force is gravitational. This force $F_{\rm grav}$ is given by

$$F_{\rm grav} = \frac{GM_* m}{r^2}, \tag{2.1}$$

where $G$ is the gravitational constant, $M_*$ is the mass of the star, $m$ is the mass of the particle and $r$ is the distance from the particle to the star. For very large particles (e.g. planets), this is the only significant force, but for smaller bodies other forces become important. For small ($\sim$ 1 $\mu$m) dust grains, the gravitational force from the star is countered by radiation pressure: starlight absorbed or scattered by the dust grain carries momentum, and so the radiation exerts a force away from the central star. The strength of this force depends primarily on the radiation flux and the surface area of the dust grain, but is also influenced by the optical properties of the particle. The force due to radiation pressure is:

$$F_{\rm rad} = \frac{L_* A}{4\pi c r^2} \langle Q_{\rm pr} \rangle_{F_*}, \tag{2.2}$$

where $L_*$ is the stellar luminosity, $A$ is the cross-sectional area of the particle, $c$ is the speed of light, $r$ is the distance from the star and $\langle Q_{\rm pr} \rangle_{F_*}$ is the radiation pressure coefficient, which accounts for the efficiency with which the particle absorbs and scatters light from the central star, and is equal to 1 for a perfectly absorbing material. As radiation pressure follows an inverse-square law, the ratio of the radiation force to the gravitational force does not depend on the distance to the star. This ratio is conventionally denoted by $\beta$:

$$\beta = F_{\rm rad}/F_{\rm grav}. \tag{2.3}$$

For a spherical particle of density $\rho$ and diameter $D$, $\beta$ is given by:

$$\beta = C_r \frac{1.5}{\rho D} \frac{L_*}{L_\odot} \frac{M_\odot}{m_*} \langle Q_{\rm pr} \rangle_{F_*}, \tag{2.4}$$

where $C_r$ is a constant with value $7.65 \times 10^{-4}$ kg m$^{-2}$ (de Pater and Lissauer 2001). The orbit of a particle under the influence of radiation pressure remains a conic section, and the overall effect is to reduce the apparent mass of the central star by a factor of $1 - \beta$.

Radiation pressure is most significant for particles which have a diameter close to the characteristic wavelength of the stellar spectrum. Larger particles have too much mass to be significantly affected by radiation pressure, and smaller particles are less affected because they have a low radiation pressure coefficient, as it is difficult for a dust grain to absorb or emit radiation with a wavelength bigger than its diameter.

### 2.2.2 Blowout diameter

If a small ($<$ 1 $\mu$m) dust grain is produced in a destructive collision, it will be much more susceptible to radiation pressure than its parent body. It will therefore follow a

new orbit, even though its initial position and velocity are very similar to the original body. If the original body is on a circular orbit with semi major axis $a$ and has a $\beta$ of 0, then new grain will have a semi-major axis and eccentricity given by

$$a' = a\frac{1-\beta'}{1-2\beta'} \tag{2.5}$$

$$e' = \frac{\beta'}{1-\beta'}. \tag{2.6}$$

If the new grain has a $\beta' > 0.5$, then $a'$ becomes infinite, hence the grain will no longer be bound to the system and will leave on the orbital timescale. Because these grains leave the system so quickly, we expect to see few in observed systems, except for some grains that have just been created and have not yet escaped.

### 2.2.3 Poynting-Robertson drag

In addition to the radial force described in the previous section, stellar radiation also causes a force in the opposite direction to the particle's velocity, known as Poynting-Robertson (PR) drag. The force occurs because the thermal emission from a dust grain, whilst being isotropic in the grain's rest frame, is anisotropic in the rest frame of the star. Photons emitted in the forward direction are blue-shifted, and therefore have more momentum than the red-shifted photons emitted in the backward direction. This momentum loss is not accompanied by a loss in mass (as would be the case for an isolated radiating dust grain), so the loss of momentum leads to a loss of velocity, i.e. it produces a force opposing the dust grains motion. This force causes the eccentricity and semimajor axes of the grain's orbit to decrease with time, ultimately causing micron to centimetre sized dust grains to spiral into the central star. For a circular orbit, the timescale for removal by PR drag is

$$\tau_{\rm pr} \approx 400\frac{M_\odot}{M_*}\frac{r^2}{\beta}, \tag{2.7}$$

where $r$ is the initial distance from the star in AU (de Pater and Lissauer 2001).

### 2.2.4 Gas drag

For disks with a significant gas content, the effects of aerodynamic drag can be extremely important (Beckwith et al. 2000). Gas drag will damp the eccentricity and orbital inclination of a particle, and can also cause migration of dust and larger bodies inwards or outwards through a disk. The drag force depends on several factors, including the size, density and speed of the dust grain and the density and temperature

of the gas, and different drag laws apply in different physical situations. However, for dust grains in a circumstellar disk the Epstein gas drag lag usually applies. A more detailed discussion of the following material is contained in Supulver and Lin (2000), who also discuss the Stokes drag law which applies for larger particles.

Epstein drag occurs when the particle size is much smaller than the gas mean free path $l$, and particle's velocity with respect to the gas is subsonic. For a neutral gas of spherical particles, the mean free path is

$$l = (N\pi a_0^2)^{-1}, \tag{2.8}$$

where $N$ is the number density of particles and $a_0$ is their diameter ($\sim 1.5 \times 10^{-8}$ cm for $H_2$ molecules). The typical density in the midplane of a young circumstellar disk is around $10^{-11}$ g cm$^{-3}$ (Hayashi et al. 1985), which gives a mean free path of $l \sim 5$ m. The drag force $F_D$ due to Epstein drag is

$$F_D = \frac{\pi}{3} D^2 \rho_{\rm gas}\, v_{\rm therm}\, v_{\rm rel}, \tag{2.9}$$

where $D$ is the diameter of the dust grain, $\rho_{\rm gas}$ is the density of the gas, $v_{\rm therm}$ is the thermal velocity of the gas molecules and $v_{\rm rel}$ is the relative velocity of the particle to the gas. The stopping timescale $t_s$ (i.e. the time for the velocity to fall by a factor of e) is then given by

$$t_s = \frac{m\, v_{\rm rel}}{F_D} \tag{2.10}$$

$$= \frac{4D\rho_{\rm dust}}{\rho_{\rm gas}\, v_{\rm therm}}. \tag{2.11}$$

For solid silicate grains ($\rho_{\rm dust} = 3$ grams cm$^{-3}$) in a 100 K nebula of density $10^{-11}$ g cm$^{-3}$, anything smaller than a few centimetres will have a stopping time of less than one orbital period, and will therefore be strongly coupled to the gas. If the grains are fluffy, then grains up to about a meter will be coupled to the gas (Nakamura and Hidaka 1998).

As well as damping the random velocities of the dust grains, gas drag can also cause migration of dust grains through the disk. This is because a gas disk is supported not only by rotation, but also by gas pressure, and so the gas will rotate slightly slower than the Keplerian velocity. For large dust grains with negligible $\beta$, this will cause a drag force which will pull the grains inwards. However, grains which are significantly affected by radiation pressure will have a typical circular velocity which is lower than the gas, so will be accelerated by the gas and pushed out to the edge of the gas disk (Takeuchi and Artymowicz 2001; Takeuchi and Lin 2002, 2003).

### 2.2.5 Other forces

As well as radiation pressure, PR drag, and gas drag, other more subtle radiation forces can affect orbiting bodies. The Yarkovski effect (Burns et al. 1979) arises because of the rotation of an asteroid; the evening hemisphere of a body will be warmer than the morning hemisphere, so will emit more radiation, resulting in a net force. The direction of the force depends on the rotation of the body, with prograde rotation causing a force away from the star, and retrograde rotation creating a force towards the star. The Yarkovski effect is most significant for meter to kilometre sized bodies. There is also a seasonal Yarkovski effect due to the difference in the temperature between the summer and winter hemispheres. Corpuscular drag by stellar wind particles also has an effect on dust grains, as it produces an effect similar to PR drag. For the smallest dust grains ($\sim 0.01$ $\mu$m) this effect creates the dominant non-radial force, as such small grains have low $\beta$ and so are only weakly affected by radiation pressure and PR drag.

## 2.3 Grain size distribution and the collisional cascade

As discussed in Section 1.2.2, the small dust grains observed around main sequence stars must be continuously replenished, and the best explanation for this dust production is that Vega excess disks are in a collisional cascade. In a collisional cascade, most bodies in a disk are the product of the previous collisional destruction of a larger body. These larger bodies will themselves have been produced by a destructive collision, and small bodies will be broken up into still smaller pieces. This cascade will cover a huge range of sizes, from micron sized dust grains up to large (100 km) asteroids. The size distribution that arises from such a cascade is known theoretically to be

$$dn(D) \propto D^{2-3q}\, dD, \tag{2.12}$$

where $q = 11/6$ (Dohnanyi 1969), assuming that the strength of the bodies does not depend on their size. In this size distribution, most of the surface area of the disk is contained within the smallest grains, whereas most of the mass is contained in the largest bodies.

For a medium sized dust grain, most collisions are with very small dust grains, as these have the largest cross sectional area and hence the highest collision probability. However, these grains also have very low mass and so do not generally have enough energy to destroy the larger body. This means that the majority of collisions in the disk are non catastrophic, resulting either in an elastic collision or in a cratering, i.e.

the larger object loses some material but is not broken up. A collision with a grain large enough to cause complete destruction is much rarer, and a collision with a grain significantly larger than this critical value is rarer still. Dust grains therefore tend to be destroyed by a grain which is only just big enough to do so. Such a collision will break up the original grain, but will only give a small velocity kick to the resulting fragments. The result is a set of new particles with very similar initial position and velocity to the original body.

The theoretical size distribution described by Equation 2.12 is only expected to be true for certain sized bodies in the collisional cascade. For very small dust grains, radiation pressure will quickly remove the particle from the disk, causing a severe depletion of these grains relative to their expected frequency. Also, the largest bodies will be strengthened by the effects of gravity, which means that it is more difficult to destroy them in a collision (i.e. destruction requires a projectile with higher energy). A rigorous calculation of the size distribution can therefore only be done by numerical simulation (Durda et al. 1998; Krivov et al. 2000; Thébault et al. 2003). As well as the additional complexity and computational difficulty of the numerical approach, a lot of extra free parameters are introduced into the model including the distribution of orbital elements of bodies in the disk, and the density and strength of these bodies.

### 2.3.1 Collisionally dominated vs. PR dominated disks

Debris disks fall into two categories, depending on how much solid material they contain (Wyatt 1999). The two types of disks behave in quite different ways, and show very marked observational differences. The key difference between the two types of disk is the way in which small dust grains are removed.

A dust grain in a stable orbit around a star can be removed in two different ways: it can either be broken up in a destructive collision, or it can be pulled into the central star by PR drag. The relative importance of these two processes depends on how dense the disk is. Dense disks tend to be collisionally dominated, and dust grains will undergo destructive collisions on a timescale shorter than the PR timescale. This means that even small dust grains will not have time to be affected by PR drag before they are destroyed. Grains are broken up into smaller and smaller pieces, until eventually the fragments get smaller than the blowout diameter and are pushed out of the disk by radiation pressure (Section 2.2.2). Conversely, tenuous disks have fewer collisions and so will be PR dominated; small grains will be dragged inwards by PR drag, eventually falling into the central star. Detectable Vega excess disks tend to contain enough

material to be collisionally dominated, while the asteroid belt is an example of a PR dominated dust disk.

The collisional timescale for grains in a disk depends on the surface density of the disk and the orbital period. For a disk with a face-on optical depth $\tau(r)$, the collisional timescale is given by (Backman and Paresce 1993)

$$t_{\rm col} = \frac{t_{\rm orbital}}{8\,\tau}. \tag{2.13}$$

For a resolved disk, this timescale can be determined fairly easily, as the face-on optical depth can be determined from the observed temperature and flux. However, the collisional timescale in itself does not determine whether a disk is collisionally dominated or not. The important quantity is really the *destructive* collision timescale, and this is much more difficult to obtain. To calculate this requires knowledge of the grain size distribution, the mean collisional velocity, and of the strength of the dust grains: quantities which are not generally observable for extrasolar debris disks. A rigorous analysis of the destructive timescale must make assumptions about these quantities. For example the analysis of the destructive collision timescale in Fomalhaut's disk by Wyatt and Dent (2002) used a size distribution from collisional cascade theory and SED modelling, grain strengths from lab experiments and computer modelling, and assumed the collisional velocity is $\sim 10\%$ of the Keplerian velocity, as is the case in the asteroid belt, and as inferred from the opening angle of $\beta$ Pic's disk. Because of the uncertainties in this type of approach, such analysis does not by itself prove that Vega excess disks are collisionally dominated. However, the resolved sub-mm images of Fomalhaut and $\epsilon$ Eri, and the spectral energy distributions of known Vega excess disks in the near and mid-IR both indicate that the inner disks of Vega excess stars are mainly free of dust. If the disks were PR dominated, then this region would contain many small dust grains that were being pulled in by PR drag, showing that the disks must be collisionally dominated, and hence that the collisional velocities must be high enough that they result in destructive collisions. The other possible explanation for the clear central region is that a planet has removed the dust from this part of the disk.

## 2.4 Dust grain optical models

Modelling an extrasolar debris disk requires detailed knowledge of the optical properties of the constituent dust grains. However, for obvious reasons these properties cannot be measured directly. Some understanding of extrasolar dust grains can be gained from

analysis of solar-system material, but this must be augmented by a theoretical model of how protoplanetary grains form.

The most widely used model is based on the idea that protoplanetary dust grains are porous aggregates of interstellar grains, with additional volatile material (i.e. ices) frozen in as they form (Greenberg and Hage 1990; Kruegel and Siebenmorgen 1994). In this model, the interstellar grains are considered to be elongated grains with a silicate core and an organic refractory mantle, about 0.1 $\mu$m in size, and the volatile component is often considered to be dominated by water ice. With this model in place, the next step is to calculate the optical properties for the resulting dust grains. This task is split into two parts: firstly, the optical properties of the composite material are determined, and then the properties of the final grains are calculated.

### 2.4.1 Calculating the optical properties of a dust grain

The interaction of a material with light can be described by its complex refractive index:

$$m(\lambda) = m'(\lambda) + im''(\lambda). \tag{2.14}$$

For a composite material, the complex refractive index can be calculated from the refractive indices of the constituent materials, using for example Maxwell-Garnett effective medium theory (Bohren and Huffman 1983). Obtaining the optical constants of the constituent materials (i.e. interstellar grains and ices) is itself problematic, but some data are available from fits to the observed interstellar extinction curve, and from lab spectra of meteorites and common ices.

Once the optical properties of the composite material have been determined, the properties of the dust grains can be calculated. The optical properties of a spherical dust grain can be parameterised by its absorption efficiency $Q_{\rm abs}(\lambda)$, its scattering efficiency $Q_{\rm sca}(\lambda)$ and the angular dependence of the scattering efficiency $f(\theta, \lambda)$. A dust grain with $Q_{\rm abs} = 1$ would absorb all the light which intersected with its geometric cross section; similarly, a grain with $Q_{\rm sca} = 1$ would reflect all the light which intersected with its geometric cross section. Calculation of optical efficiencies given the complex refractive index is generally difficult, and analytic solutions exist only for spherical particles, infinite cylinders, and spheroids. The simplest approach is to assume that the dust grains are spherical, in which case $Q_{\rm abs}$, $Q_{\rm sca}$ and $f(\theta)$ can be calculated using Mie theory (Bohren and Huffman 1983). For dust grains which are much larger than the wavelength of the light, Rayleigh-Gans theory and geometric optics must be used

in place of Mie theory (Laor and Draine 1993).

The entire process is shown in Figures 2.1 to 2.3. The complex refractive indices of the constituent materials are shown in Figure 2.1, the complex refractive index of the composite material is then calculated using Maxwell-Garnet effective medium theory (Figure 2.2), and the absorption efficiencies of the final grains are calculated using Mie theory and shown in Figure 2.3. These figures were generated using programs written by Mark Wyatt for the modelling of Fomalhaut's dust disk (Wyatt and Dent 2002).

The final parameter to be calculated is the radiation pressure coefficient, $Q_{\rm pr}$. This depends on what fraction the incident radiation the dust grain absorbs, what fraction it scatters, and what direction the scattering occurs in:

$$Q_{\rm pr} = Q_{\rm abs} + Q_{\rm sca}(1 - \langle \cos\theta \rangle), \tag{2.15}$$

where $\langle \cos\theta \rangle$ accounts for the relative importance of forward and back scattering. For a normalised scattering phase function $f(\theta)$ (where $\theta = 0$ means forward scattering and $\theta = \pi$ radians means back scattering), this is given by integrating over all directions:

$$\langle \cos\theta \rangle = \int_{4\pi} f(\theta) \cos\theta \, d\chi, \tag{2.16}$$

where $d\chi$ is an element of solid angle. As $Q_{\rm pr}$ is wavelength dependent, the effective value will depend on the stellar spectrum $F_*(\lambda)$, and is given by

$$\langle Q_{\rm pr} \rangle_{F_*} = \frac{\int Q_{\rm pr}(\lambda) F_*(\lambda) \, d\lambda}{\int F_*(\lambda) \, d\lambda}. \tag{2.17}$$

## 2.5 Thermal emission from a dust disk

### 2.5.1 Temperature of a dust grain

The temperature of a dust grain is set by the balance between energy it absorbs from the central star, and the energy it radiates away thermally. For a rapidly rotating perfect blackbody, the resulting temperature is

$$T_{\rm bb} = \left( \frac{L_*}{16\pi r^2 \sigma_{\rm sb}} \right)^{1/4}, \tag{2.18}$$

where $r$ is the distance from the star and $\sigma_{\rm sb}$ is the Stefan-Boltzmann Constant. However, small dust grains absorb energy from the star much more efficiently than they emit it. This is because the wavelength the grain is trying to emit at is typically in the mid or far IR, i.e. much bigger than the size of the grain, and so emission is more

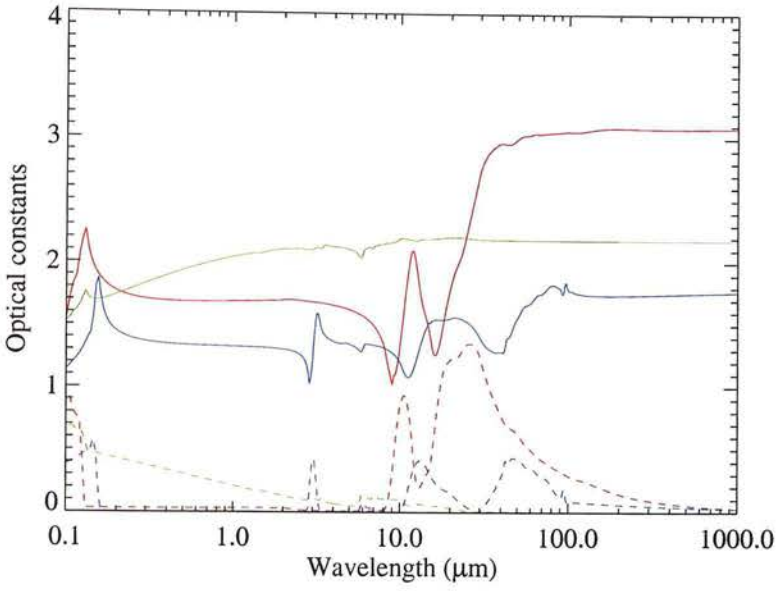


**Figure 2.1:** Optical constants for silicates (red), organic refractory material (green), and water ice (blue). The data for silicates and organic refractory material are from Li and Greenberg (1997), and the data for ice are from Li and Greenberg (1998). Solid lines show the real part of the complex refractive index, dashed lines show the imaginary part.

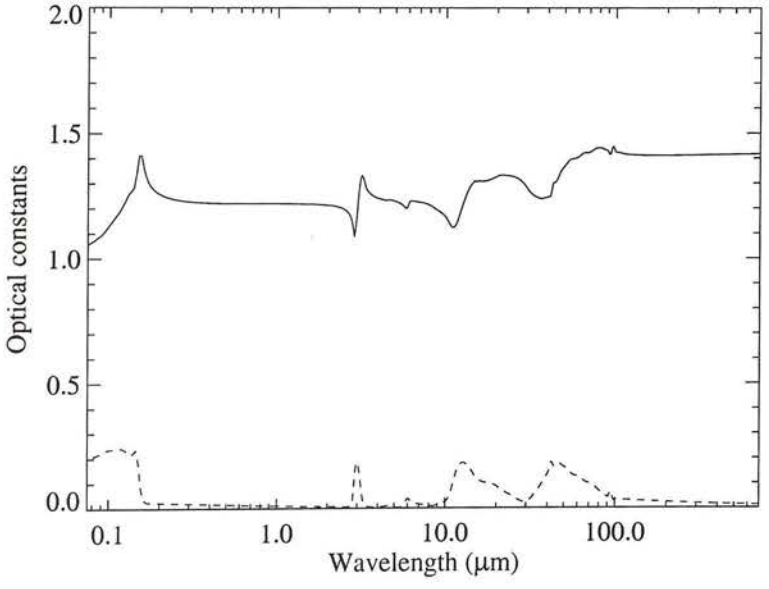


**Figure 2.2:** Optical constants for a composite dust grain material. In this plot, the silicates/organic ratio is 1/3 and the porosity is 0.9, 50% of which is filled with water ice. Solid lines show the real part of the complex refractive index, dashed lines show the imaginary part.

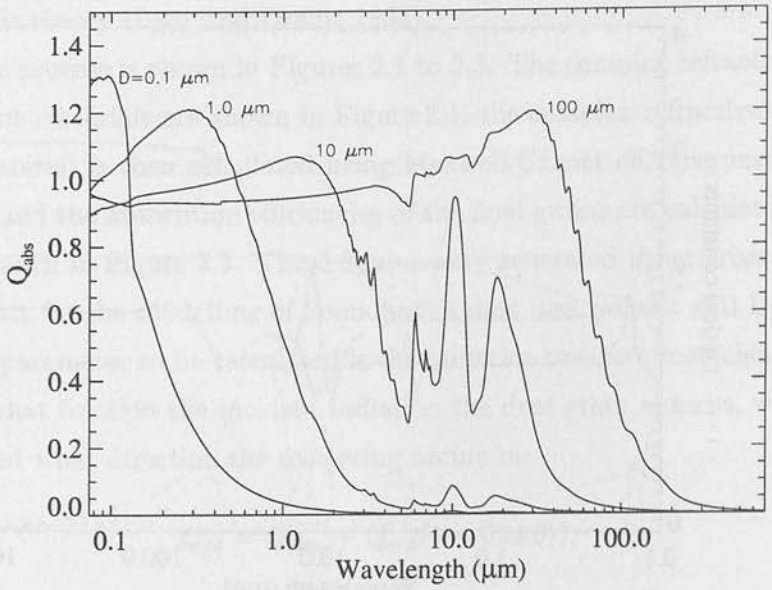


**Figure 2.3:** $Q_{\rm abs}$ for the composite material shown in Figure 2.2 for spherical grains of various sizes.

difficult than absorption. This means that small dust grains are significantly hotter than blackbody grains. The temperature of the grain is then given by:

$$T(D,r) = \left( \frac{\langle Q_{\rm abs} \rangle_{F_*}}{\langle Q_{\rm abs} \rangle_{T(D,r)}} \right)^{1/4} T_{bb}, \tag{2.19}$$

where $\langle Q_{\rm abs} \rangle_{F_*}$ is the absorption efficiency averaged over the stellar spectrum, and $\langle Q_{\rm abs} \rangle_{T(D,r)}$ is the absorption efficiency averaged over the blackbody spectrum of the grain's temperature. As $T(D,r)$ appears on both sides of the equation, this must be solved iteratively. Equilibrium temperatures for solid and porous grains are shown in Figure 2.4.

### 2.5.2 Observable emission

With all the above details in hand, it is now possible to work out the thermal emission from a disk. The observed flux of a single dust grain with diameter $D$ and at a distance $r$ from the central star is:

$$F_\nu(\lambda, D, r) = Q_{\rm abs}(\lambda, D)\, B_\nu[\lambda, T(D,r)]\, \Omega(D), \tag{2.20}$$

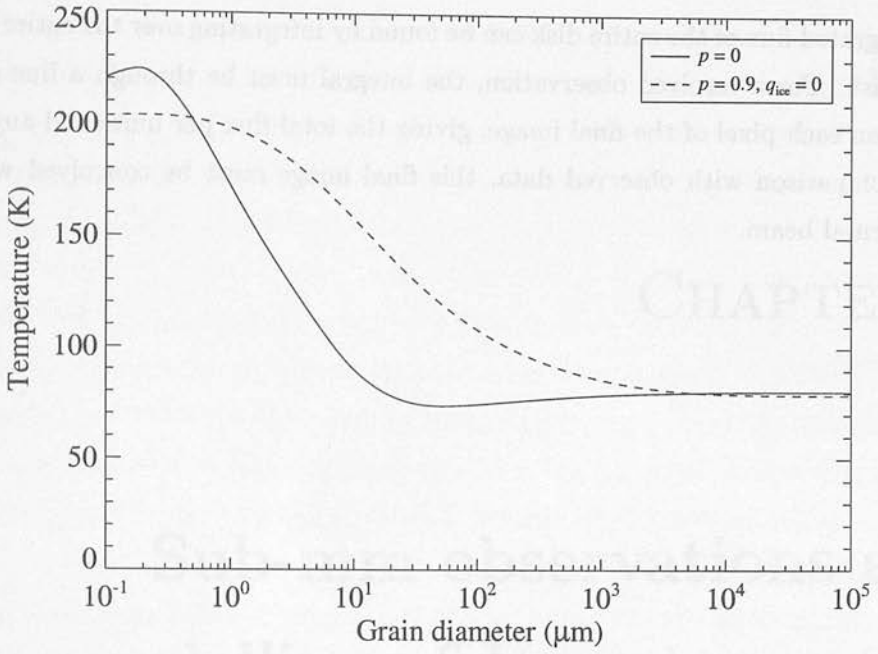


**Figure 2.4:** Temperature of solid and porous grains 50 AU from an A0 type star as a function of grain size.

where $B_\nu$ is the Planck function, and $\Omega$ is the solid angle subtended by the dust grain. If the observer is at a distance $R$ from the grain, this is given by

$$\Omega = \sigma(D)/R^2, \tag{2.21}$$

where $\sigma(D)$ is the cross sectional area of the grain ($= \pi D^2/4$ for a spherical grain). An element of volume $dV$ located at $\mathbf{r}$ within the disk will contain dust grains of different sizes. The number of grains within this volume element $dV$ and with size between $D$ and $D + dD$ will be on average $n(D, \mathbf{r})\, dD\, dV$. The cross sectional area of the grains is $\sigma(D, \mathbf{r})\, dD\, dV$, where

$$\sigma(D, \mathbf{r}) = n(D, \mathbf{r})\, \sigma(D). \tag{2.22}$$

The thermal emission from this volume element from grains with diameter between $D$ and $D + dD$ can then be calculated:

$$dF_\nu(\lambda, D, \mathbf{r}) = Q_{\rm abs}(\lambda, D)\, B_\nu[\lambda, T(D, r)]\, (\sigma(D, \mathbf{r})/R^2)\, dD\, dV, \tag{2.23}$$

giving a total flux with $dV$ of

$$dF_\nu(\lambda, \mathbf{r}) = \int_{D_{\rm min}}^{D_{\rm max}} Q_{\rm abs}(\lambda, D)\, B_\nu[\lambda, T(D, r)]\, (\sigma(D, \mathbf{r})/R^2)\, dD\, dV. \tag{2.24}$$

The integrated flux of the entire disk can be found by integrating over the entire volume of the disk. For a resolved observation, the integral must be through a line of sight centred on each pixel of the final image, giving the total flux per unit solid angle. For direct comparison with observed data, this final image must be convolved with the instrumental beam.

# Chapter 3

# Sub-mm observations and modelling of Vega-type stars

## 3.1 Introduction

In studying Vega excess disks, sub-mm observations are of particular importance. Debris disks emit strongly in the sub-mm due to their large effective surface area, and at sub-mm wavelengths photospheric emission is small, so the disk can be detected unambiguously. In addition, the spatial resolution of sub-mm observations is high enough that some disks can be resolved, giving a great deal of information about the size and structure of the disks. The resolved sub-mm images of the disks around $\beta$ Pic, Fomalhaut, Vega and $\epsilon$ Eri have provided a large fraction of the current understanding of debris disks (Holland et al. 1998b; Greaves et al. 1998; Holland et al. 2003). In addition, photometry of unresolved targets has been used to expand the number of targets with good SED information (Sylvester et al. 1996, 2001), allowing indirect probes of disk structure and composition.

However, despite these advances, one of the main problems with understanding Vega excess disks remains that only a few have been studied with any detail. Though the Vega phenomenon is common, the low resolution of current far-IR and sub-mm instruments means that few Vega excess stars are close enough to be resolved. For the resolved disks, detailed analysis using realistic models for the optical properties and size distribution of the dust can be performed. This type of analysis has been undertaken

for $\beta$ Pic (Li and Greenberg 1998), HR4796 (Augereau et al. 1999b) Fomalhaut (Wyatt and Dent 2002) and $\epsilon$ Eri Li et al. (2003). These models use the observed spatial distribution of dust, and fit the SED by varying the dust composition and size distribution. However, as these objects have been analysed on a case-by-case basis, different models and assumptions are used, which makes it somewhat difficult to make direct comparisons between them. In addition, there are so few resolved targets that it is impossible to look for statistical trends between disk size, age, stellar mass, etc. However, there are many unresolved targets with good SED information, and new instruments such as SIRTF and SOFIA will produce many more such objects. A method which could retrieve the physical parameters of a disk from just its SED would be invaluable. To accomplish this, the detailed properties of the dust grains in Vega excess disks must be fully understood.

I have tried to tackle these problems in two ways. Firstly, I have made sub-mm photometric observations of Vega excess stars, to help constrain their SEDs. Secondly, I have attempted to model all known Vega excess stars with sub-mm data, using a consistent model with realistic dust grains. This allows the models of resolved targets to be compared directly; the knowledge of dust grain size and composition gained from this can then be used to estimate the disk size for the unresolved targets.

## 3.2 Observations

Sub-mm observations were made using the SCUBA bolometer array on the James Clerk Maxwell Telescope. The observations were made as part of several different observing programmes, and hence data were obtained in different observing modes. In addition, unpublished archive observations of suspected Vega excess stars were reduced to enlarge the sample. The observations are summarised in Table 3.1, and the parameters for the stars are shown in Table 3.2.

SCUBA is a sub-mm camera and photometer operating on the JCMT telescope in Hawaii (Holland et al. 1998a). The instrument has two arrays of bolometric pixels, one operating at 850$\mu$m and one at 450$\mu$m. The pixels in each array are arranged in a hexagonal close packed formation, giving a field of view of 2.3 arcmin. Both arrays collect data simultaneously by using a dichroic beamsplitter. The bolometers are cooled to 100 mK so that sensitivity is limited by the photon noise from the sky.

SCUBA observation and data reduction is complicated compared to say optical imaging with a CCD. There are two main reasons for this. Firstly, the atmosphere

emits strongly in the sub-mm, and the strength of this emission changes on a time-scale of less than a second. The effects of sky emission must therefore be removed. Secondly, the spacing of the bolometers in the arrays is too large for the image to be fully sampled. This means that many different telescope pointings must be used to fill in the gaps, and then this data must somehow be combined to form a fully sampled map.

Both these problems are overcome by using a moving secondary mirror. The secondary mirror of the JCMT can be tilted, so that a different part of the sky falls onto the detector. SCUBA observations are made by 'chopping' the secondary mirror, so that the central bolometer alternates between seeing the target and seeing a point 30–120 arcsec away, at a rate of about 8 Hz. Assuming that the sky emission from the two points is the same, the difference between the two fluxes is equal to the flux from the target, with no contamination from the sky. Each bolometer is sampled 128 times a second, and a demodulator then extracts the difference in flux between the two points (given the chopping frequency). The raw data are not actually stored, only the demodulated value.

This procedure removes most of the sky signal from the data. However, it also introduces systematic errors, because the two points being compared (target and blank sky) reach the detector by different paths. This is overcome by periodically moving the whole telescope so that the source is seen along the optical path originally used by the sky. This brings a new point of the sky into the path originally used by the source. This procedure is called nodding, and is repeated every 16 seconds when using SCUBA. The telescope only physically moves every 32 seconds, as the nods are done using a 'a,b,b,a,a,b,b... b,b,a' sequence.

The moving secondary is also used to solve the undersampling problem. Moving the primary mirror to make a fully sampled map is not possible, as it would create a huge amount a wasted time slewing between all the different pointings. So as well as chopping, the secondary mirrors uses a 'jiggle pattern' to fill in the gaps between the bolometers. To make a fully sampled map at 450 $\mu$m, 64 jiggle positions must be used, though if only 850 $\mu$m is required 16 positions are enough. Each jiggle position is held for one second. The 64 point jiggle is split up into four sections, so the nod can still be made every 16 seconds. Nodding every 64 seconds is not possible as the source rotation (due to the rotation of the Earth) would distort the image.

Whilst mapping in this way is ideal for extended sources, for an observation of an unresolved object a lot of time is spent where no bolometer can see the source. To

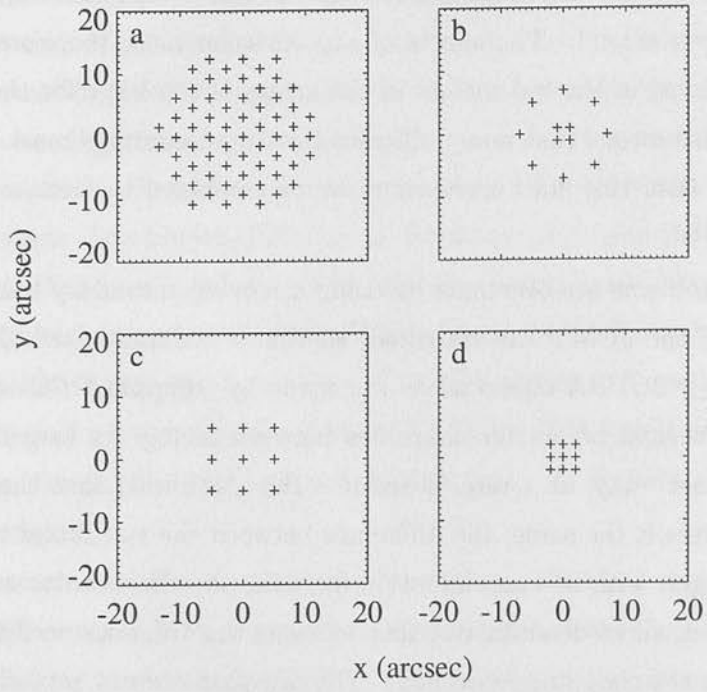


**Figure 3.1:** Comparison of the different jiggle patterns used on SCUBA: (a) full mapping mode, (b) 12 point extended mode, (c) 9 point extended mode, (d) normal photometry mode.

prevent wasting observation time in this way photometry mode can be used, which does not attempt to make a fully sampled map. In this mode, the central bolometer is always on source, and hence the observation will be more sensitive. The disadvantage is that a fully sampled map is not produced, so if the object is resolved the measured flux will underestimate the true flux. This mode should therefore only be used if the target is known to be point-like. Although a full jiggle map is not used in this mode, a small 9-point map is used to prevent small pointing errors from affecting the measurement.

For some of the observations in this project an extended photometry mode was used, which used a 9-point map with a spacing of 5 arcsec between each point, instead of the normal 2 arcsec spacing. The aim of this was to ensure that the true flux was measured even if the source was marginally resolved, whilst retaining most of the sensitivity advantage of photometry mode. Also, some data were taken using a 12-point pattern, with four points at the centre and eight points arranged around the central position, at a distance of 7 arcsec. Data from these extended photometry modes were reduced in exactly the same way as the conventional photometry. The different jiggle patterns are shown in Figure 3.1.

| Object | Date | Wavelength ($\mu$m) | Mode |
|---|---|---|---|
| HD17206 | 23 Aug 1997 | 450/850 | Map |
| | 27 Aug 1997 | 450/850 | Map |
| | 10 Mar 2001 | 450/850 | Ext. Phot. |
| HD23362 | 7 Jun 2000 | 450/850 | Map |
| HD34282 | 25 Sep 1997 | 450/850 | Map |
| | 29 Jan 2000 | 450/850 | Map |
| | 21 Mar 2000 | 450/850 | Map |
| HD34700 | 13 Dec 1997 | 450/850 | Map |
| | 14 Dec 1997 | 450/850 | Map |
| | 29 Jan 2000 | 450/850 | Phot |
| HD35187 | 13 Dec 1997 | 450/850 | Map |
| | 14 Jan 1998 | 450/850 | Map |
| HD38393 | 11 Mar 2001 | 450/850 | Ext. Phot. |
| | 12 Mar 2001 | 450/850 | Ext. Phot. |
| HD48682 | 9 Mar 2001 | 450/850 | Ext. Phot. |
| | 10 Mar 2001 | 450/850 | Ext. Phot. |
| | 11 Mar 2001 | 450/850 | Ext. Phot. |
| | 12 Mar 2001 | 450/850 | Ext. Phot. |
| HD69830 | 9 Mar 2001 | 450/850 | Ext. Phot. |
| HD81515 | 21 Mar 2000 | 450/850 | Map |
| HD109085 | 21 Mar 2000 | 450/850 | Map |
| | 10 Mar 2001 | 450/850 | Ext. Phot. |
| | 11 Mar 2001 | 450/850 | Ext. Phot. |
| | 12 Mar 2001 | 450/850 | Ext. Phot. |
| HD121617 | 11 Jun 2000 | 450/850 | Photometry |
| HD123160 | 9 Dec 1997 | 450/850 | Photometry |
| | 19 Feb 1998 | 450/850 | Photometry |
| | 10 Jun 2000 | 450/850 | Map |
| HD128167 | 21 Jan 2002 | 450/850 | Ext. Phot. |
| HD139664 | 30 Nov 1997 | 450/850 | Map |
| | 13 May 1998 | 450/850 | Map |
| | 25 Jun 1998 | 450/850 | Map |
| | 11 Jun 2000 | 450/850 | Photometry |
| HD141569 | 10 Jun 2000 | 450/850 | Photometry |
| | 11 Jun 2000 | 450/850 | Phot |
| HD207129 | 17 May 1998 | 450/850 | Map & Phot |
| | 28 May 1998 | 450/850 | Map |

**Table 3.1:** New observations used in the analysis. Observations before 2000 were extracted from the JCMT archive. The extended photometry of HD128167 was observed with a 12 point pattern, all other extended photometry is 9 point.

| Object | Other name | Sp. type | Distance pc | $L_{dust}/L_{star}$ | Ref. | Estimated age Myr | Ref. |
|---|---|---|---|---|---|---|---|
| HD17206 | | F5/F6V | 13.97 | | | | |
| HD23362 | | K2 | 308.6 | $7.9 \times 10^{-4}$ | 1 | | |
| HD34282 | | A0 | 163.9 | 0.39 | 1 | | |
| HD34700 | | G0 | > 180 | 0.14 | 2 | | |
| HD35187 | | A2 | 150 | 0.14 | 1 | | |
| HD38393 | | F7V | 8.97 | $5.3 \times 10^{-6}$ | Best fit model | $1660^{+1580}_{-1391}$ | 8 |
| HD48682 | | G0V | 16.4 | $1.2 \times 10^{-4}$ | Best fit model | | |
| HD69830 | | K0V | 12.58 | $2.3 \times 10^{-4}$ | Spline | 600-2000 | 10 |
| HD81515 | | A5Vm... | 107.0 | | | | |
| HD109085 | | F2V | 18.2 | $4 \times 10^{-4}$ | Spline | | |
| HD121617 | | A1V | 180[a] | $4.5 \times 10^{-3}$ | 2 | | |
| HD123160 | | K5 | > 250 | | | | |
| HD128167 | $\sigma$ Boo | F2V | 15.5 | $1.8 \times 10^{-5}$ | Best fit model | $1700^{+1320}_{-720}$ | 8 |
| HD139664 | | F5IV-V | 17.5 | $1.9 \times 10^{-4}$ | Spline | $1120^{+880}_{-875}$ | 8 |
| HD141569 | | B9 | 99.0 | $8.3 \times 10^{-3}$ | 2 | $5 \pm 3$ | 7 |
| HD207129 | | G0V | 15.6 | $1.0 \times 10^{-4}$ | Spline | $6030^{+2290}_{-1660}$ | 8 |
| HD22049 | $\epsilon$ Eri | K2V | 3.22 | $1.1 \times 10^{-4}$ | Best fit model | $730 \pm 200$ | 10 |
| HD39060 | $\beta$ Pic | A5V | 19.3 | $3 \times 10^{-3}$ | 3 | $20 \pm 10$ | 6 |
| HD109573 | HR4796 | A0V | 67 | 0.005 | 4 | $8 \pm 2$ | 9 |
| HD172167 | Vega | A0V | 7.76 | $2 \times 10^{-5}$ | 3 | $354^{+29}_{-87}$ | 5 |
| HD216956 | Fomalhaut | A3V | 7.69 | $8 \times 10^{-5}$ | 3 | $156^{+188}_{-106}$ | 5 |

Reference list: 1 Sylvester et al. (1996); 2 Sylvester et al. (2001); 3 Backman and Paresce (1993); 4 Jura (1991); 5 Song et al. (2001); 6 Barrado y Navascués et al. (1999); 7 Weinberger et al. (2000); 8 Lachaume et al. (1999); 9 Stauffer et al. (1995); 10 Song et al. (2000).

[a] No parallax was available, so the distance was estimated by assuming the absolute visual magnitude for an A1V star is +1.0 (Lang 1992, page 144), and using the measured visual magnitude of 7.298 from SIMBAD.

**Table 3.2:** Parameters of stars used in the analysis. The top part of the table shows objects with new sub-mm data, the bottom part shows objects where published data has been analysed. Spectral type and distance are from SIMBAD.

## 3.3 Data reduction

### 3.3.1 Maps

The basic steps in producing a map are to combine the data from each nod to remove systematic effects, flatfield the data to remove sensitivity variations between bolometers, correct the data for sky extinction and finally re-grid the data to make a regularly sampled image.

To remove the effects of sky extinction, the opacity of the atmosphere must be known. There are two ways of measuring this. Firstly, every couple of hours a skydip is performed, in which SCUBA is used to measure the emission from the sky as a function of altitude. These data can then be used to fit a model of the atmosphere, which gives the opacity. Alternatively, data from the nearby CSO Tau Monitor can be

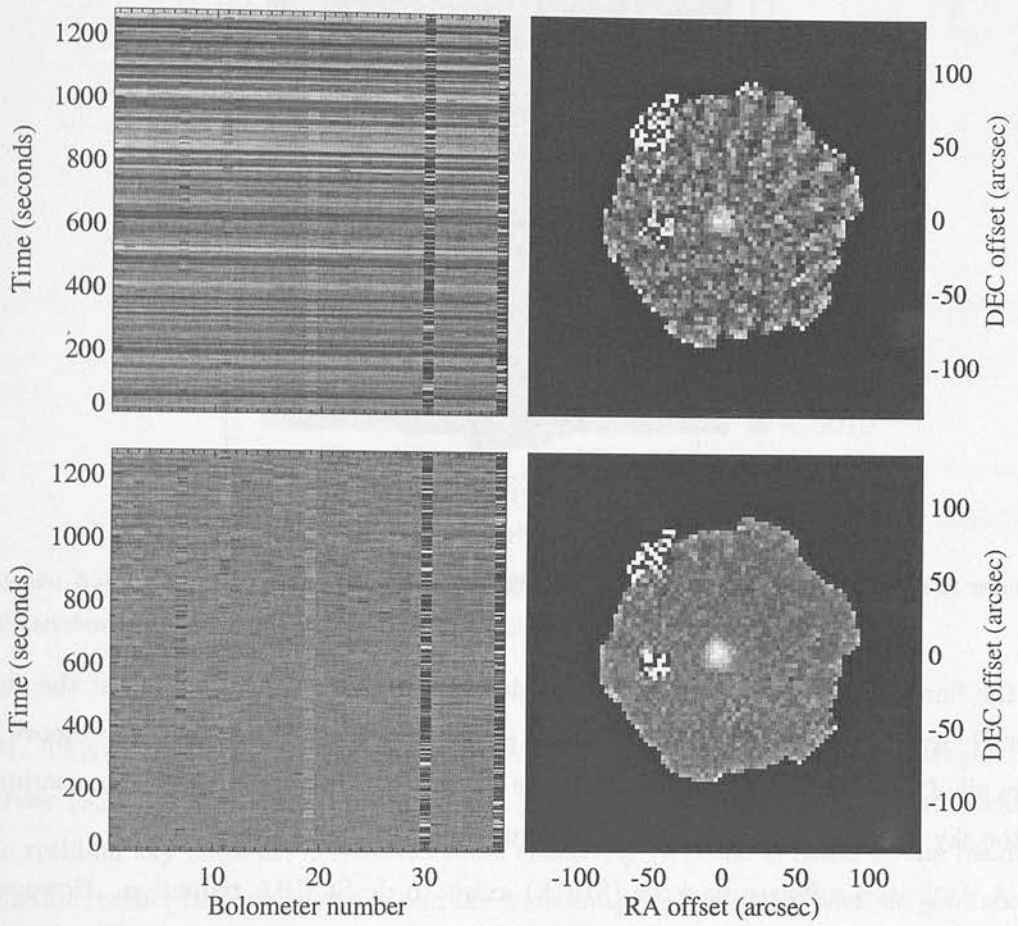


**Figure 3.2:** Example of the sky subtraction method. On the left is the raw bolometer data as a function of time, on the right is the rebinned data. The top panels shows the original data, the bottom panels show the data after the median sky signal is removed from each jiggle position.

used. The CSO Tau Monitor is a sensor dedicated to measuring the sky opacity. This has the advantage that a skydip is performed every ten minutes, but the disadvantage that the measurement is made at 1100 $\mu$m instead of 850 $\mu$m, so an empirical relation must be used to determine the 450 and 850 $\mu$m opacity.

In addition to the basic steps outlined above, it is usually possible to improve on the sky subtraction provided by chopping. This is because there is usually a gradient in the sky emission, so chopping does not completely remove the sky signal. This produces a signal which is correlated across the whole array and is different for each jiggle position (the signal changes on a time-scale of a few seconds), creating a patchwork appearance

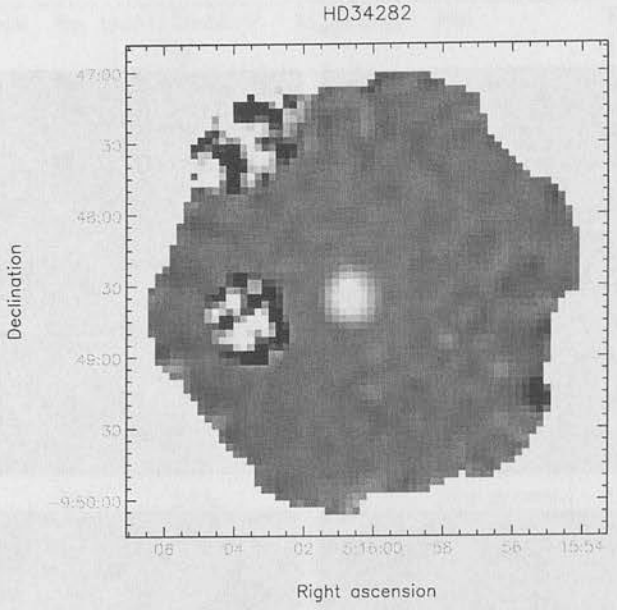


**Figure 3.3:** Map of HD34282 produced using SURF.

on the final map. However, if there are bolometers which are just looking at the sky, then these can be used to measure the sky signal in each jiggle position and remove it from all of the bolometers. This step is done before the data are regridded. An example of the sky removal process is shown in Figure 3.2.

A dedicated software package (SURF) exists to do SCUBA reduction. However, this software was not ideal for this data reduction for several reasons. Firstly, the rebinning methods available in SURF implicitly smooth the data, which means that each pixel of the final map is not an independent measurement, and it is therefore not obvious how to calculate uncertainties on measured quantities. Secondly, the sky subtraction method provided in SURF works by removing a uniform signal from each jiggle, whereas a better solution is to fit a plane to the data, and then subtract this. Thirdly, there is no support for using CSO tau to calculate sky opacities, though this method is likely to be more accurate, as skydips are taken so infrequently. Finally, it is difficult to automate SURF, as typical reduction in SURF has a lot of user interaction, e.g. identifying noisy bolometers and choosing which bolometers should be used for sky subtraction. As CSO tau opacities cannot be used, the results and times of two skydips must be manually selected for each observation, and once a map is produced there is no way to automatically measure the signal from the source: a typical approach is to export the data to AIPS to do this.

Map data were therefore reduced using custom data reduction software written in

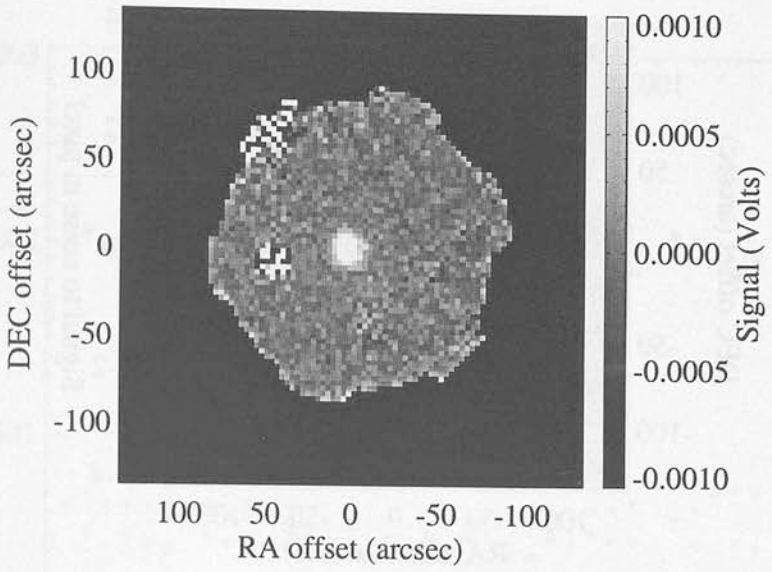


**Figure 3.4:** Map of HD34282 produced using the new reduction system. Here, the noise is independent on each pixel, which makes it much simpler to fit a model to the data.

IDL. This system is similar to that developed to reduce data for the 8-mJy extragalactic survey (Scott et al. 2002). This method is preferred over the SURF software because the residual sky emission is removed more effectively (a plane is fitted to the residual emission, rather than a constant), and the 'zero footprint' rebinning method produces a map where each pixel is an independent measurement, which makes subsequent analysis much simpler. In this method, the position of each bolometer on the sky plane is calculated for each data point, accounting for the location of the bolometers at the focal plane, the jiggle offset on the secondary mirror, and sky rotation (SCUBA has no field rotator). This gives a list of bolometer positions and the signal recorded at that position. Then, the signal in each pixel of the final image is simply the average of all the data points that fell within that pixel over the course of the observations. The data are weighted using the measured bolometer noise, so noisy bolometers do not degrade the map, so long as good data points are also available. Source flux was measured by fitting an elliptical Gaussian to the source. To ensure that the software was reliable, SURF was used to reduce several sources, and the results from the two reduction systems were compared to ensure that any differences were well within the errors. For comparison, the final maps of AB Aur produced by both the new reduction system and SURF are shown in Figures 3.3 to 3.5. The map produced with the new reduction system appears cosmetically worse than the SURF map, but this is due to

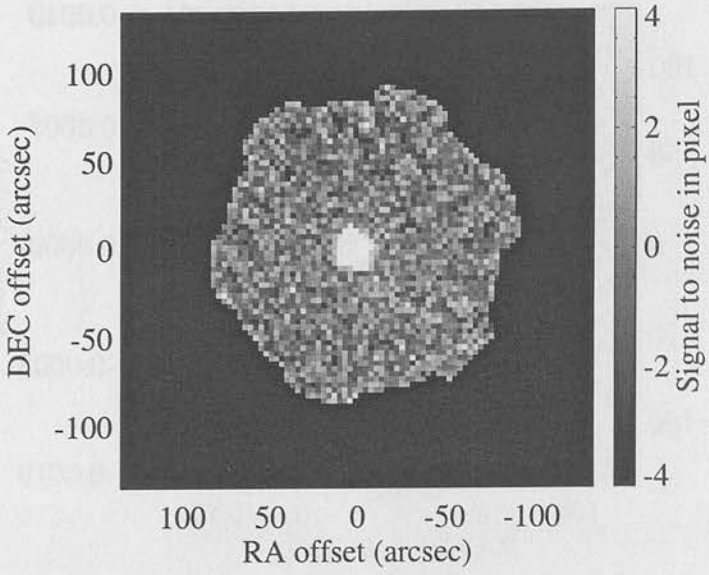


**Figure 3.5:** Signal to noise map for AB Aur produced with the new system.

the smoothing used by SURF. Smoothing does improve the appearance of the map, but it also creates correlated noise which makes the data much more difficult to interpret. For example, fitting routines will tend to overestimate the significance of any features in the map, as they usually assume that each pixel is an independent measurement.

The new sky subtraction method is also an improvement on typical SURF sky subtraction. The method is more effective because a plane is a better model of the sky emission than a constant, and also because the new method takes into account the measured noise on each bolometer when fitting the plane. The results of the sky subtraction are shown in Figure 3.6.

Flux calibration is done by mapping a calibration source, and either measuring the peak signal, or the integrated signal within an aperture. The same measurement (peak or integrated signal) is made on the source map. Given the flux of the calibrator, the flux of the source can be calculated. Using the peak signal rather than the integrated signal means that the measurement is sensitive to changes in the beam shape (Dunne and Eales 2001), but this approach was necessary as most of the calibration sources were secondary calibrators, and only the peak signal is well determined for these sources.

### 3.3.2 Photometry data

Photometry data were reduced using the SURF package. After combining the positive and negative beams, the data were flat-fielded and corrected for atmospheric extinction,

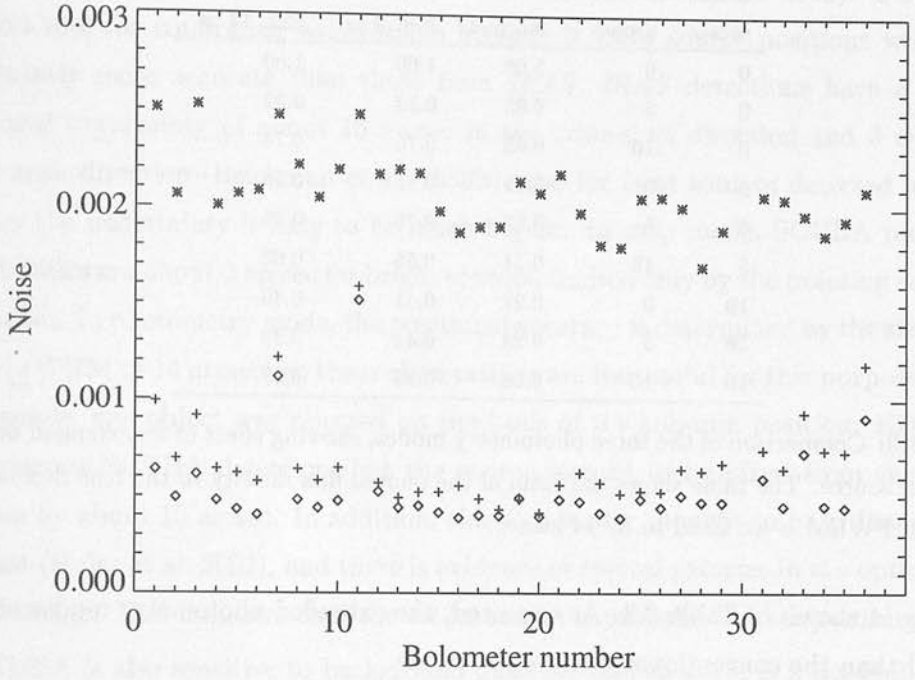


**Figure 3.6:** Comparison of the different sky subtraction methods. Asterisks show the noise on each bolometer before sky subtraction, crosses show the noise after a constant is removed from the data, diamonds show the noise when a plane is fitted and removed. The improvement is most significant towards the edge of the array (e.g. bolometer 19 is the central bolometer, and the new sky subtraction does not reduce sky noise here).

estimated using the CSO tau data and the relations in Archibald et al. (2000). Residual sky emission was estimated using bolometers well separated from the source, and this signal was subtracted from the data. The sky bolometers were those in rings 2 and 3 (30 bolometers in total), and their median was taken as the average sky signal. The signal from the central bolometer was then despiked using a 4 sigma cut.

Calibration sources were observed and reduced in exactly the same way as the targets. If a planet was used as a calibrator, the FLUXES package was used to estimate the flux and a correction was made for the loss of flux because the object was resolved. For the observations taken with the extended photometry mode, all of the calibration sources were point-like (i.e. secondary calibrators, not planets). Thus the final photometry is derived under the assumption that the emission is point-like and centred on the star. If a target is extended (i.e. marginally resolved) or is offset from the position of the star, then observations in photometry mode will underestimate the true flux, by

| Offset | FWHM | Relative response | | |
|---|---|---|---|---|
| arcsec | arcsec | Normal | Ext. 9 pt. | Ext. 12 pt. |
| 0 | 0 | 1.00 | 1.00 | 1.00 |
| 0 | 5 | 0.89 | 0.93 | 0.92 |
| 0 | 10 | 0.68 | 0.76 | 0.75 |
| 5 | 0 | 0.72 | 0.81 | 0.79 |
| 5 | 5 | 0.67 | 0.76 | 0.75 |
| 5 | 10 | 0.54 | 0.65 | 0.63 |
| 10 | 0 | 0.27 | 0.41 | 0.40 |
| 10 | 5 | 0.28 | 0.41 | 0.39 |
| 10 | 10 | 0.28 | 0.39 | 0.37 |

**Table 3.3:** Comparison of the three photometry modes, showing effect of an extended or offset Gaussian source. The table shows the ratio of the quoted flux density to the true flux density. The PSF FWHM is assumed to be 14 arcsec.

an amount shown in Table 3.3. As expected, the extended photometry modes are less affected than the conventional photometry mode.

## 3.4 Results

The results of the sub-mm observations are shown in Table 3.4. For objects with multiple observations, the flux given is the weighted mean of all the data. Of the 15 objects observed, 7 were not detected, 4 were detected at 850 $\mu$m and 450 $\mu$m, and 4 were detected at 850 $\mu$m only.

Most of the objects have not been observed in the sub-mm before, but for objects with existing observations, the new data were checked for consistency with the old results. HD34282 and HD35187 have both been observed with UKT14 (Sylvester et al. 1996): HD34282 had a flux of $1.3 \pm 0.3$ Jy at 400 $\mu$m and $0.409 \pm 0.027$ Jy at 800 $\mu$m, HD35187 had a flux of $0.115 \pm 0.022$ Jy at 800 $\mu$m. The discrepancy between these fluxes and the new data is small (2 sigma), however similar discrepancies have been found in other comparisons of UKT14 and SCUBA data (e.g. Sylvester et al. 2001). This may be due to calibration errors in the original data.

One of the advantages of SCUBA observations is that they can confirm the *IRAS* excess is associated with the star, and not simply a background source (i.e. a galaxy or galactic cirrus). Contamination by background sources is a significant problem, and follow up observations are important to confirm that the *IRAS* associations are real. Certainly, not all *IRAS* associations are real, as demonstrated by observations

of 55 Cnc (Jayawardhana et al. 2002) and HD155826 (Lisse et al. 2002). SCUBA is a useful tool for confirming associations because it gives source positions which are significantly more accurate than those from *IRAS*. *IRAS* detections have a typical positional uncertainty of about 16 arcsec in the cross-scan direction and 3 arcsec in the in-scan direction (Beichman et al. 1988b), and for faint sources detected at 60 or 100 $\mu$m the uncertainty is likly to be much higher. In map mode, SCUBA positional uncertainties are about 2 arcsec for bright sources, limited only by the pointing accuracy of the dish. In photometry mode, the positional accuracy is determined by the size of the beam (FWHM of 14 arcsec) so these observations are less useful for this purpose. From this sample, one object was rejected on the basis of it's sub-mm position: HD123160 was a strong SCUBA detection, but the source seemed to be offset from the stellar position by about 10 arcsec. In addition, this star is now thought to be a distant class III giant (Kalas et al. 2002), and there is evidence of several galaxies in the optical DSS survey image. This indicates that the *IRAS* source is probably a background galaxy.

SCUBA is also sensitive to background galaxies, and so there is a possibility that a background galaxy could fall into the beam of the observations and cause a spurious detection. The chances of this happening depend on the limiting flux of the observations (as there are many more faint galaxies than bright ones) and the size of the beam. The extended photometry mode is therefore more susceptible to this problem, as it is sensitive to sources over $\sim 2$ times more area than conventional photometry. The tentative detection of HD38393 has the highest probability of being due to a background galaxy, as the source is extremely faint and the observations were taken in extended photometry mode. This possibility is discussed further in Section 3.6.8.

Sub-mm fluxes can be used to obtain an estimate of the mass of a dust disk, as the emission is optically thin. This was done using the 850 $\mu$m flux, and a dust temperature determined from the peak of the dust emission SED. The results are shown in Table 3.4. The mass absorption coefficient was set to $\kappa = 1.7$ cm$^2$ g$^{-1}$ at 850 $\mu$m for consistency with previous work (e.g. Zuckerman and Becklin 1993; Holland et al. 1998b; Sylvester et al. 2001). Detailed discussion of the value of $\kappa$ can be found in Pollack et al. (1994). It is important to note that this mass estimate cannot measure the mass held in grains larger than about 1 mm. This is a key point, as in a collisional cascade (see Section 3.5.3), the total mass of the disk is dominated by the contribution from large bodies, which contribute little to the 850 $\mu$m emission. The mass estimate only reflects the amount of mass held in small dust grains, and even then is model dependent. The dust masses of the new targets are comparable with those measured in previous

| Object | Flux (Jy) | | $T_{\rm dust}$ | Dust mass |
|---|---|---|---|---|
| | 450$\mu$m | 850$\mu$m | K | $M_{\rm moon}$ |
| HD17206 | $< 0.1789$ | $< 0.0078$ | | $< 0.33^a$ |
| HD23362 | $< 0.17$ | $< 0.012$ | | $< 248^a$ |
| HD34282 | $1.925 \pm 0.29$ | $0.384 \pm 0.023$ | | $3 \times 10^{4\ b}$ |
| HD34700 | $0.218 \pm 0.037$ | $0.0407 \pm 0.0024$ | | $> 286^a$ |
| HD35187 | $0.268 \pm 0.047$ | $0.061 \pm 0.005$ | | $298^a$ |
| HD38393 | $< 0.0428$ | $0.0024 \pm 0.001$ | 82 | 0.04 |
| HD48682 | $< 0.0368$ | $0.0055 \pm 0.0011$ | 99 | 0.3 |
| HD69830 | $< 2.0248$ | $< 0.1005$ | | $< 3.5^a$ |
| HD81515 | $< 0.26$ | $< 0.02$ | | $< 49.7^a$ |
| HD109085 | $< 0.0381$ | $0.0075 \pm 0.0012$ | 85 | 0.6 |
| HD121617 | $< 0.36$ | $< 0.012$ | | $< 85$ |
| HD123160[c] | $0.152 \pm 0.046$ | $0.021 \pm 0.007$ | | |
| HD139664 | $< 0.39$ | $< 0.015$ | | $< 1.0^a$ |
| HD141569 | $0.066 \pm 0.023$ | $0.014 \pm 0.002$ | 90 | 33 |
| HD207129 | $< 1.7$ | $< 0.018$ | | $< 0.95^a$ |
| $\sigma$ Boo | | $0.0062 \pm 0.0017$ | 62 | 0.5 |
| $\epsilon$ Eri | $0.225 \pm 0.010$ | $0.040 \pm 0.0015$ | 85 | 0.1 |
| $\beta$ Pic | | $0.104 \pm 0.010$ | 103 | 7.8 |
| HR4796 | $0.180 \pm 0.15$ | $0.0191 \pm 0.0034$ | 99 | 19 |
| Vega | | $0.0457 \pm 0.0054$ | 68 | 0.8 |
| Fomalhaut | $0.595 \pm 0.035$ | $0.097 \pm 0.005$ | 75 | 1.7 |

[a] Calculated assuming a dust temperature of 100 K.

[b] Taken from Piétu et al. (2003).

[c] Sub-mm emission is offset by 9 arcsec from the star, and is thought to be due to a galaxy (see Section 3.4).

**Table 3.4:** Photometry results and estimated dust masses for the sample. The top part of the table shows new data, the bottom part shows existing data. The dust temperature is estimated from the wavelength of maximum emission for the best fitting SED model. HD34700 only has a lower limit on its distance, and hence a lower limit on its dust mass is calculated. These mass estimates are consistent with existing estimates made for Fomalhaut, Vega, and $\beta$ Pic in Holland et al. (1998b) and for $\epsilon$ Eri in Greaves et al. (1998).

studies, ranging from 0.04 lunar masses (HD38393) to 33 lunar masses (HD141569) for the Vega excess stars, and hundreds of lunar masses or more for the pre-main sequence stars (HD34700, HD35187 and HD34282).

## 3.5 SED modelling

The key objective of the SED modelling is to determine the size of a Vega excess disk from just its SED. Because models have many free parameters, as much as possible was constrained using understanding of the physical processes taking place in the disks, in particular by setting the size distribution from theoretical arguments.

The model used here is a modified version of the model developed to fit the SED and sub-mm image of Fomalhaut (Wyatt and Dent 2002). The model is based on a collisional cascade, where small dust grains are continuously created by collisions between larger bodies. The only significant difference between the model used here and that used in Wyatt and Dent (2002) is that a simpler assumption is used about the spatial distribution of the dust (see Section 3.5.4 for details).

For this model to be accurate, the disk must be optically thin to radiation from the central star. If this is not the case, then the inner parts of the disk will shadow the outer parts from starlight, and a radiative transfer code would be needed to properly model the system. Objects where $L_{\rm dust}/L_{\rm star} > 0.01$ have therefore been excluded. This ensures that disks are optically thin, as long as the opening angle is more than 2°. Measured opening angles are generally larger than this, e.g. 7° for $\beta$ Pic (Heap et al. 2000). HD34282, HD34700, and HD35187 all have $L_{\rm dust}/L_{\rm star} > 0.1$, so these objects have not been included in this analysis.

### 3.5.1 Photometric data

Mid and far IR photometry data are taken from the *IRAS* faint source catalogue (Moshir et al. 1990). Where available, this is supplemented by ground based mid-IR data from the literature. Also, published *ISO* photometry has been added to help constrain the far-IR part of the SEDs (in particular data from Habing et al. 2001).

### 3.5.2 Dust grain properties

The model of the dust grains is based on the assumption that the grains in protoplanetary disks are aggregates of interstellar dust grains, with an additional ice component frozen into them as they grow. This type of model was originally developed to simulate cometary grains (Greenberg 1982, 1998), but it has also been successfully applied to the dust grains in accretion disks (Pollack et al. 1994), and to the debris disks of $\beta$ Pic (Li and Greenberg 1998), HR4796 (Augereau et al. 1999b; Li and Lunine 2003b), HD141569 (Li and Lunine 2003a) and HD207129 (Jourdain de Muizon et al. 1999).

| Object | $p$ | $q_{\rm ice}$ | $D_{\rm min}$ $\mu$m | Reduced $\chi^2$ | $R$ AU |
|---|---|---|---|---|---|
| Fomalhaut | 0.0 | | 9.6 | 4.2 | 150 |
| | 0.5 | 0.0 | 18.6 | 14.1 | 150 |
| | 0.9 | 0.0 | 91.0 | 23.2 | 150 |
| | 0.5 | 1.0 | 12.5 | 9.3 | 150 |
| HR4796 | 0.0 | | 10.9 | 16.8 | 70 |
| | 0.5 | 0.0 | 21.3 | 1.8 | 70 |
| | 0.9 | 0.0 | 105.2 | 3.2 | 70 |
| | 0.5 | 1.0 | 14.3 | 25.6 | 70 |
| Vega | 0.0 | | 28.3 | 4.2 | $120 \pm 13$ |
| | 0.5 | 0.0 | 55.9 | 4.9 | $191 \pm 16$ |
| | 0.9 | 0.0 | 281.4 | 4.7 | $237 \pm 21$ |
| | 0.5 | 1.0 | 37.2 | 5.4 | $92 \pm 8$ |
| $\epsilon$ Eri | 0.0 | | 0.74 | 33.6 | 60 |
| | 0.5 | 0.0 | 0.44 | 110.9 | 60 |
| | 0.9 | 0.0 | 0.51 | 139.4 | 60 |
| | 0.5 | 1.0 | 0.67 | 43.7 | 60 |
| | 0.0 | | 3.5 | 2.8 | 60 |
| | 0.0 | | 7.0 | 6.6 | 60 |
| | 0.0 | | 12.0 | 14.0 | 60 |
| ($q = 1.9$) | 0.0 | 1.0 | 0.74 | 25.6 | 60 |
| ($q = 1.8$) | 0.0 | 1.0 | 0.74 | 139.4 | 60 |
| ($q = 1.76$) | 0.0 | 1.0 | 0.74 | 808.9 | 60 |
| $\beta$ Pic | 0.0 | | 5.9 | 12.2 | $43.5 \pm 1.8$ |
| | 0.5 | 0.0 | 11.2 | 13.6 | $62.1 \pm 2.5$ |
| | 0.9 | 0.0 | 53.3 | 11.5 | $82 \pm 3$ |
| | 0.5 | 1.0 | 7.6 | 18.6 | $31.9 \pm 1.1$ |
| HD141569 | 0.0 | | 10.3 | 2.0 | $55.0 \pm 2.3$ |
| | 0.5 | 0.0 | 20.1 | 1.9 | $84 \pm 4$ |
| | 0.9 | 0.0 | 99.5 | 2.4 | $114 \pm 5$ |
| | 0.5 | 1.0 | 13.5 | 3.8 | $43.8 \pm 1.7$ |
| HD109085 | 0.0 | | 4.2 | 4.0 | $180 \pm 40$ |
| HD38393 | 0.0 | | 2.7 | 0.4 | $200 \pm 50$ |
| HD48682 | 0.0 | | 2.3 | 7.0 | $71 \pm 15^a$ |
| | 0.0 | | 2.3 | 3.1 | $110 \pm 21^b$ |
| $\sigma$ Boo | 0.0 | | 3.3 | 2.0 | $320 \pm 90$ |
| HD207129 | 0.0 | | 1.6 | 3.7 | $260 \pm 50$ |

[a] Assuming secondary does not contribute to *IRAS* fluxes

[b] Assuming secondary does contribute to *IRAS* fluxes

**Table 3.5:** Results of the SED fitting, where $p$ is the porosity of the grains, $q_{\rm ice}$ is the fraction of this porosity filled with ice, and $D_{\rm min}$ is the smallest dust grains in the system. $D_{\rm min}$ was determined by the blowout limit due to radiation pressure, except for $\epsilon$ Eri (see Section 3.6.3). Where no error is quoted on the disk radius, the size was constrained from existing images and was not a free parameter of the fits.

| Object | Flux (Jy) | | | |
|---|---|---|---|---|
| | 12 $\mu$m | 25 $\mu$m | 60 $\mu$m | 100 $\mu$m |
| Fomalhaut | $12.1 \pm 1.2$ | $3.9 \pm 0.3$ | $10.0 \pm 0.6$ | $10.7 \pm 0.6$ |
| HR4796 | | $4.2 \pm 0.4$ | $7.1 \pm 0.9$ | $3.6 \pm 0.4$ |
| Vega | $27.8 \pm 1.4$ | $9.3 \pm 0.5$ | $9.8 \pm 0.4$ | $7.6 \pm 0.4$ |
| $\epsilon$ Eri | $6.6 \pm 0.3$ | $2.18 \pm 0.11$ | $1.57 \pm 0.08$ | $1.99 \pm 0.22$ |
| $\beta$ Pic | | $10.6 \pm 0.4$ | $19.1 \pm 0.8$ | $10.4 \pm 0.4$ |
| HD38393 | $3.00 \pm 0.15$ | $0.69 \pm 0.04$ | $0.19 \pm 0.03$ | $< 0.5$ |
| HD48682 | $1.00 \pm 0.06$ | $0.29 \pm 0.03$ | $0.36 \pm 0.05$ | $< 1.0$ |
| HD141569 | | $2.29 \pm 0.05$ | $5.3 \pm 0.8$ | $4.1 \pm 0.5$ |
| $\sigma$ Boo | $1.10 \pm 0.05$ | $0.32 \pm 0.02$ | $0.13 \pm 0.04$ | $< 0.5$ |
| HD207129 | $0.60 \pm 0.03$ | $0.15 \pm 0.02$ | $0.31 \pm 0.04$ | $< 0.24$ |

**Table 3.6:** Colour corrected *IRAS* fluxes, based on the best fitting model. Upper limits are three sigma, and are taken directly from the *IRAS* faint source catalogue. HD109085 has been excluded because the best fitting model is unlikely to be representative of the true spectral shape at any of the *IRAS* wavelengths.

For the composition of the interstellar grains, the core-mantle model developed in Li and Greenberg (1997) is used, which successfully fits the observed interstellar extinction and polarisation data. This model has a silicate core surrounded by a UV-processed organic refractory mantle. The silicate/organic-refractory volume ratio is forced to be 1:2, as inferred for cometary grains (Greenberg 1998). The grains are assumed to be porous, with the porosity being a free parameter of the model. The gaps due to porosity may be filled with either vacuum, water ice or a mixture of the two. The free parameters in the dust composition model are therefore the porosity $p$ of the grains and the ice fraction $q_{\rm ice}$. Optical constants for the materials are taken from Li and Greenberg (1997, 1998), and the optical properties of the dust grains are calculated using the methods described in Section 2.4.

To be completely accurate, only grains cooler than $\sim 120$ K should contain ice, as for dust grains warmer than this most ices would sublime. This constraint was not included in the modelling because it is difficult to implement, but in most cases all of the dust grains are cooler than 120 K, so this does not affect the results. The two possible exceptions are $\beta$ Pic and HR4796, which both have quite warm disks. For these objects, the models with ices may be inaccurate.

### 3.5.3 Size distribution

The size distribution that results from an infinite collisional cascade (described more fully in Section 2.3) is (Dohnanyi 1969):

$$n(D) \propto D^{2-3q}, \tag{3.1}$$

where $n(D)dD$ is the number of planetesimals of size between $D$ and $D + dD$, and $q = 11/6$. However, this distribution will only hold for large dust grains, as radiation pressure will blow out small grains (e.g. $< 1$ $\mu$m) very rapidly, and Poynting-Robertson drag will cause intermediate sized grains (e.g. $< 10$ $\mu$m) to spiral inwards toward the star. Which of these two effects is dominant depends on the optical depth of the dust disk, but for all but the most tenuous disks the collisional timescale is shorter than the PR timescale, so PR drag can be safely ignored (Wyatt et al. 1999). Given this, the above size distribution is assumed to hold down to the radiation blowout limit, when $\beta > 0.5$ (where $\beta = F_{\rm rad}/F_{\rm grav}$), at which point there is a sharp cutoff.

### 3.5.4 Spatial distribution

For the spatial distribution of the dust grains, an infinitely thin, flat ring is assumed, with the ring's radius $R$ as a free parameter. This approach is motivated by the sub-mm images of Fomalhaut and $\epsilon$ Eri, which both show a narrow, well defined ring of emitting material. This spatial distribution is different to that used in Wyatt and Dent (2002), as here no attempt is made to account for a spread in orbital semimajor axes and eccentricities of the dust grains, which broadens the ring by about 50 AU. The advantage of the simpler model is that it reduces the number of free parameters, but should still give a reasonable estimate of the overall extent of the disk. The Fomalhaut results shown in Section 3.6.1 are almost identical to the results presented in Wyatt and Dent (2002), which indicates that this simplification will not affect the conclusions.

### 3.5.5 Stellar parameters

Accurate stellar parameters are needed for several reasons. Firstly, the photospheric flux must be estimated in each band, so that the excess flux due to dust can be determined. This is particularly important in the *IRAS* 12 and 25 $\mu$m bands, where the photosphere can be the dominant source of flux. Secondly, the temperature of the dust depends on the luminosity of the star, and on the shape of the star's spectrum in the region where most power is emitted (i.e. UV—optical—near-IR). The luminosity and

stellar spectrum also determine the magnitude of the radiation forces which act on the dust grains. Finally, an estimate of the mass of the star is needed to calculate the gravitational forces.

To determine the stellar parameters, the spectral type of each star was obtained from SIMBAD. This was used to estimate the star's effective temperature, using the calibration provided in Gray and Corbally (1994). A Kurucz model atmosphere with this effective temperature was then extracted, assuming solar metallicity and surface gravity $\log(g) = 4.3$ appropriate for dwarf stars. Kurucz model atmospheres are provided in a grid of temperature and surface gravity, so the model was produced by interpolating between the four models that bracketed the desired model in both parameters. The model atmosphere was then normalised to fit the K band magnitude. K band was preferred over optical photometry because it is less susceptible to the effects of reddening. The luminosity of the star was then calculated by integrating the normalised model atmosphere. Finally, the mass of the star was estimated using the observed spectral type and the table provided by Lang (1992, page 132).

### 3.5.6 Modelling method

A model SED is specified by the grain composition (porosity $p$, ice fraction $q_{\rm ice}$), radius of the dust ring ($R$), and the total dust luminosity. In the cases where the size of the dust ring is known, the ring radius is fixed to the observed size; for the unresolved objects the ring radius must be left as a free parameter. The approach taken here is to choose a dust composition, and then find the best fit to the data by varying the remaining free parameters.

As described in Chapter 2, the emission spectrum of an individual dust grain depends on its temperature, and on its emission efficiency as a function of wavelength. The SED of a disk is simply the combined emission of all the dust grains (so long as the disk is optically thin). For a given dust composition model, the absorption efficiency $Q_{\rm abs}$ was calculated as a function of grain size. Given this, the temperature of the dust grains as a function of grain size and distance from the star was determined by solving the thermal balance equation (Equation 2.19), locating the root using Newton's method. Then, the total flux as a function of wavelength was found by integrating over all grain sizes, weighting with the size distribution given in Equation 3.1. The programs to implement this method were all written in IDL. Calculation of $Q_{\rm abs}$ and $Q_{\rm pr}$ was done using programmes written by Mark Wyatt for the modelling of Fomalhaut's dust disk (Wyatt and Dent 2002), but I wrote new programs to calculate the grain

temperature and the total thermal emission of the disk. This was necessary to allow least-squares fitting to the data, as the original routines were too slow for this purpose. The new and old routines were checked to ensure they produced the same results.

The model spectrum was then converted into an SED that could be directly compared to the observed points to obtain a $\chi^2$ value. To do this, the spectral response of each filter-instrument combination was combined with the model spectrum, to estimate the broad-band flux that would be recovered from a real observation of the model spectrum. This step is particularly important for the *IRAS* data points, which have a very wide band-pass. By converting the model spectrum into broad-band fluxes, we avoid having to make colour-corrections to the original data, which would otherwise require detailed knowledge of the true spectrum of the source. If an astronomical spectrum $f_\nu$ is passed through an instrument, filter, and detector system which has a total response $R_\nu$, the resulting measured signal $S$ will be

$$S = \int_0^\infty d\nu \, f_\nu \, R_\nu. \tag{3.2}$$

Here $R_\nu$ is the relative response to radiation of equal power at different frequencies. To estimate what the quoted monochromatic flux would be, the conversion from signal $S$ into quoted flux $F$ must be known. IRAS and ISO make this conversion with the assumption that the source spectrum is constant in flux per logarithmic frequency interval, i.e. of the form

$$f_\nu \propto \nu^{-1}. \tag{3.3}$$

The relationship between signal and flux can be established from this assumed spectrum. If the centre of the filter is $\nu_0$, then the following spectrum will have a monochromatic flux of 1.0 at $\nu_0$:

$$f_\nu^{\rm flat} = \nu_0 \, \nu^{-1}. \tag{3.4}$$

As this spectrum is of the form specified in Equation 3.3, it must also have a quoted flux $F$ of 1.0. The signal produced by this spectrum would be

$$S = \int_0^\infty d\nu \, \nu_0 \, \nu^{-1} \, R_\nu. \tag{3.5}$$

The relationship between signal and quoted flux must therefore be

$$\frac{F}{S} = \frac{1.0}{\int_0^\infty d\nu \, \nu_0 \, \nu^{-1} \, R_\nu}. \tag{3.6}$$

The quoted flux of a real spectrum $f_\nu^*$ is then

$$F^* = \frac{\int_0^\infty d\nu \, f_\nu^* \, R_\nu}{\int_0^\infty d\nu \, \nu_0 \, \nu^{-1} \, R_\nu}. \tag{3.7}$$

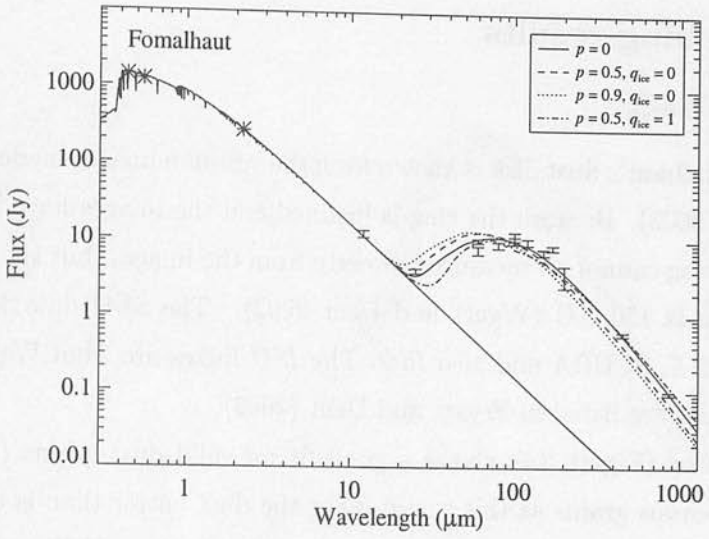


**Figure 3.7:** SED of Fomalhaut and model fits with the ring radius set at 150 AU. Asterisks show optical and near-IR photometry, *IRAS*, *ISO* and SCUBA data are shown with error bars. Colour corrections for the *IRAS* data were estimated from the $p = 0$ model.

This procedure allows an unambiguous photosphere subtraction, and model fit. Fitting was done using the IDL package MPFIT, which uses a modified Levenberg-Marquardt algorithm. The uncertainty on the fitted dust ring radius was calculated by doing a Monte-Carlo simulation. Synthetic datasets were produced by perturbing the observed datapoints using a normal distribution scaled to the estimated uncertainties. The fitting was redone with each synthetic dataset, and the standard deviation in the fitted radius is taken to be the uncertainty.

When showing the result of the fit, a colour-correction must be applied so that the data points can be plotted in real units. For this purpose, the best fitting model is used to estimate the colour correction for each point. If the best model is more than 3 sigma away from a data point, then no colour-correction is applied to that point, as the model is not likely to give a good estimate of the true colour-correction.

For some objects it is impossible to fit all the data points simultaneously, because there is dust at a range of distances from the star. In these cases, only the long wavelength points are fitted, in order to obtain an estimate of the overall extent of the ring.

## 3.6 Modelling results

### 3.6.1 Fomalhaut

The size of Fomalhaut's dust disk is known from the sub-mm images made with SCUBA (Holland et al. 2003). Because the ring is inclined and the images have low resolution the size of the ring cannot be measured directly from the images, but the best estimate of the true size is 150 AU (Wyatt and Dent 2002). The SED data for Fomalhaut comes from *IRAS*, SCUBA and also *ISO*. The *ISO* fluxes are from Walker et al. (in preparation), and are listed in Wyatt and Dent (2002).

The modelling (Figure 3.7) shows a good fit for solid dust grains (i.e. $p = 0.0$), but rules out porous grains as this would make the dust hotter than is observed. The $p = 0.5$, $q_{\rm ice} = 1.0$ model is also ruled out, as it fails to fit the mid-IR part of the SED.

The reduced $\chi^2$ for the best fitting model is 4.2, which indicates that the model is not consistent with the data. However, by far the dominant contribution to $\chi^2$ comes from the *ISO* data, which show considerable scatter from any smooth model. The *ISO* filters all have broad band passes ($\Delta\lambda/\lambda \sim 0.5$), so the apparent scatter in the *ISO* points is unlikely to be due to structure in the spectrum. A more likely explanation is that uncertainties on the *ISO* points have been underestimated, and this would explain the high reduced $\chi^2$.

Fomalhaut has already been modelled in detail by Wyatt and Dent (2002), and the results here are almost identical to those results. As the modelling here uses the same data and dust grain model, it is hardly surprising that the same results are recovered. However, this does confirm that the simpler spatial distribution used here does not significantly affect the results of the modelling.

### 3.6.2 HR4796

HR4796 is resolved in both mid-IR images of dust emission (Koerner et al. 1998; Jayawardhana et al. 1998) and scattered light images in the near-IR (Schneider et al. 1999). The best estimate of the size of the ring comes from mid-IR images, which suggest that the radius is 70 AU. The star is younger than most of the other stars in the sample, with an age of $8 \pm 2$ Myr (Stauffer et al. 1995).

The modelling results show that solid dust grains are unable to fit the observed SED and disk size (Figure 3.8). However, using a porosity of $p = 0.5$ provides a good fit to the SED. The icy model ($p = 0.5$, $q_{\rm ice} = 1.0$) is a worse fit than the solid grain model, so can be rejected. Around 10 $\mu$m, there is an additional excess which cannot

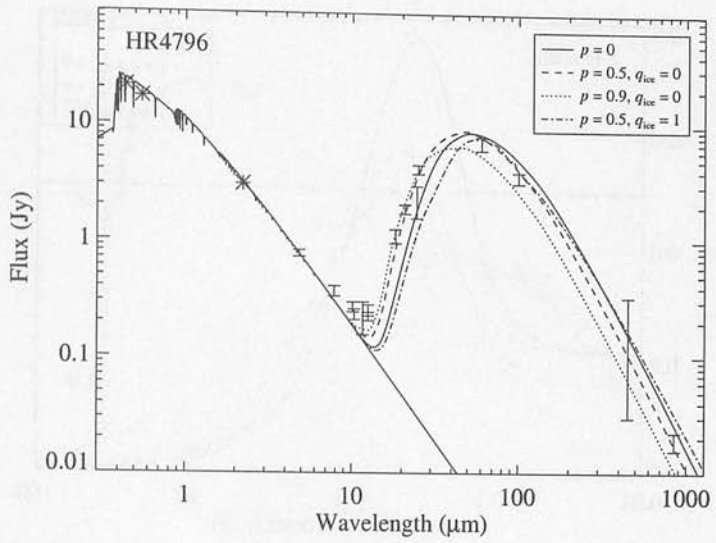


**Figure 3.8:** SED of HR4796 and model fits with the ring radius set at 70 AU. Data where the wavelength is shorter than 18 $\mu$m has been excluded from the fit, as the excess here is probably due to a hot dust component close to the star (see Section 3.6.2). Upper limits are 3 sigma. Colour corrections for the *IRAS* data were estimated from the $p = 0.5$, $q_{\rm ice} = 0$ model.

be accounted for by any model. This is likely to be produced by a hot dust component close to the star. Data in this part of the spectrum have therefore been excluded from the fit, and do not contribute to the total $\chi^2$ quoted in Table 3.5.

Detailed modelling of this object has been done previously by Augereau et al. (1999b), and the results here are in good agreement with this work. Augereau et al. made a much more thorough exploration of parameter space, but their overall conclusion was that two dust populations are required: a cool component at 70 AU, and a hotter component at about 10 AU. Their best fitting model for the cool dust has amorphous grains with a porosity of $p = 0.6$ and an ice fraction ice $q_{\rm ice} = 0.03$. In their analysis, the ring's diameter was constrained to be 70 AU, but the grain porosity, ice fraction and the width of the dust ring were all left as free parameters. As for Fomalhaut, these results confirm that the simpler model used here is able to produce similar results to a more detailed model.

Modelling of HR4796 has also been done by Li and Lunine (2003b), and they were able to fit the entire SED without having a hot dust component, in contrast to the results of Augereau et al. (1999b) and the results presented here. This discrepancy is probably because Li and Lunine's model contains a large number of grains which are much smaller than the blowout diameter, and these small grains produce a hot component in the SED even though they are distant from the central star.

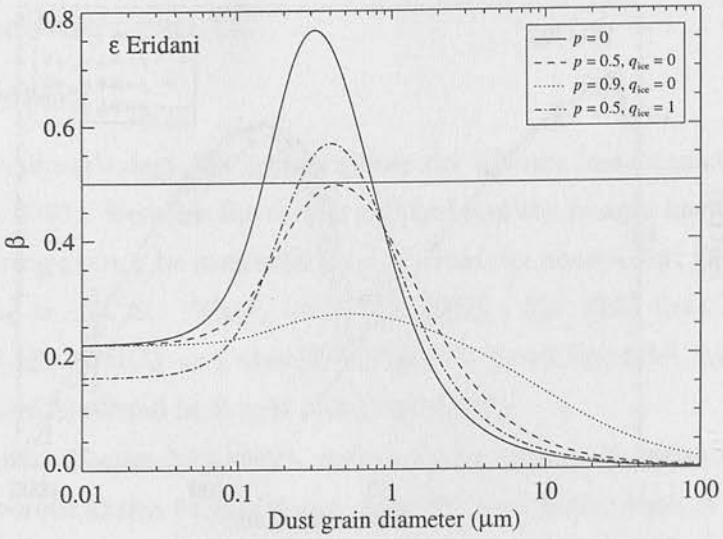


**Figure 3.9:** Graph showing how $\beta$ ($= F_{\rm rad}/F_{\rm grav}$) depends on dust grain size, for dust orbiting $\epsilon$ Eri. $\beta = 0.5$ is shown by the horizontal line; any dust grain with $\beta > 0.5$ will leave the system on a hyperbolic trajectory.

### 3.6.3 $\epsilon$ Eri

$\epsilon$ Eri is a particularly interesting object, as it the only cool star (K2V) with a resolved dust disk, all other resolved disks being around A stars. SCUBA images of $\epsilon$ Eri show a distinct ring, which is approximately face on and has a radius of 60 AU (Greaves et al. 1998).

In modelling $\epsilon$ Eri's dust disk, a problem arises due to the low luminosity of the star. The model for the dust size distribution assumes that radiation pressure will remove the smallest dust grains. However, in the case of $\epsilon$ Eri the radiation pressure is not sufficient to blow dust grains out of the system when porous dust grains are used (Figure 3.9). In this situation, it is not clear what limits the size of the smallest dust grains. As a first step, the ad-hoc assumption was made that when porous grains were used, the small size cutoff is set at the grain size where $\beta$ is greatest, i.e. where the radiation force is most significant compared to the gravitational force. Modelling using this assumption produced a very interesting result: all of the models predict too much flux in the mid-IR, and too little in the sub-mm (Figure 3.10). This means that the models have too many small (and therefore hot) dust grains. This is an unexpected result, as there is no obvious mechanism for removing the small grains. By varying the minimum size cutoff explicitly, an excellent fit is possible, but only if the cutoff size is set to 3.5 $\mu$m and the $p = 0$ model is used, as shown in Figure 3.11. Solid dust grains

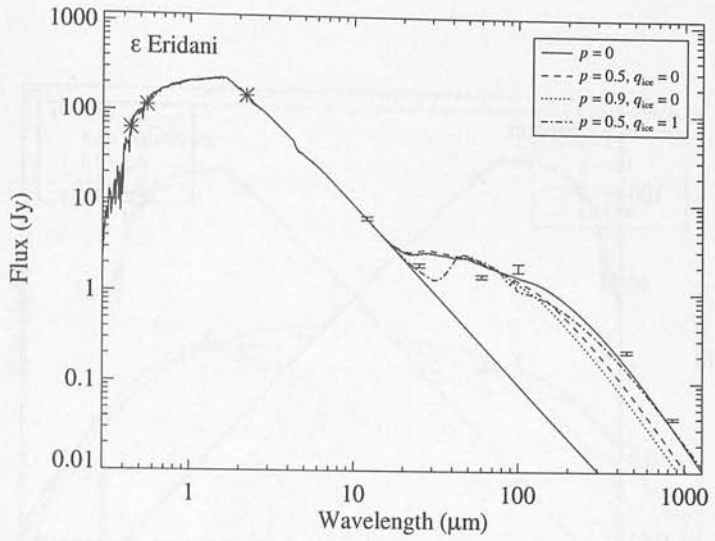


**Figure 3.10:** SED of $\epsilon$ Eri, with the ring radius set at 60 AU. Colour corrections for the *IRAS* data as plotted here were estimated from the $p = 0$ model.

with a size of 3.5 $\mu$m have a $\beta$ of about 0.15, much less than is needed to remove the grains by radiation pressure. It therefore seems that the disk around $\epsilon$ Eri contains few grains smaller than about 3 $\mu$m, and radiation pressure from the star cannot explain this deficiency. Possible causes for this discrepancy are discussed in Section 3.7.

It is also possible to obtain a good fit using porous grains, but only if the minimum size cutoff is set to around 300 $\mu$m (Figure 3.12). This model does not predict the observed excess at 25 $\mu$m, but this flux could come from an additional hot component close to the star. Modifying the slope of the size distribution can improve the fit (Figure 3.13), but cannot make the model consistent with the data.

### 3.6.4 Vega

The original estimate for the size of Vega was made by Aumann et al. (1984), who analysed special pointed observations made with *IRAS* after the discovery of a far-IR excess. The estimated diameter was 23 arcsec at 60 $\mu$m (corresponding to a radius of 90 AU). Subsequently, these data was reanalysed, giving a larger diameter of $35 \pm 5$ arcsec (135 AU) (van der Bliek et al. 1994, and references therein). This discrepancy is attributed to the fact the Aumann et al. did not account for the photospheric emission at 60 $\mu$m, and hence underestimated the extent of the excess emission. However, sub-mm observations made with SCUBA on the JCMT indicate a diameter of $24 \pm 3$ arcsec (Holland et al. 1998b), similar to the original estimate from the *IRAS* data. At

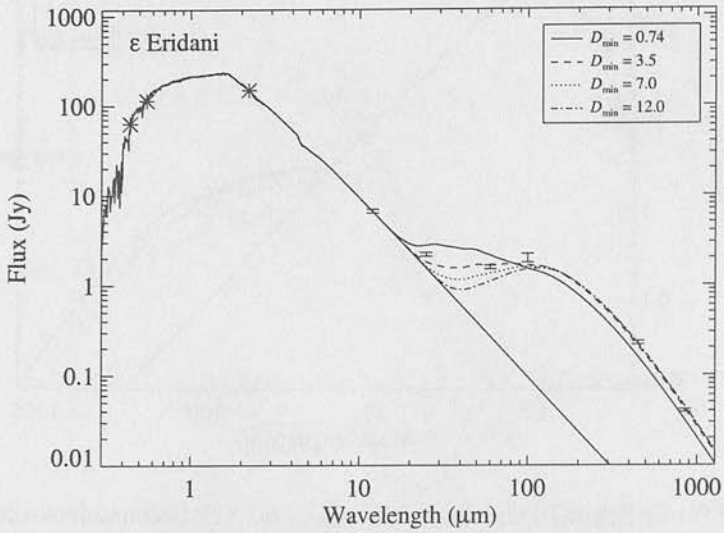


**Figure 3.11:** SED of $\epsilon$ Eri, with the ring radius set at 60 AU. Models show the effect of changing the minimum size cutoff when using solid grains ($p = 0$). Colour corrections for the *IRAS* data were estimated from the $D_{\rm min} = 3.5$ $\mu$m model.

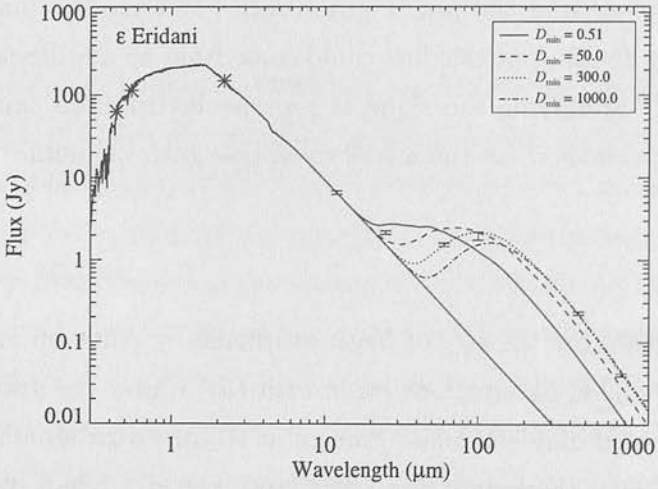


**Figure 3.12:** SED of $\epsilon$ Eri, with the ring radius set at 60 AU. Models show the effect of changing the minimum size cutoff when using porous grains ($p = 0.9$). Colour corrections for the *IRAS* data were estimated from the $D_{\rm min} = 300$ $\mu$m model.

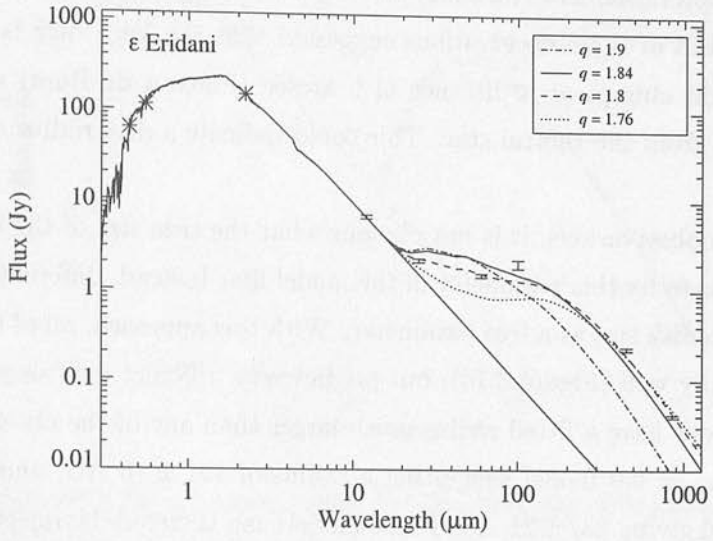


**Figure 3.13:** SED of $\epsilon$ Eri, with the ring radius set at 60 AU. Models show the effect of changing the slope of the size distribution ($q$). Colour corrections for the *IRAS* data were estimated from the $q = 1.8$ $\mu$m model.

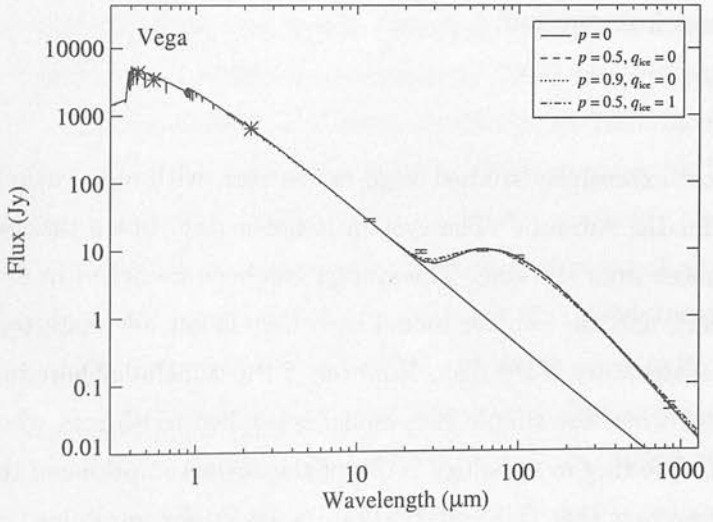


**Figure 3.14:** SED of Vega and model fits to the data with ring radius as a free parameter. Colour corrections for the *IRAS* data as plotted here were estimated from the $p = 0$ model.

millimetre wavelengths, aperture synthesis imaging has been done using the Plateau de Bure interferometer (Wilner et al. 2002) and Owens Valley Radio Observatory (Koerner et al. 2001). Both of these observations suggested that the Vega disk is very clumpy, and found bright clumps at a distance of 9 arcsec (Plateau de Bure) and 12 arcsec (Owens Valley) from the central star. This could indicate a disk radius as small as 70 AU.

Given these observations, it is not obvious what the true size of the disk is, and it was not possible to fix this parameter in the model fits. Instead, different grain models were fitted with disk size as a free parameter. With this approach, all of the dust grain models fit equally well (Figure 3.14), but predict very different disk sizes. The porous grain models both have a fitted radius much larger than any of the observations, with the $p = 0.5$, $q_{\rm ice} = 0.0$ model suggesting a radius of $191 \pm 16$ AU, and the $p = 0.9$, $q_{\rm ice} = 0.0$ model giving $237 \pm 21$ AU. These models can therefore be rejected. However, the solid grain model ($p = 0.0$) gives a radius of $120 \pm 13$ AU, and the icy $p = 0.5$, $q_{\rm ice} = 1.0$ model gives $92 \pm 8$ AU, both of which are compatible with the observations. Without more detailed analysis of the structure observed in the disk, it is impossible to distinguish between these two options.

There is a small additional excess at 25 $\mu$m ($\sim$ 2 Jy), which none of the models account for. This could either be due to an additional warm dust component similar to that found for HR4796, or because the spatial distribution is broad, with dust at a range of distances from the star.

### 3.6.5 $\beta$ Pic

$\beta$ Pic is the most extensively studied Vega excess star, with observations in scattered light, mid-IR, far-IR, sub-mm. The system is not a ring, but a disk with dust at a variety of distances from the star. The system has been modelled in detail by Li and Greenberg (1998), and the simpler model used here is not adequate to deal with the extended spatial structure of the disk. However, $\beta$ Pic is included here in order to show the consequences when the simple ring model is applied to objects where the dust is really in a disk. The ring morphology is one of the key assumptions of the model, so it is extremely important that this assertion can be tested for unresolved objects.

The SED was fitted using the same approach taken for Vega, i.e. the ring radius is left as a free parameter, and each dust composition model is fitted to the SED. The modelling shows that it is not possible to fit the observed SED with any single model regardless of what dust composition is chosen (Figure 3.15). This is a helpful result, in

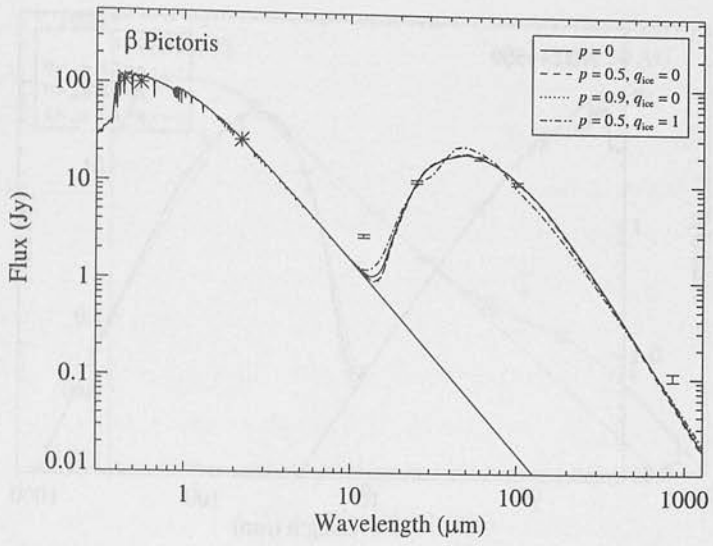


**Figure 3.15:** SED of $\beta$ Pic and model fits to the data with ring radius as a free parameter. Colour corrections for the *IRAS* data as plotted here were estimated from the $p = 0$ model.

that it shows that it is possible to distinguish between a disk and a ring morphology purely from the SED. However, this modelling reveals little else about the composition and size distribution of dust grains in $\beta$ Pic.

### 3.6.6 HD141569

HD141569 has a resolved circumstellar disk, first directly detected in near-IR scattered light images (Augereau et al. 1999a; Weinberger et al. 1999), and subsequently resolved in mid-IR thermal emission (Fisher et al. 2000; Mouillet et al. 2001; Marsh et al. 2002). Most recently, the disk has been observed with the ACS coronagraph (Clampin et al. 2002), revealing that the structure observed in the disk is probably caused by a tidal interaction with a bound binary system at a projected distance of around 1000 AU. The age of the system has been estimated to be $5 \pm 3$ Myr (Weinberger et al. 2000), making it one of the youngest stars in the sample. However, despite its youth the disk appears to be in a collisional cascade, as modelling shows that it contains small dust grains which must leave the system on a very short timescale (Fisher et al. 2000).

The mid-IR imaging shows that the overall size of the disk is around 100 AU, but the emission is produced at a range of distances from the star from 20 AU outwards (Marsh et al. 2002). This is also apparent from the SED modelling, as no model can simultaneously fit all the data (Figure 3.16). When only the long wavelength points are fitted (i.e. only the cooler, outer parts of the disk), the fitted radius is about 50 AU if

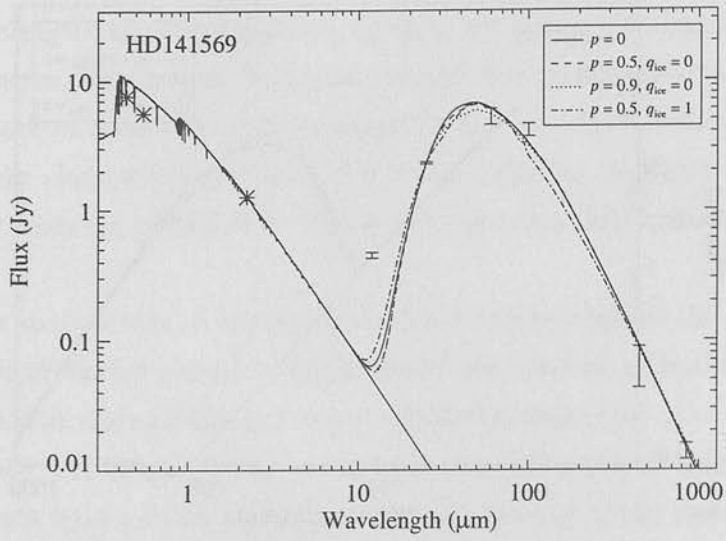


**Figure 3.16:** SED of HD14159 with model fits for different grain compositions. The ring radius is a free parameter in each case. Colour corrections for the *IRAS* data as plotted here were estimated from the $p = 0$ model.

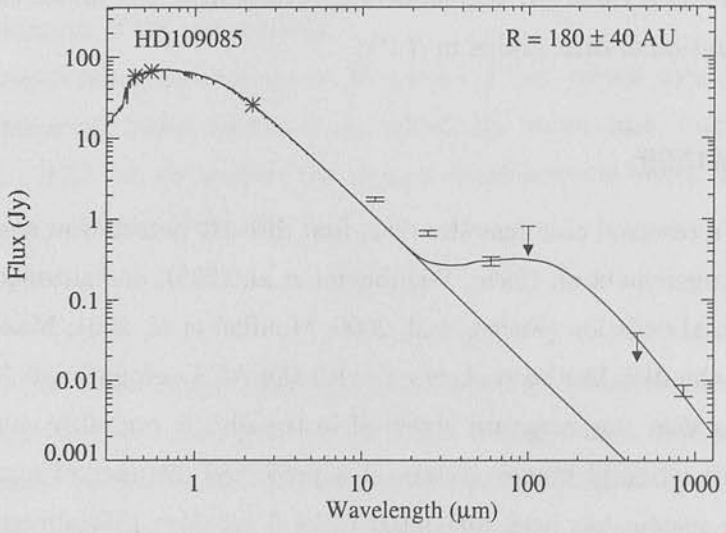


**Figure 3.17:** SED of HD109085 with model fit to the data. Ring radius is a free parameter. Upper limits are 3 sigma.

solid ($p = 0$) or icy ($p = 0.5$, $q_{\rm ice} = 1.0$) grains are used, but 114 AU for porous grains ($p = 0.9$, $q_{\rm ice} = 0.0$). This indicates that the thermal emission is probably produced by porous grains, in agreement with the modelling done by Li and Lunine (Li and Lunine 2003a).

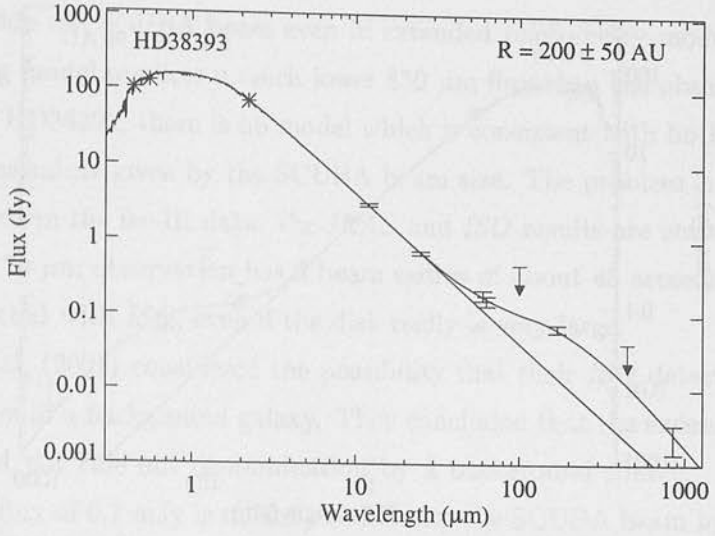


**Figure 3.18:** SED of HD38393 with model fit to the data. The *ISO* 60 $\mu$m point has been offset to the right to distinguish it from the *IRAS* 60 $\mu$m point. Upper limits are 3 sigma.

### 3.6.7 HD109085

HD109085 is clearly detected in the sub-mm, indicating that the *IRAS* association is real. However, no model can simultaneously fit all of the data (Figure 3.17). This indicates that there must be dust at a variety of distances from the star, as is the case for $\beta$ Pic and HD141569. For the fitted model, the *IRAS* 12 and 25 $\mu$m points have not been included, so the fitted radius reflects the size of the coolest parts of the disk, i.e. the disk's overall extent. This gives a result of 180 AU, which at a distance of 18.2 pc gives an angular radius of 9.9 arcsec. This is more extended than the SCUBA beam, so this flux estimate is probably smaller that the true flux by a factor of $\sim 2$ (Table 3.3). Given the size and brightness of the disk, it should be possible to fully map HD109085 with SCUBA, and such observations are currently being performed (Wyatt et al. in preparation).

### 3.6.8 HD38393

HD38393 is extremely faint in the sub-mm, and is only detected at the 2.4 sigma level. The modelling produces a good fit to the SED (Figure 3.18), but with a disk radius of $200 \pm 50$ AU for solid dust grains. At the distance of HD38393 (9.0 pc), this corresponds to a radius of 22 arcsec. This would place most of the flux outside the SCUBA beam (even though the extended photometry mode was used), implying that the true flux at 850 $\mu$m is much higher than the measured flux. In fact, if this radius is correct emission

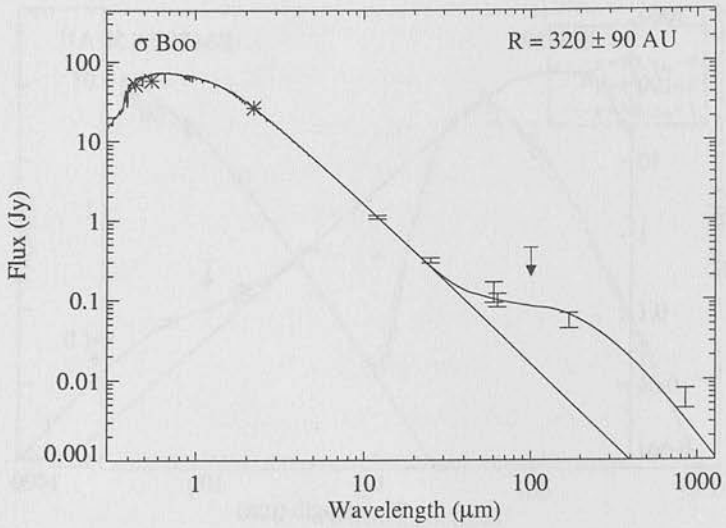


**Figure 3.19:** SED of $\sigma$ Boo. The *ISO* 60 $\mu$m point has been offset to the right to distinguish it from the *IRAS* 60 $\mu$m point. Upper limits are 3 sigma.

would only be detected if the source is edge on. Revising the estimate of the 850 $\mu$m flux results in a still larger fitted radius (because a higher sub-mm flux indicates a cooler disk), and so does not resolve this problem. Nor does choosing a different dust composition, as porous grains tend to be warmer than solid grains, and so also increase the estimated disk size.

Given the low significance of the detection, it is possible that the 850 $\mu$m detection is either spurious, or caused by a background galaxy. The source counts of galaxies detected in blank fields (e.g. Figure 11 in Scott et al. 2002) show that there is a 6 per cent probability that a 2.4 mJy background source will fall into the beam of SCUBA in extended photometry mode (which is sensitive over a 300 arcsec$^2$ area). Habing et al. (2001) also concluded that their 170 $\mu$m detection is likely to be due to a background galaxy, given the low flux and the galaxy number counts at that wavelength. However, an alternative explanation is that the estimate of the disk size is wrong: the difficulty fitting the SED of $\epsilon$ Eri may indicate that the model is generally unreliable for cool stars, and hence the true size of the disk could be smaller than 200 AU. This would mean that the disk is deficient in small grains compared with our model.

### 3.6.9 $\sigma$ Boo

Excess sub-mm emission from $\sigma$ Boo was detected at the 3.6 sigma level, with a flux of 6.7 mJy. However, the best fitting model gives a disk radius of $320 \pm 90$ AU, which corresponds to an angular radius of 20 arcsec, implying that most of the 850 $\mu$m flux

would be outside the SCUBA beam even in extended photometry mode. In addition, the best fitting model predicts a much lower 850 $\mu$m flux than the observed value. As is the case for HD38393, there is no model which is consistent with both the SED and the spatial constraints given by the SCUBA beam size. The problem is unlikely to be caused by errors in the far-IR data: the *IRAS* and *ISO* results are entirely consistent, and the *ISO* 170 $\mu$m observation has a beam radius of about 45 arcsec, so all the flux would be detected with *ISO*, even if the disk really is very large.

Habing et al. (2001) considered the possibility that their *ISO* detection at 60 and 170 $\mu$m was due to a background galaxy. They concluded that the excess was probably real, but could not rule out contamination by a background source. A background galaxy with a flux of 6.7 mJy is unlikely to fall into the SCUBA beam by chance alone (1 per cent probability), but as $\sigma$ Boo was selected on the basis of a far-IR excess, contamination by a background source becomes more likely. The alternative explanation is that $\sigma$ Boo is deficient in small grains, which would reconcile the modelling results with the SCUBA beam size.

### 3.6.10 HD48682

HD48682 is a quoted as visual binary in the Washington double star catalogue with a separation of 34 arcsec. However the two stars cannot be physically associated due to their differing proper motions, and it appears that HD48682B is in fact a background object. Given that the separation of the two components is similar to the *IRAS* beam size, it is not obvious whether the photosphere of the secondary will contribute to the *IRAS* fluxes or not. The *IRAS* beam is different at each wavelength, as the diffraction limit is much smaller at 12 $\mu$m than it is at 100 $\mu$m. This means that the secondary photosphere may only contribute to the measured fluxes at longer wavelengths. In addition, it is very difficult to estimate the brightness of the secondary at *IRAS* wavelengths, because the star is most likely an M star and only optical photometry is available. A small uncertainty in the effective temperature therefore causes a large error in the estimated mid-IR flux. A K band image would resolve this problem, but unfortunately the secondary star is saturated on 2MASS images, so a dedicated observation would be required. Aumann and Probst (1991) made ground based observations of HD48682 at 10 $\mu$m, and concluded that the 12 $\mu$m excess comes from $> 6$ arcsec from the primary and is consistent with the flux from the secondary, but that the secondary photosphere cannot account for the large 60 $\mu$m excess. The detection with SCUBA confirms that the 60 $\mu$m *IRAS* excess is associated with the primary and not the secondary, but the

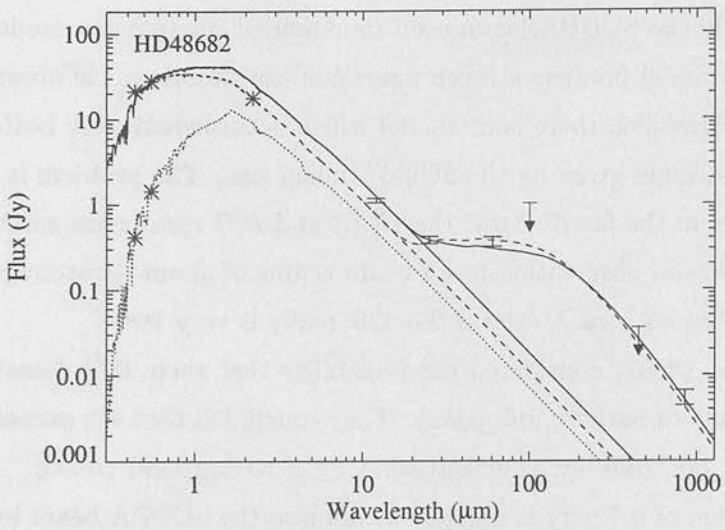


**Figure 3.20:** SED of HD48682, with model fit to the data. Asterisks show optical and near-IR photometry, *IRAS* and SCUBA data are shown with error bars. The photospheric flux from the primary, and the best fit model assuming that only the primary contributes to the *IRAS* fluxes are shown with dashed lines. The secondary is shown with a dotted line. Solid lines show the combined photospheric flux, and combined photospheric flux plus best fit model assuming that the secondary does contribute to the *IRAS* fluxes. Upper limits are $3\sigma$.

source of the 12 and 25 $\mu$m excess is not clear.

Figure 3.20 shows the SED of HD48682, and the best fit model. The modelling has been done in two ways, with and without the secondary included in the photosphere subtraction (assuming a spectral type M0). At 12 $\mu$m, the IRAS flux is more than the photosphere of the primary, which could either be due to circumprimary emission at $> 6$ arcsec, or flux from the secondary. At 25 $\mu$m, the *IRAS* flux is more than the combined flux from primary and secondary, indicating that there is definitely emission by dust at this wavelength. There is a large excess at 60 $\mu$m, and the secondary photosphere could only make a small contribution even if it is within the beam. The modelling results are better if the secondary is included in the photosphere subtraction (reduced $\chi^2 = 3.1$, verses 7.0 if the secondary is not included). If the secondary is not included in the subtraction, the estimated radius is $71 \pm 15$ AU, whereas if the secondary is included, the estimated radius is $110 \pm 21$ AU. If the larger value is true, the projected radius would be 6.7 arcsec, so the disk could be marginally resolved with SCUBA mapping. The shape of the fitted model indicates that there would be only a small excess at 18 $\mu$m, so resolved ground based mid-IR imaging would be difficult.

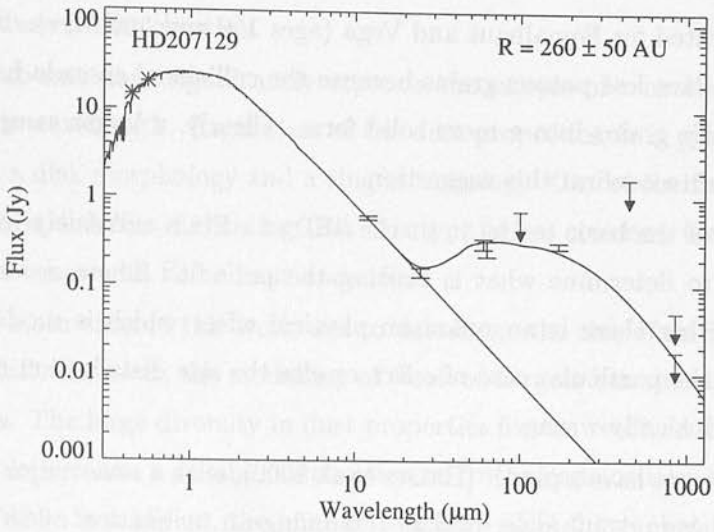


**Figure 3.21:** SED of HD207129. The *ISO* 60 $\mu$m point has been offset to the right to distinguish it from the *IRAS* 60 $\mu$m point. Upper limits are 3 sigma. The lower data point at 850 $\mu$m is the result if the source is unresolved, the upper point is the result if the source is resolved but with a radius smaller than 20 arcsec.

### 3.6.11 HD207129

HD207129 is not detected in the archived SCUBA measurements, but because there are *ISO* measurements at 170 $\mu$m a model fit is possible, and the SCUBA upper limit also helps to constrain this fit. The SED and model fit are shown in Figure 3.21. The fitted size of the disk is $260 \pm 50$ AU, which corresponds to an angular radius of 17 arcsec. Since this is larger than the SCUBA beam a significant fraction of the flux would not have bean detected, and the quoted upper limit on the 850 $\mu$m flux may actually be lower than the true flux. HD207129 was observed in both photometry mode and map mode, and the quoted upper limit of $< 0.018$ Jy is based on both sets of measurements. If just the mapping data are used, then an integrated flux over a 20 arcsec radius aperture can be calculated. This method gives a flux $< 0.05$ Jy (3 sigma).

## 3.7 Discussion

The most striking result of this modelling is that there is a large diversity in dust grain compositions between different disks. A simple explanation for this result is that dust grain composition may vary with age. The modelling of HD141569 and HR4796 (age 5 and 8 Myr respectively) indicates high porosity grains ($p = 0.9$), as does the previous modelling of $\beta$ Pic (age 20 Myr) done by Li and Greenberg (1998). However, solid

grains are indicated for Fomalhaut and Vega (ages 150 and 350 Myr). It may be that the older stars have less porous grains because the collisional cascade has reprocessed the initially fluffy grains into a more solid form. Clearly, a larger sample of resolved disks is required to confirm this suggestion.

The failure of the basic model to fit the SED of $\epsilon$ Eri is extremely interesting, and it's important to determine what is causing the poor fit. There are essentially two possibilities: either there is an unknown physical effect which is modifying the size distribution in the particular case of $\epsilon$ Eri, or else the size distribution model we have assumed is intrinsically wrong.

$\epsilon$ Eri is known to have a planet (Hatzes et al. 2000), with a semi-major axis of 3.4 AU and a mass of around 2 Jupiter masses (assuming an inclination of 25° as measured by Greaves et al. 1998). This planet is unlikely to affect the dust size distribution at 60 AU, because of its small orbital radius. However, a planet with a large semi-major axis has been inferred from the existence of clumps within the dust disk (Quillen and Thorndike 2002). If this planet is real, then dynamical effects are clearly very important in shaping the disk, and this would undoubtedly affect the size distribution of the dust.

The alternative explanation is that the discrepancy is not due to an external influence, but that a more accurate treatment of the dust grain size distribution in a collisional cascade is needed to account for the SED. More detailed size distribution models allow the grain strength to vary with grain size, and account for the effects of removing small grains on the overall size distribution (Campo Bagatin et al. 1994; Durda and Dermott 1997). For $\beta$ Pic, extensive numerical models of this type have been produced, both for the inner disk (Thébault et al. 2003) and for the outer disk (Krivov et al. 2000). Both of these studies show significant deviation from the theoretical size distribution used in this chapter. This suggests that a more rigorous treatment of the collisional cascade in $\epsilon$ Eri would also give a significantly different size distribution. However, it is not obvious that this would produce a better fit to the SED (i.e. that the new size distribution would have few grains smaller than 3 $\mu$m). In fact, according to Campo Bagatin et al. (1994) an enhancement of grains just above the blowout radius should be expected as they are less likely to be destroyed by collisions, which would make the problem worse. Conversely, the modelling of $\beta$ Pic's outer disk by Krivov et al. (2000) suggests a reduction in the number of grains just above the blowout limit, because they are destroyed by small, fast moving grains as they are ejected from the system by radiation pressure. However, as the stellar luminosity is much lower for $\epsilon$ Eri, this mechanism is likely to be less important. Only detailed modelling specific to $\epsilon$ Eri's

dust disk can answer this question.

The new sub-mm data significantly expands the sample of true Vega excess stars detected at this wavelength. Regardless of the dust properties, it is possible to distinguish between a disk morphology and a ring morphology. Out of the five new objects, only HD109085 is disk like, indicating that this type is less common than the ring like structure observed around Fomalhaut and $\epsilon$ Eri.

One of the main aims of this work was to determine the size of an unresolved disk from just its SED. However, the modelling of resolved targets has shown that this may not be possible. The large diversity in dust properties for the resolved disks mean that it is not possible to make a reliable assumption as to the composition of the grains in an unresolved disk. In addition, the poor fit to $\epsilon$ Eri's SED shows that the model may not in general contain all of the physics necessary to account for the observations. The estimates of the disk size are based on the assumption that the dust grains are solid (as for Fomalhaut), but if the grain properties are different, then the size estimates will be incorrect.

Future progress in this field depends on spatially resolving disks, as this allows a direct measure of disk size and thus measurements of the dust composition. These results indicate that there are probably a few more targets that can be resolved using SCUBA, given sufficient integration time. Also, ground based mid-IR observations also have the ability to resolve some disks. However, large numbers of resolved disks may have to wait until SIRTF and SOFIA become available.

## 3.8 Conclusion

I have presented new observations and modelling of Vega excess disks with sub-mm data. These observations expand the sample of Vega excess stars detected in the sub-mm from 5 to 10, with a further 4 objects which were not detected but have useful upper limits. I have fitted the observed SEDs with models based on realistic dust grain composition and size distribution. Dust grain composition varies significantly between different objects, with younger disks having more porous grains. For $\epsilon$ Eri, the models fails to fit the data unless there are less small grains in the system than expected from a collisional cascade. This discrepancy may be due to an inadequacy in the model of the size distribution, or the result of an external influence such as a planet. For the unresolved targets, disk size is estimated assuming solid dust grains, but given the observed diversity in dust composition and the problems fitting $\epsilon$ Eri, these size

estimates may not be reliable.

# Chapter 4

# Mid-IR imaging of debris disks

## 4.1 Introduction

In investigations of debris disks, one of the key aims is to understand Vega excess disks in the wider context of star and planet formation. In order to achieve this aim, it is essential to study objects at a variety of different evolutionary stages. Different observing strategies are required for different types of object, and many different techniques are needed to give a true picture of what is happening at different times.

The progenitors of Vega excess disks are T-Tauri and Herbig Ae/Be stars. These stars have optically thick disks with material from 0–200 AU, and contain much more gas than dust. Almost all pre-main sequence stars have such a disk, but by the time a star reaches the main sequence much of the dust and nearly all of the gas has disappeared, leaving a Vega excess star with an optically thin disk, and a cleared region <30 AU from the star (Backman and Paresce 1993). Though Vega-type disks evolve from T-Tauri and Herbig Ae/Be disks, the observational evidence from older disks indicates that they are fundamentally different from the young counterparts. Vega excess disks contain solid material in large bodies. This naturally implies that the disk must have undergone a phase of planetesimal building, where small dust grains accreted together to form larger bodies. However, the existence of small grains in old disks shows that Vega disks are now grinding down the large planetesimals to smaller ones in a collisional cascade. Disks therefore must pass from a constructive phase in their early life into a destructive phase latter on. The root of this change lies in the collisional ve-

locity between dust grains. In young disks, the collisional velocities between grains are held low by gas drag, leading to constructive collisions. However, once the gas is gone, there is nothing to stop collisional velocities increasing to the point where the disk will enter a destructive phase. This picture leaves open the question of what actually drives the increases in collisional velocity, but if there are very large bodies in the disk, then gravitational stirring could provide the necessary perturbation (Kenyon and Bromley 2001).

Clearly, understanding the transition between the two types of disk is of key importance to understanding planet formation processes and how Vega-type disks formed. Several questions need to be answered. When do disks enter the debris disk phase, i.e. when do collisions become destructive, and is this really caused by the formation of planets within the disk? How is the inner disk (0–30 AU) cleared, and on what time-scale? Is the inner disk cleared by the formation of planets and does this occur before or after the start of the collisional destruction of the outer disk?

The obvious way to address these questions is to observe disks in transition between the T-Tauri/Herbig Ae Be phase and the Vega excess phase. Such objects can be identified fairly easily, and several such disks have been studied. In particular $\beta$ Pic, the most studied of all debris disks, is probably best classified as a transitional object. Mid-IR observations are particularly useful for studying these transitional disks. Older debris disks with ages of around 100 Myr tend to emit little radiation in the mid-IR, indicating that the inner parts of the disk have been cleared. However, transitional disks with ages of around 10 Myr still have an inner disk which emits in the mid-IR. In addition there is a significant number of objects which are close enough to be resolved using a 4 or 8 meter class telescopes.

This chapter describes mid-IR imaging of debris disks using MICHELLE on the United Kingdom Infrared Telescope (UKIRT). The work in this chapter comes from a programme to directly resolve the disks around several nearby main sequence stars. The implementation of this program has been hampered by poor weather and delays in the mid-IR instrumentation for Gemini South, but the data obtained so far are presented here.

## 4.2 Selection criteria

The aim of this program was to resolve transitional disks around young main sequence stars. The criteria were therefore that the systems should be at the correct evolution-

ary stage, have significant emission at 20 $\mu$m (the longest wavelength observable with MICHELLE), and be large enough to be resolved with UKIRT.

To identify suitable targets, a database of main sequence stars with an IRAS excess was used (available at `http://www.roe.ac.uk/atc/research/ddd/`). This database is formed from several surveys of the IRAS catalogue (e.g. Mannings and Barlow 1998; Walker and Wolstencroft 1988). For each star in the database the photospheric flux at 12 and 25 $\mu$m was calculated using a Kurucz model atmosphere normalised to the K band magnitude. By using K band to normalise the model atmosphere, the effects of reddening and also stellar metallicity are greatly reduced. Unfortunately, it was not possible to obtain K band magnitudes for all stars in the database, and stars without K band data were not considered further. Of the original 270 Vega excess stars with a measured 12 or 25 $\mu$m flux in the database, only 180 had known K band magnitudes.

The spectral type of each star, taken from the Michigan Spectral Catalogue, was used to choose the best model atmosphere in each case. The photospheric flux was then colour corrected for the IRAS pass-bands (as described in Section 3.5.6), and stars were selected that had an excess at both 12 and 25 $\mu$m, and an $F_\nu$ excess which is rising between 12 and 25 $\mu$m. The rising flux criteria ensures that the emission at 20 $\mu$m comes from an extended disk, not from the Rayleigh-Jeans tail of a very small disk.

To ensure the stars were at the correct evolutionary stage, the fractional excess of the disks ($f_{\rm IR} = L_{\rm disk}/L_{\rm star}$) was calculated by integrating the excess flux measured by IRAS. For pre-main sequence stars, $f_{\rm IR}$ is around 0.2 as the disk is optically thick, though the actual value of $f_{\rm IR}$ will depend on the opening angle of the disk. For Vega excess disks, $f_{\rm IR}$ is typically around $10^{-4}$, as the disks are optically thin. In this sample, only objects with $f_{\rm IR} < 0.01$ were allowed, excluding young optically thick disks. The requirement for a 12 $\mu$m excess excludes the older Vega excess stars, leaving just the transitional objects.

Finally, the disks must be large enough to be resolved, so that a measurement of the disk size can be made. The size of the disks in this survey is not known, but an estimate can be made from other similar objects. Only three objects have been resolved in the mid-IR ($\beta$ Pic, HR4796 and HD141569); all three met the criteria to be included in the sample, and were only excluded because they had already been observed. These disks range from 65 to 100 AU in radius (see references cited in Section 1.5.2). The average radius is 85 AU, so this was taken as the estimated size for the disks in this survey. An alternative approach is to use the SED modelling system described in Chapter 3 to estimate the disk sizes, and the fitted SEDs of HD161868 and HD220825

| Object | Spectral type | Distance (pc) | Estimated size (arcsec) | $L_{Dust}/L_{Star}$ | $F_{12}$ (Jy) | | $F_{25}$ (Jy) | |
|---|---|---|---|---|---|---|---|---|
| | | | | | Dust | Star | Dust | Star |
| HD93331 | B9.5V | 151.5 | 1.2 | 0.0009 | 0.088 | 0.049 | 0.155 | 0.011 |
| HD139450 | G0/1V | 73.5 | 2.4 | 0.0109 | 0.503 | 0.045 | 0.746 | 0.010 |
| HD145263 | F0V | 116.3 | 1.5 | 0.0075 | 0.406 | 0.027 | 0.509 | 0.006 |
| HD145482 | B2V | 143.5 | 1.2 | 0.0001 | 0.296 | 0.364 | 1.458 | 0.082 |
| HD155401 | B9V | 167.5 | 1.0 | 0.0014 | 0.300 | 0.127 | 1.081 | 0.029 |
| HD161868 | A0V | 29.1 | 6.0 | $7.5 \times 10^{-5}$ | 0.026 | 1.384 | 0.199 | 0.311 |
| HD176269 | B7/8V | 134.2 | 1.3 | 0.0005 | 0.349 | 0.089 | 0.635 | 0.020 |
| HD181296 | A0V | 47.7 | 3.7 | 0.0002 | 0.110 | 0.371 | 0.406 | 0.085 |
| HD220825 | A0V | 49.7 | 4.0 | 0.0001 | 0.090 | 0.405 | 0.140 | 0.091 |

**Table 4.1:** Sample for the program. $F_{12}$ and $F_{25}$ refer specifically to the IRAS excess. HD161868 does not have a significant IRAS 12 $\mu$m excess, but was included because ground based photometry indicates that an excess may be present (Fajardo-Acosta et al. 1998).

(the targets from the sample that have been observed to date) are shown in Figures 4.1 and 4.2. However, these fitted disk sizes may be somewhat misleading. The fitted size for HD220825 small partly because this source only as an upper limit as 60 $\mu$m. The absence of a detection at 60 $\mu$m allows a small fitted radius, but the true size could be much bigger. In addition, these fits assume that the dust grains have a solid composition. If the real grains are porous, the radius could be larger by a factor of two. The angular size of each disk was therefore estimated using an assumed radius of 85 AU and the Hipparcos parallax of the star. This was then used to rank the selected objects from easiest to hardest to resolve. The complete list of selected targets is shown in Table 4.1.

## 4.3 Observations

### 4.3.1 Observation details

The observations were made using MICHELLE (Glasse et al. 1997), the mid-IR imager spectrometer on the United Kingdom Infrared Telescope (UKIRT). MICHELLE uses a 320x240-pixel array which operates between 8 and 25 $\mu$m. In imaging mode on UKIRT, the pixel scale is 0.21 arcsec pixel$^{-1}$.

HD161868 was observed at 11.6 $\mu$m on May 1 2002, and HD220825 was observed at 11.6 and 18.5 $\mu$m on August 31 2002. The weather was poor on both nights. The first run was hampered by intermittent cloud, which made 18.5 $\mu$m observations impossible, and also made the atmospheric extinction extremely variable. Conditions on the second

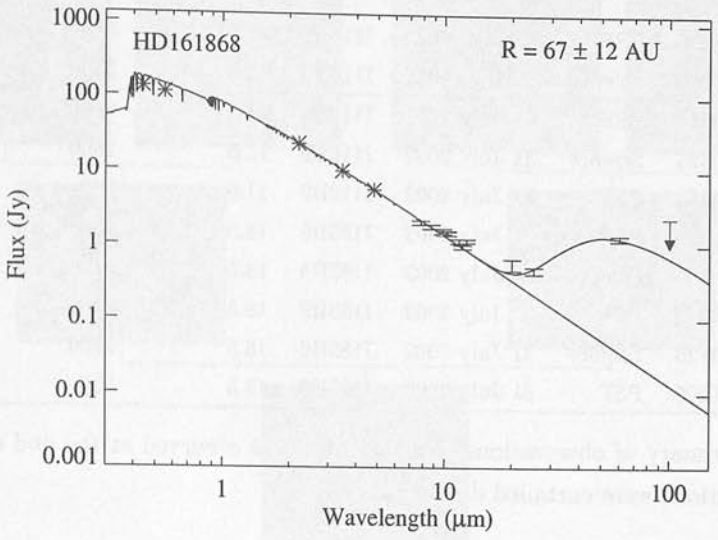


**Figure 4.1:** SED of HD161868 and model fit to the data with ring radius as a free parameter. Colour corrections for the *IRAS* data as plotted here were estimated from the model. The data plotted are taken from the IRAS faint source catalogue and Fajardo-Acosta et al. (1998). At 12 $\mu$m there is some discrepancy between the two; the IRAS flux indicates no excess whereas the ground based photometry shows an excess.

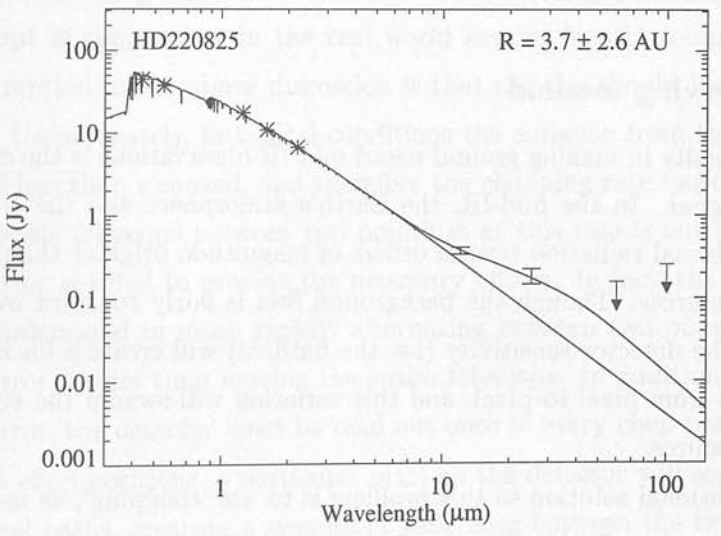


**Figure 4.2:** SED of HD220825 and model fit to the data with ring radius as a free parameter. Colour corrections for the *IRAS* data as plotted here were estimated from the model.

| Object | Type | Date | Filter | Wavelength $\mu$m | Integration time seconds |
|---|---|---|---|---|---|
| HD157236 | PSF | 1 May 2002 | I116B9 | 11.6 | 800 |
| HD161868 | Science | 1 May 2002 | I116B9 | 11.6 | 5400 |
| HD220954 | PSF | 31 July 2002 | I116B9 | 11.6 | 1000 |
| HD220825 | Science | 31 July 2002 | I116B9 | 11.6 | 1800 |
| HD220954 | PSF | 31 July 2002 | I116B9 | 11.6 | 700 |
| HD6860 | PSF | 31 July 2002 | I185B9 | 18.5 | 550 |
| HD220825 | Science | 31 July 2002 | I185B9 | 18.5 | 2700 |
| HD6860 | PSF | 31 July 2002 | I185B9 | 18.5 | 350 |
| HD220825 | Science | 31 July 2002 | I185B9 | 18.5 | 2700 |
| HD217906 | PSF | 31 July 2002 | I185B9 | 18.5 | 350 |

**Table 4.2:** Summary of observations. No PSF star was observed at the end of the May run because observations were curtailed due to bad weather.

run were much more stable, but atmospheric water vapour led to very high extinction in the mid-IR, particularly at 18.5 $\mu$m. The 11.6 $\mu$m and 18.5 $\mu$m filters both have fairly narrow bandpass (approximately 11.1–12.1 for the 11.6 $\mu$m filter and 17.7–19.3 for the 18.5 $\mu$m filter), which meant that they were most appropriate for the poor weather conditions, as they prevent the array from saturating due to the sky emission. In addition to the two science targets, standard stars were also observed to accurately determine the PSF. The PSF stars were chosen to be close to the science target and bright in the mid-IR. Full details of all the observations are given in Table 4.2.

### 4.3.2 Observing method

The main difficulty in making ground based mid-IR observations is the extremely high background signal. In the mid-IR, the Earth's atmosphere and the warm telescope optics emit thermal radiation several orders of magnitude brighter than the flux from astronomical sources. Though the background flux is fairly constant over the image, variations in the detector sensitivity (i.e. the flatfield) will create a background signal which changes from pixel to pixel, and this variation will swamp the signal from any astronomical source.

The conventional solution to this problem is to use 'chopping', as used in the sub-mm observations described in Chapter 3. In the mid-IR, the basic technique is to take images with two slightly different pointings, and then examine the difference between these images. So long as the sky emission is similar in the two images, the background signal will cancel out; because the flatfield correction is the same in each case, this

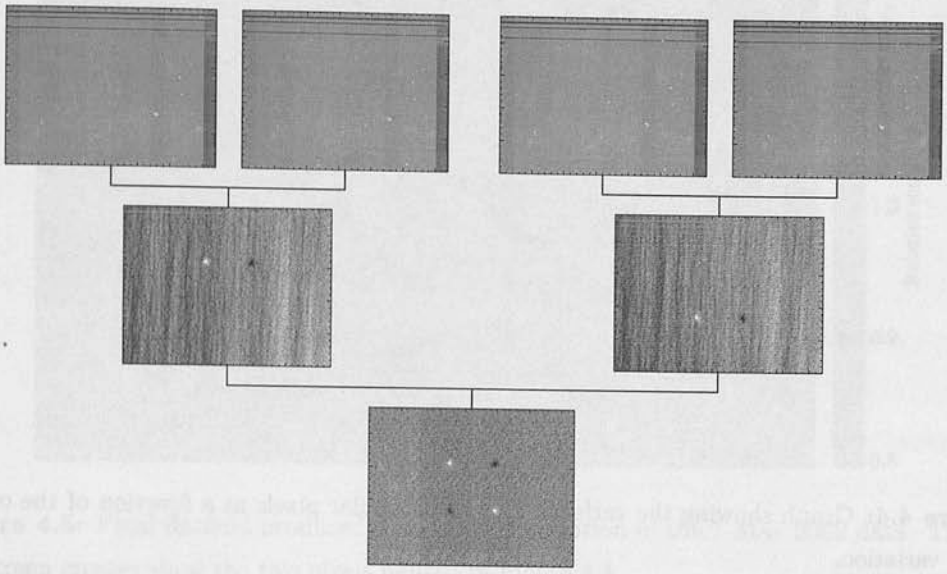

**Figure 4.3:** Diagram showing how chopping and nodding are used to remove the sky signal from the data. In the first stage, the data from the two chop positions are subtracted. Then data from two different nod positions are combined to give the final frame.

subtraction will be near perfect. As the source is in a different position on each image, it will not cancel out, and a positive and negative version of the source will be left over.

The concept is simple, but in the real world several factors complicate matters. The key assumption in the above discussion is that the sky should look the same on both images. Unfortunately, in typical conditions the emission from the sky varies on a timescale of less than a second, and therefore the chopping rate must be several Hz. Moving the whole telescope between two pointings at this rate is not possible, so the secondary mirror is tilted to provide the necessary offsets. In fact, the term chopping is generally understood to mean rapidly alternating between two pointings using the secondary mirror, rather than moving the entire telescope. In addition to moving the secondary mirror, the detector must be read out once in every chop position.

In the two chop positions, a particular pixel on the detector will see the sky along differing optical paths, creating a systematic difference between the two images. The residual sky signal created by this difference is removed by 'nodding' the telescope. This means moving the entire telescope to a slightly different pointing, making another set of chopped observations, and subtracting this from the first set. As this is an

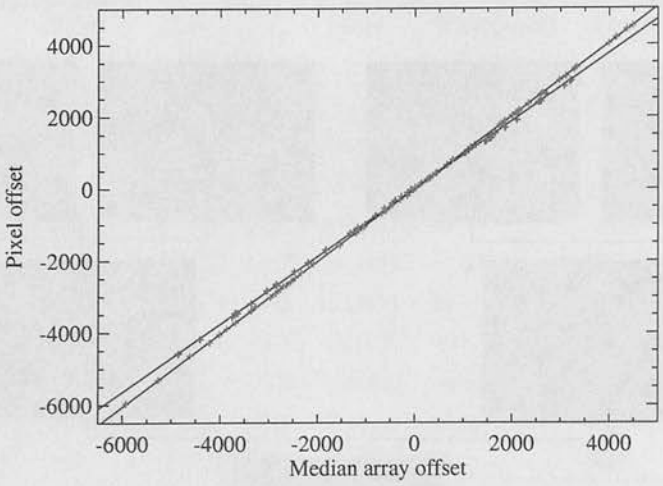


**Figure 4.4:** Graph showing the variation of two particular pixels as a function of the overall array variation.

optical effect, it will change only slowly, and so it is sufficient to nod every minute or so. Usually, the nod direction is perpendicular to the chop direction, so that the source will remain somewhere on the detector at all times. In these observations the nod and chop throw were both 15 arcsec. An example of the chop and nod process is shown in Figure 4.3.

## 4.4 Data reduction

### 4.4.1 Flatfielding mid-IR arrays

Flatfielding ground based mid-IR detectors is a difficult problem, and often this step is neglected when reducing mid-IR observations. However, because this dataset has high signal to noise, errors due to the flatfield could be the dominant source of uncertainty in the final images, and it is vital that a flatfield correction is made.

An accurate flatfield is important for two reasons. Firstly, though chopping and nodding remove most of the background signal, the variability of the sky means that some residual sky emission will remain. This residual emission can be removed by measuring the signal in regions of the detector which are far from any source, but this will only be valid for all parts of the detector if the flatfield is known. Secondly, the final image should hopefully contain an astronomical source, and the flatfield correction needs to be applied to this.

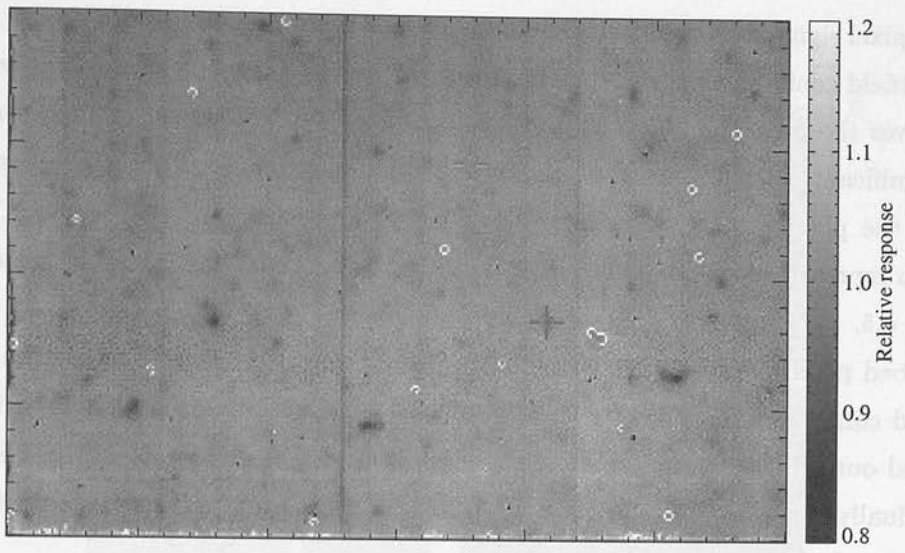


**Figure 4.5:** Final flatfield produced from the sky variation in the 1 May 2002 data. The red and green crosses show the two pixels plotted in Figure 4.4.

Mid-IR flatfielding is difficult for several reasons. Firstly, the dark current and flatfield are not stable (unlike optical and near-IR detectors), and in fact can vary significantly on a timescale of hours. This means that flatfield observations must be taken very frequently. Secondly, the flatfield depends on the exact readout mode of the detector, so the exposure time must be the same for the flatfield source and the science observations. This means that the flatfield source must have a similar brightness to the sky, or else the detector will saturate. Thirdly, the flatfield source must pass through the same optical path that the sky does. This is because the flatfield depends on components which are not in the focal plane (such as the instrument window).

The approach taken here is to use the natural variation in sky brightness over the course of the science observations to flatfield the array.[1] This method has the advantage that the flatfield observations are taken at exactly the same time as the science observations, and at the same brightness. The method only works if there are significant variations in the sky level over the course of the observations, but as the data were taken in moderately poor weather, this criterion is satisfied.

The method was implemented as follows. After masking off dead parts of the detector, the median signal was calculated for each integration. This gives the median sky signal plus the median dark current. Then for each pixel, a straight line was fitted

[1] Further details of this method can be found on these web pages:
`http://cfa-www.harvard.edu/~jhora/mirac/mrcffield.html`
`http://www.ls.eso.org/lasilla/Telescopes/360cat/timmi/T2_Flats/timmi_flat.html`

to the pixel signal as a function of median detector signal. The slope of this line is then the flatfield coefficient for that pixel. The errors on the line slope were calculated, and this gives the uncertainty in the flatfield for each pixel. Integrations where the pixel (or significant parts of the detector) were saturated were ignored. Any integrations where the pixel may have picked up flux from a source were also ignored. The fit for two representative pixels is shown in Figure 4.4, and the final flatfield is shown in Figure 4.5.

A bad pixel mask was then created by identifying pixels with a very high or low flatfield correction, and pixels with high flatfield uncertainty. Also, pixels which had a signal outside the linear region of the detector were flagged as bad; this was done individually for each nod-pair, as the number of pixels affected depends on the sky emission, which changes with time.

### 4.4.2 Method

Once the flatfield had been created (using observations over the whole night), each object was reduced individually. Firstly, the four frames from each chop/nod set were subtracted, giving a set of frames with most of the sky signal removed. The residual background signal was then subtracted from these frames. Three distinct type of background signal were identified: residual sky emission, block offsets in 20 pixel wide columns, and a ripple effect. The block offsets are produced by the readout electronics (the detector is read out in 20 pixel wide blocks), the ripple effect may be produced by RF pickup. Only some of the frames are affected by block and ripple effects, and frames near the start of an observation or shortly after the array has been saturated are particularly susceptible. The block offset and ripple effects are produced in the electronics, so they must be removed before the flatfield correction is applied. The residual sky subtraction must of course be removed after flatfielding. The background subtraction procedure was therefore as follows. Firstly, the ripple was removed by subtracting the median level from each row. Then the block offset was removed by subtracting the median level from each 20 pixel wide block. These steps will have also removed the residual sky emission, which must be left on until the flatfield has been applied, so the sky emission was reinstated by adding on the median level from the original image. The image was then flatfielded, and the sky signal removed by subtracting the median level from the whole frame. The entire background subtraction process is shown in Figure 4.6.

To estimate the noise on each pixel, the chop/nod subtraction was done again, but

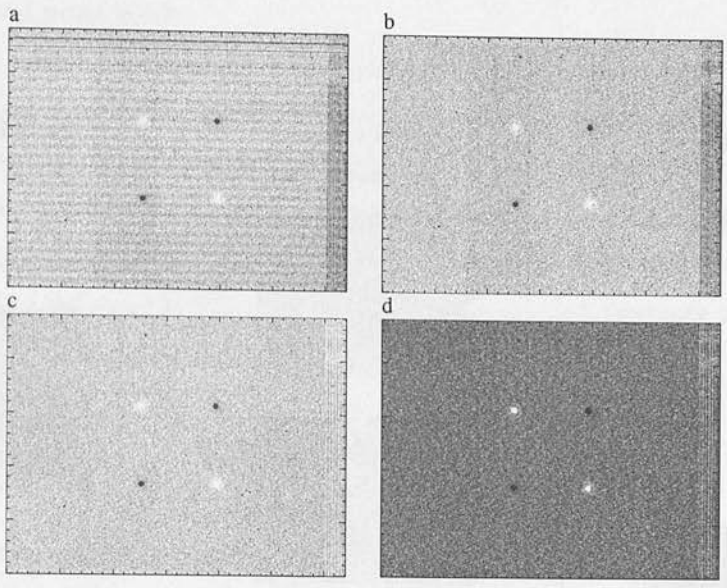


**Figure 4.6:** Background subtraction method. (a) The original image. (b) Ripples removed. (c) Block offsets removed. (d) Flatfielded and with the residual sky signal subtracted.

this time using sets of frames taken in the *same* nod position (Figure 4.7). This means that one half of the frame (either the top or the bottom) should be free of sources, and so can be used to measure the noise. The noise estimate was made by taking the standard deviation of each pixel through the set of frames. This method assumes that the noise will be constant throughout the observation, which is not strictly true as the sky emission changes. In these observations, the sky emission varied by a maximum of 20%, so poisson noise from the sky would vary by 10%. However, the method will produce a good estimate of the average noise during the observations, and in particular will identify all the noisy pixels.

Because the sky transparency varies with time, the source brightness will change on each image, and in each nod position. To correct for the varying sky transmission, a Gaussian was fitted to the sources in each image, and each sub-image was normalised to have the same integrated source flux. The error estimates for each sub-image were also scaled by the same factor. For HD220825, the source was not bright enough to be fitted on each frame, so this step had to be omitted. The images were then combined by calculating the weighted mean and error of each pixel over all the integrations. The pixel noise and the flatfield uncertainty were combined in quadrature to obtain the final

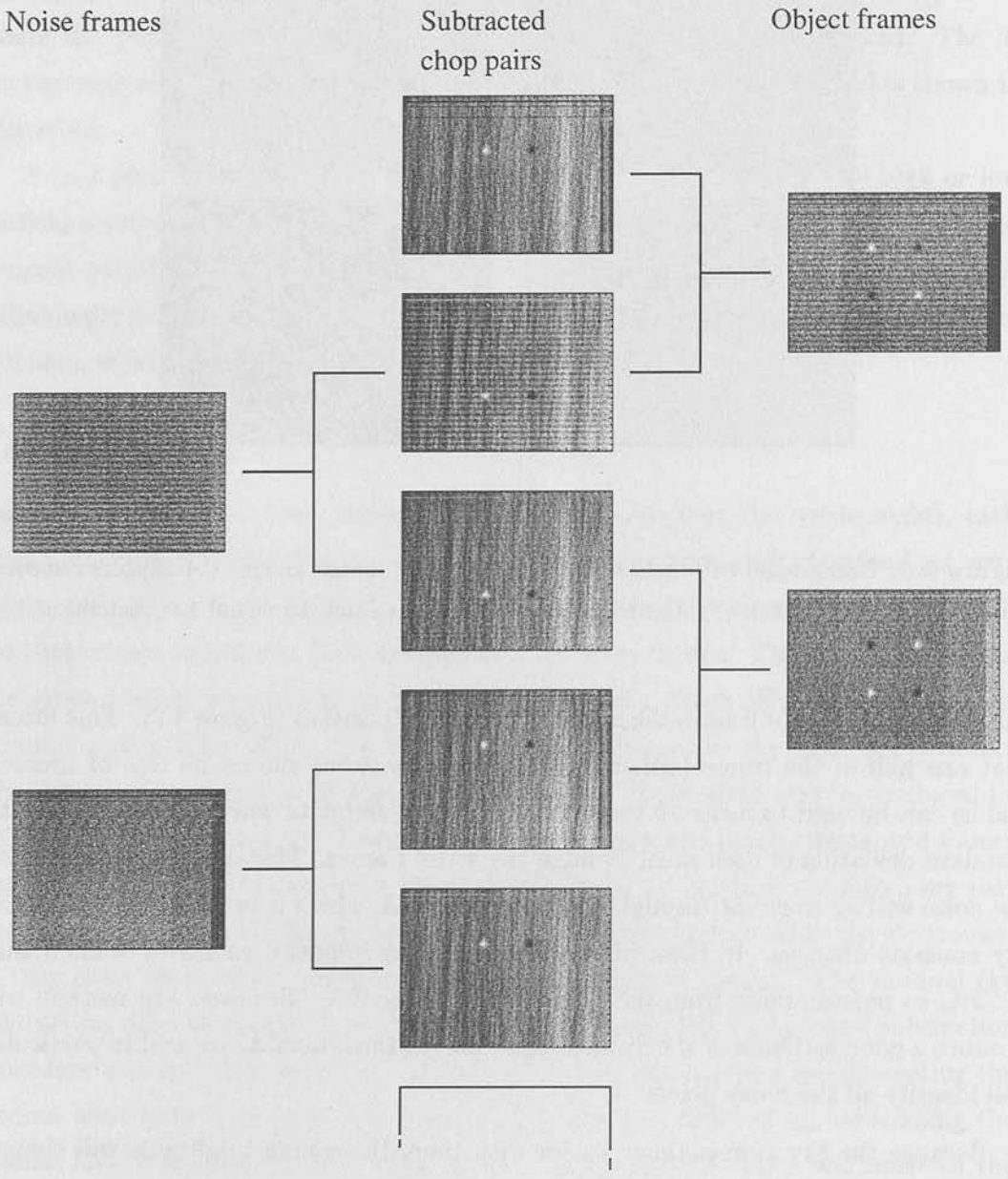


**Figure 4.7:** Subtraction scheme used to obtain the noise estimates. On the left, frames in the same nod position are subtracted, allowing an estimate of the noise on each pixel. On the right is the normal subtraction, which is used to produce the final images.

uncertainty on each pixel. Pixels which have no or few good datapoints were set to bad in the final bad pixel mask.

The final reduced data has four versions of the source, with uncertainties in each pixel, and a bad pixel mask. However, in each sub-image the source will have a different sub-pixel centring. This means that there is no simple way to combine the images without losing spatial information. Complicated schemes like drizzling (Fruchter and Hook 2002) are not feasible because there are only four pointings, and the sub-pixel grid is not sampled evenly. Therefore, each sub-image is left separate and analysed in parallel, which produces no loss of spatial information at all.

## 4.5 Analysis

The overall aim of the analysis is to determine the size of a circumstellar disk, or an upper limit to this size. The size of the smallest detectable disk depends on the signal-to-noise ratio of the data, and also on the stability of the point spread function (PSF) during the observations. The PSF is the image produced when a point source is observed, and this depends primarily on diffraction by the telescope optics and atmospheric seeing. Both of these factors can change with time, because of flexure in the telescope and atmospheric variations, and if the disk size is similar to the typical variation in the PSF, then the extension cannot be detected reliably.

An additional problem arises because the PSF is wavelength dependent. If a broadband filter is used, then light with a range of wavelengths will be detected. The diffraction pattern will therefore depend on the colour of the object that is being observed — blue objects will have smaller diffraction patterns than red objects. In addition, the seeing as also likely to be wavelength dependent. The significance of these effects will depend on the bandwidth of the filter.

Though the PSF is a continuous 2D function, the resulting image is only sampled at discrete intervals. The exact location of the image on the detector will change between observations, which means that a direct comparison of a science target and a PSF star is not possible. Therefore, the PSF star observations are used to create a model of the PSF. This model recreates the diffraction and seeing effects that determine the observed PSF, but has free parameters (e.g. seeing FWHM) which are constrained by fitting to the PSF star observations. The model can then be fitted to the science observations, with the source position and brightness as free parameters. As the uncertainties on the image pixels are known, any difference between the model and the observed image can

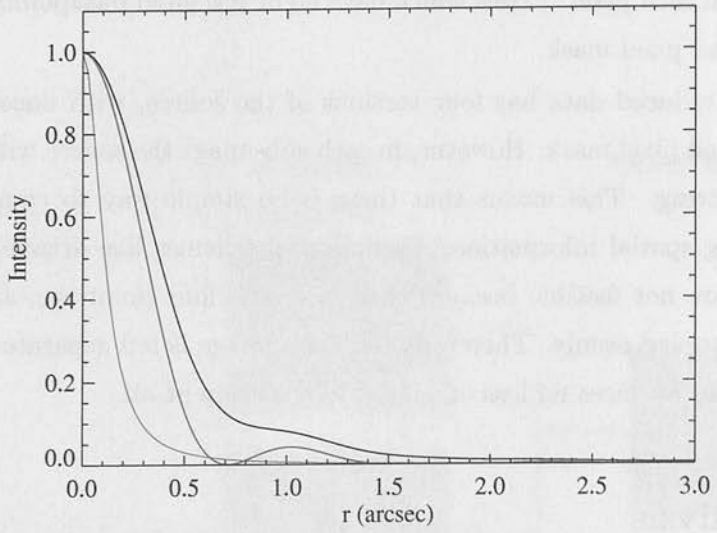


**Figure 4.8:** Radial plot of the model PSF, fitted to observations of a PSF star. The red line indicates the diffraction pattern of the mirror, the green line shows the seeing profile, and the black line the final radial profile.

be assessed to determine if it is significant. If the best fitting model is inconsistent with the data, then a disk model can be added, and the parameters of this model deduced. If, however, the science observation is consistent with the model, then the disk has not been detected, and limits on the size of the disk can be determined.

### 4.5.1 PSF model

The aim of the model is to produce a theoretical PSF which matches as closely as possible the observed PSF. There are three basic components to this theoretical model. Firstly, diffraction from the primary mirror sets the minimum possible size of the PSF, and also determines the location and strength of any diffraction rings. Secondly, atmospheric seeing will broaden the PSF, as will any inaccuracies in the telescope tracking. Finally, the continuous PSF at the focal plane is sampled by the detector. Each of these components must be included to produce an accurate model.

The diffraction pattern of the primary mirror can be determined using a Fourier transform. The UKIRT mirror is taken as being an annulus with an inner radius $r_{\rm in} = 0.514$ meters and an outer radius of $r_{\rm out} = 1.901$ meters. As this is a radially symmetric shape, the diffraction pattern can be determined by taking a Hankel

transform (Birkinshaw 1994):

$$\tilde{f}(k) = \int_0^\infty dr\, r\, J_0(kr)\, f(r), \tag{4.1}$$

where $J_0$ is a Bessel function. Here, $f(r)$ is the aperture function of the telescope and $\tilde{f}(k)$ is the resulting PSF. The wavenumber $k$ is equal to $2\pi\theta/\lambda$, where $\theta$ is the angular offset from the centre (in radians) and $\lambda$ is the wavelength of the observation. In this case $f(r) = 1$ where $r_{\rm in} < r < r_{\rm out}$ and $f(r) = 0$ otherwise, so

$$\tilde{f}(k) = \int_{r_{\rm in}}^{r_{\rm out}} dr\, r\, J_0(kr). \tag{4.2}$$

The intensity of radiation at the focal plane is then given by

$$I_{\rm PSF}(k) = \tilde{f}(k)^2. \tag{4.3}$$

The seeing was approximated by a Moffat profile (Moffat 1969):

$$I_{\rm seeing}(\theta) = \frac{I_0}{(1 + (\theta/R)^2)^\beta}, \tag{4.4}$$

where $I_0$ is the peak intensity, and $R$ and $\beta$ are free parameters that depend on the quality of the seeing. The contributions of diffraction and seeing can then be combined by convolving the two functions. As these are both radially symmetric functions, this can again be done using a Hankel transform (Birkinshaw 1994). The convolution $c(r)$ of two radially symmetric functions $a(r)$ and $b(r)$ is given by:

$$c(r) = 2\pi \int_0^\infty dk\, k\, J_0(kr)\, \tilde{a}(k)\, \tilde{b}(k). \tag{4.5}$$

Applying this to the seeing and diffraction profiles will give the final PSF at the focal plane. This was done by taking the inverse transforms of Equation 4.3 and 4.4, and applying Equation 4.5 to get the final PSF. All the transforms were done numerically. The radial PSF is shown in Figure 4.8.

Once the 1D radial PSF has been determined, a 2D image must be produced which can be directly compared with observations. The final image will depend on the instrument's pixel scale and on the exact position of the source on the detector. Although the detector pixel scale is designed such that the image will be critically sampled, there will still be a significant variation in the intensity of the PSF over the area of a pixel. This means that the final pixel value should be a 2D integral over the area of the PSF that the pixel covers. To accomplish this, the 1D profile was used to produce a very high resolution image, with 8 times the resolution of the real detector. Then, this high resolution image was binned up to make the final image (Figure 4.9).

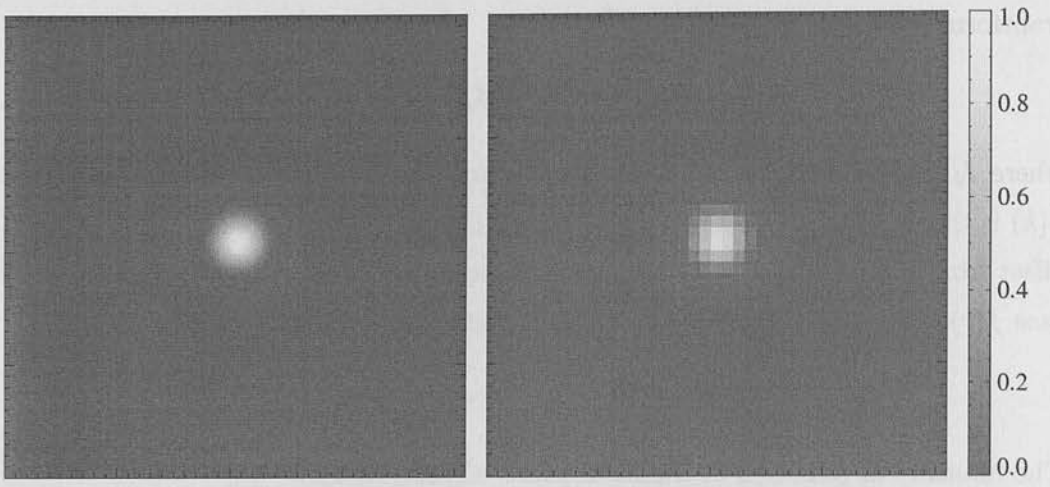


**Figure 4.9:** Model PSF in 2D. On the left is a high resolution version, produced directly from the radial PSF. On the right is the final version, produced by binning up the high-resolution image.

### 4.5.2 Determining the final PSF model

The free parameters in the PSF model are the seeing parameters ($R$ and $\beta$), the $x$ and $y$ position of the source and the total source flux. In addition, testing of MICHELLE on UKIRT indicated that the outer part of the primary mirror is somewhat vignetted, so the outer radius of the mirror $r_{\rm out}$ was also left as a free parameter. Only three of these parameters really define the PSF ($R$, $\beta$ and $r_{\rm out}$), as the source position and brightness will naturally change between observations. These three parameters were determined by fitting to the PSF observations. As there are four subimages due to nodding and chopping, each subimage has its own $x$, $y$ and flux parameter, but $R$, $\beta$ and $r_{\rm out}$ are forced to be the same for all subimages. Figure 4.10 shows the observed PSF, and the residuals after subtracting the best fitting model ($r_{\rm out} = 1.58$ meters, $R = 0.133$, $\beta = 1.805$). In this figure, the four subimages have been added together, but this does not cause any problems with degraded resolution as each subimages has been fitted and subtracted individually.

### 4.5.3 Fitting the science targets

Once the parameters of the PSF model have been determined, the model was fitted to the science targets. Again, each sub image must have its own $x$, $y$ and flux parameters, but the PSF parameters are held at the values determined from the standard star fits. The residuals between the observed images and the best fitting model can then be

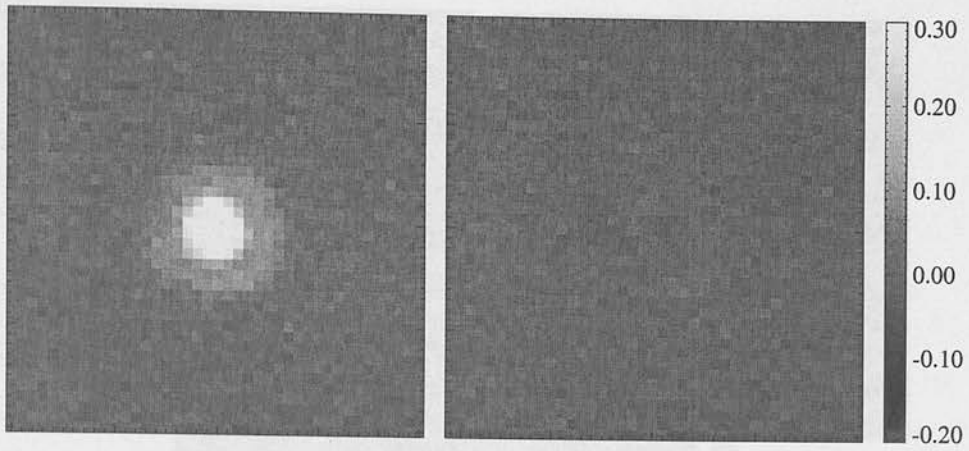


**Figure 4.10:** The final image of the PSF star HD157236 (left) and the residuals after subtracting the model PSF (right). The scale is such that the brightest pixel in the image has a value of 1.0.

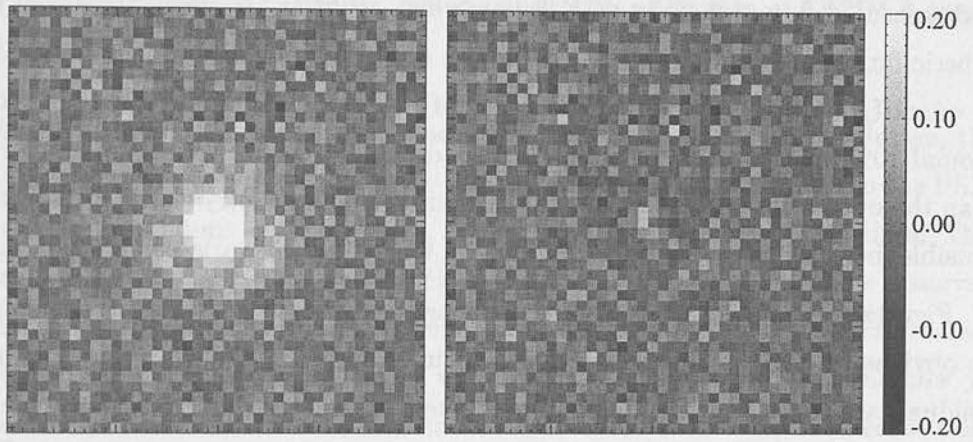


**Figure 4.11:** The final image of HD161868 (left) and the residuals after subtracting the model PSF (right). The scale is such that the brightest pixel in the image has a value of 1.0.

examined to determine whether the object is consistent with a point source, or whether there is any resolved component.

## 4.6 Results

HD161868 and HD220825 were both detected at 11.6 $\mu$m, with a signal to noise of 150 and 75 respectively within a circular aperture of radius 3 pixels (chosen to maximise signal to noise). HD220825 was not detected at 18.5 $\mu$m. As the 11.6 $\mu$m filter is not a standard N band filter, the photometric calibration was based on a model atmosphere of the standard star, normalised to its K band magnitude. Using this method, HD220825

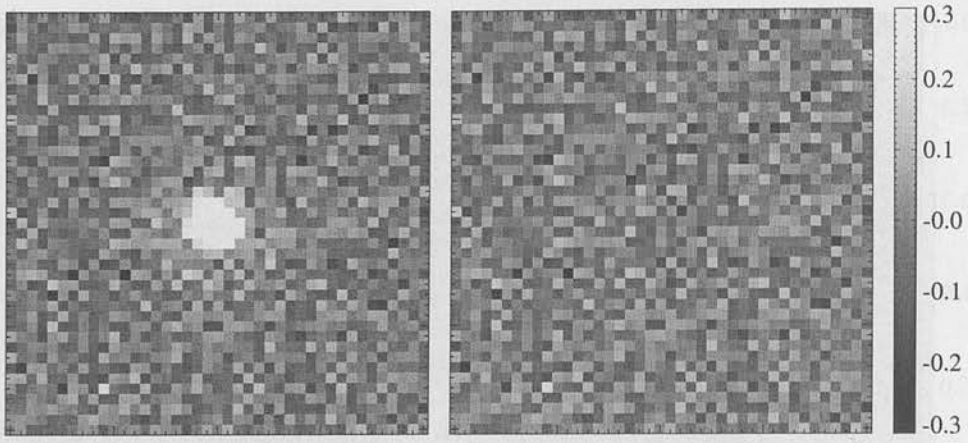


**Figure 4.12:** The final image of HD220825 (left) and the residuals after subtracting the model PSF (right). The scale is such that the brightest pixel in the image has a value of 1.0.

had measured flux of 0.42 Jy at 11.6 $\mu$m, which confirms an excess above the photospheric flux (estimated to be 0.317 Jy). The uncertainty on this measurement is hard to quantify as it depends on the accuracy of the model atmosphere, but is probably around 10%. No airmass correction was made, as this is likely to be a smaller effect than the uncertainty due to the model atmosphere. Photometry of HD161868 was not possible, because the atmospheric extinction was extremely variable over the night.

Figures 4.11 and 4.12 shows the final image and residuals after subtracting a PSF; no obvious resolved component is apparent in either case. To determine whether the residuals are consistent with being purely due to noise, the reduced $\chi^2$ was calculated within a circular region centred on the source. The results of this are shown in Figures 4.14 and 4.15. For HD161868, the high reduced $\chi^2$ value indicates that the observations are not consistent with the PSF. However when the residual images is smoothed, the reason for this becomes apparent (Figure 4.13). The residuals are high at the location of the source, and negative in a ring around the source. This is the opposite to what would be expected if the source were resolved. The likely reason for this is that the seeing had slightly improved over the course of the observations, so that the PSF model is slightly broader than the PSF for the science observation. In this case, the upper limit on the size of the disk is determined by the stability of the PSF. However, because there were no PSF observations at the end of the run (because bad weather interrupted the observations), it is not possible to quantify this variability, and hence set a limit on the size of the disk.

For HD220825, the $\chi^2$ plot indicates that the observations are entirely consistent

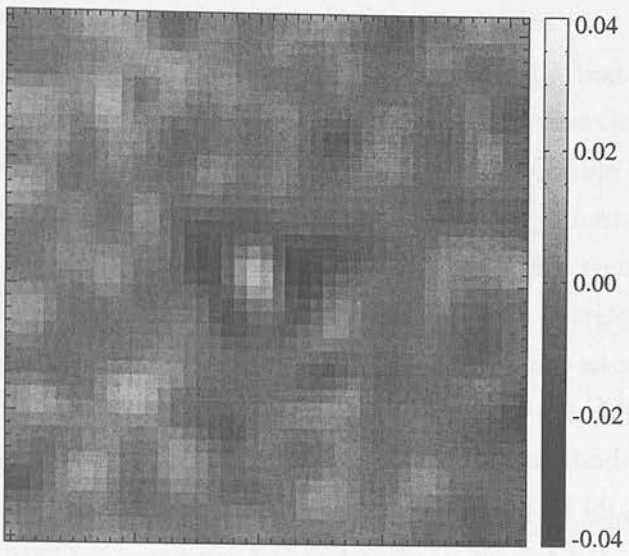


**Figure 4.13:** Residuals for HD161868, but smoothed with a Gaussian of FWHM 3 pixels. Scale is as for the unsmoothed residuals.

with the PSF model, so there is clearly no detection of extension. For this image, the limiting factor is the signal to noise of the observations, not the variability in the PSF. To obtain the upper limit on the disk size, an artificial disk was added to the data. This disk was simulated as a ring with an inclination of 45°, convolved with the observed PSF. The model was then fit to this simulated dataset, and the $\chi^2$ was calculated. This process was repeated several times with different disk radii, to find the how $\chi^2$ changed. The ratio of disk to star emission was assumed to be 0.32, as inferred from the colour corrected IRAS data and the photometry presented here. However, with the signal to noise obtained in these observations, the results of this simulation show that a disk cannot be detected regardless of its radius. If the radius is small, the disk cannot be distinguished from the stellar emission. If the radius is large, the surface brightness of the disk becomes low, and the disk cannot be detected above the sky noise. At no radius does the disk become detectable.

## 4.7 Discussion

Though these observations have not resolved either of the debris disks, they have produced useful information on what will be required to successfully image disks in the future. Though better weather is the most obvious requirement, several aspects of the observing method need to be improved for this technique to reach its full potential.

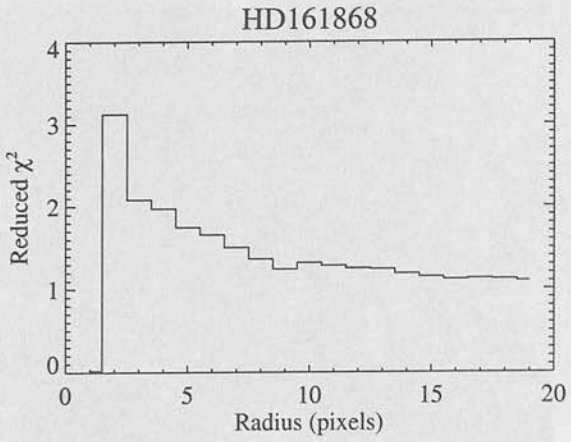


**Figure 4.14:** Reduced $\chi^2$ for HD161868 within a circular aperture centred on the source.

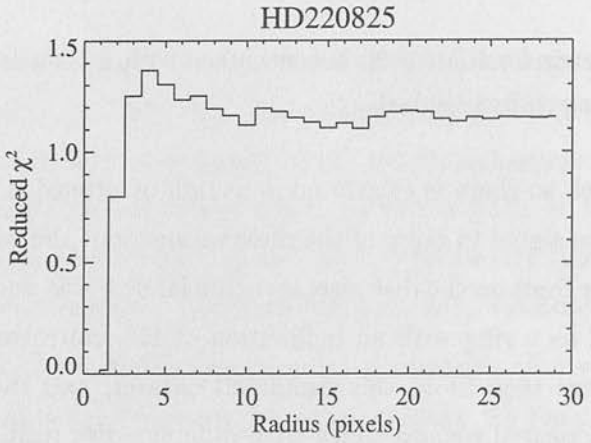


**Figure 4.15:** Reduced $\chi^2$ for HD220825 within a circular aperture centred on the source.

The most important factor in this type of observation appears to be the stability of the PSF. In the HD161868 observations this was the limiting factor, and furthermore because the PSF was not adequately monitored, it was impossible even to set upper limits on the disk size. A better strategy would have been to monitor the PSF throughout the observations, perhaps with a 10 minute PSF observation once every half hour. It may be possible to track the optical seeing using the guider, as this could provide useful information as to how the seeing changes throughout the night. Several other factors may also be important in matching the PSF observations to the science observations. The altitude of the source may have a significant effect on the PSF, so it may be necessary to take PSF observations both above and below the science target to quantify this effect. Also, the brightness of the guide star could have an effect on the

guiding accuracy, so guide stars should have similar magnitudes.

The quality of the flatfield also has a significant impact on the final results. In these observations, an excellent flatfield was produced for the first observing run using the natural sky variability, but on the second run this was not possible because the sky emission was too stable. In conditions suitable for 20 $\mu$m observations, the sky is likely to be very stable, and hence obtaining a flatfield could present a significant problem. Techniques for obtaining a good flatfield in stable weather must therefore be developed. At the moment, the best techniques are using the telescope dome as a flatfield source, or making special observations of the sky at different airmasses (i.e. different altitudes). Some experimentation will be required to determine the best method.

The effect of the source colour is also important. Some mid-IR filters are extremely broad, and the MICHELLE broad band N and Q filters have $\Delta\lambda/\lambda \sim 0.5$. The PSF star is being observed on the Rayleigh-Jeans side of its spectrum, so the majority of the photons detected would have a wavelength at the shortest end of this extreme. Conversely, the emission from a debris disk is still rising, so the majority of the detected photons would be at the longest wavelength that passes through the filter. With a broad band filter, this means that the PSF could be 50% bigger for the debris disk than for the PSF star. Such a difference would make it almost impossible to conclusively detect a marginally extended disk. The obvious solution is to use narrower filters. The filters used in this work have $\Delta\lambda/\lambda \sim 0.1$, so this effect is much reduced. However, this is probably the ultimate limit on using imaging to measure the size of a disk.

With the knowledge of MICHELLE PSF gained from these observations, the signal to noise requirements for future observations can be calculated. To do this, simulated star plus disk images were made using the model PSF, and then the pixel noise that would produce a 5 sigma detection of extension was calculated. The disks were again simulated by a ring with an inclination of 45° convolved with the PSF, and the minimum signal to noise was calculated to produce a reduced $\chi^2$ of 5.0 within an aperture centred on the source. The size of the aperture was chosen to maximise the sensitivity to the disk. The quoted signal to noise required is suitable for use in an integration time calculator, i.e. it is the signal to noise that would be produced if all of the flux was in the point source. The results of the simulations are shown in Figure 4.16. Interestingly, the disks which are easiest to detect have a radius similar to the PSF FWHM. Larger disks have a lower surface brightness, which makes them more difficult to detect above the sky noise. However, this method does somewhat overestimate the signal to noise required to detect large disks, as a circular aperture is probably not the best shape

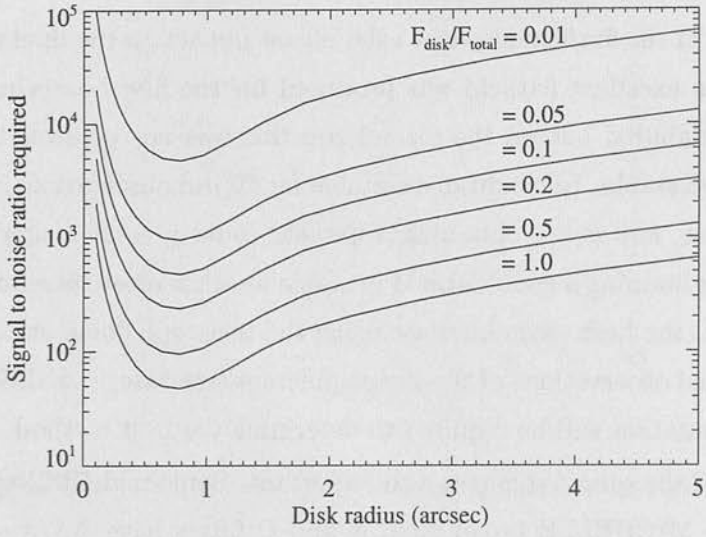


**Figure 4.16:** Signal to noise required for a 5 sigma detection of an extended disk, using MICHELLE on UKIRT. For Gemini, the radius should be halved.

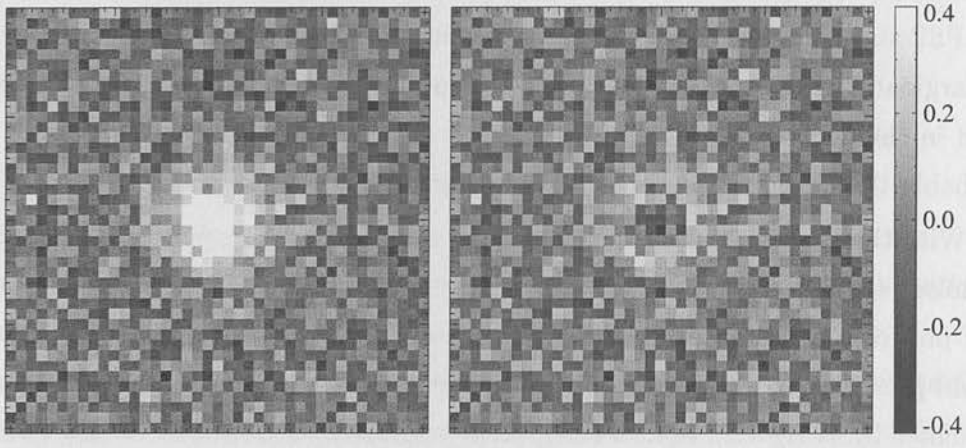


**Figure 4.17:** Simulated image showing a resolved disk that is detected at the 5 sigma level. On the left is the simulated images, and on the right are the residuals after subtracting the best fitting model. In this image the disk radius is 0.5 arcsec, and the disk flux contributes half of the source flux. The signal to noise ratio of the source is 91.5.

to choose for this purpose: for an inclined disk, an ellipse would give higher signal to noise. Figure 4.17 shows a simulated image with a disk that is only just detected.

## 4.8 Conclusion

This chapter has discussed mid-IR imaging observations of two debris disks using MICHELLE on UKIRT. Though neither of the disks were resolved, techniques were developed to reduce imaging data of marginally resolved disks, and the observations have provided a clearer idea of what is required for a successful program in the future. The key requirements are regular monitoring of the PSF (i.e. interleaved PSF star observations), a high quality flatfield and fairly narrow band filters. In addition, 20 $\mu$m observations are probably needed in most cases. Ultimately, the technique is limited by the stability of the PSF, and on the difference in colour between the PSF star and the debris disk.

# Chapter 5

# Observations of $H_2$ in circumstellar disks

## 5.1 Gas in young and old disks

For circumstellar disks around young stars, understanding the gas content is crucial to understanding the processes which are taking place. Planet formation is profoundly affected by the presence of a gas disk, as it provides the raw material for forming gas giant planets, and influences the planetesimal building process itself. The presence of gas alters the dust dynamics, causing certain grains to migrate inwards or outwards (Takeuchi and Artymowicz 2001; Takeuchi and Lin 2002). In addition, gas drag damps the orbital eccentricity and inclination of the dust grains in the disk, hence regulating the collisional velocities between grains. This is the key parameter in determining whether dust grains will stick together, and hence whether planetesimal growth will occur. Planet formation depends on circumstellar disks being a mixture of gas and dust, and both ingredients must be included in any attempt to understand the process. Though this thesis is mainly concerned with the dusty disks around main sequence stars, the immediate progenitors of these disks are dominated by gas. Understanding these gassy disks, and particularly transitional disks such as $\beta$ Pic, HR4796 and HD141569, is vital to understanding the origin of Vega excess disks.

The dominant component in the gassy disks around pre-main sequence stars is molecular hydrogen ($H_2$). However, observing emission from $H_2$ is not straightforward.

Near-IR (Bary et al. 2002), UV emission (Valenti et al. 2000) or absorption observations (Roberge et al. 2001) trace only the hottest gas or are dependent on the line of sight through the circumstellar disk. Mid-IR observations of the pure rotational emission lines of $H_2$ trace the bulk of the warm ($\sim$ 200 K) gas, but are difficult from ground-based sites, due to atmospheric absorption and the high mid-IR background emission. Because of these problems, many previous studies of circumstellar gas have relied on observations of tracer molecules, particularly CO (Mannings and Sargent 2000; Duvert et al. 2000). While these observations have been successful in tracing the velocity structure in disks, it seems that CO is a poor indicator of the total gas content. This is because CO can be destroyed by UV photons or frozen onto dust grains, leading to a severe underestimate of the total amount of gas (Dent et al. 1995).

The launch of the Infrared Space Observatory (*ISO*) and the recent development of ground based mid-IR spectrometers have made direct observations of warm $H_2$ possible. One of the most surprising results from these observations is the detection of large masses of $H_2$ in the disks around main sequence stars (Thi et al. 2001a). These results came from an *ISO* search for $H_2$ pure-rotational emission lines from pre-main sequence stars, and also young main sequence stars which are known to have dust disks. Thi et al. (2001b) report detections of the $H_2$ $J = 3 \rightarrow 1$ transition ($\lambda = 17.035$ $\mu$m) and $H_2$ $J = 2 \rightarrow 0$ transition ($\lambda = 28.221$ $\mu$m). However, as the *ISO* beam is large compared with the disks (beam size 14 $\times$ 27 arcsec) and the observations have moderate spectral resolution ($R \sim 2000$), these results cannot distinguish circumstellar disk emission from that of a foreground cloud or extended source. Follow up observations of both the pure rotational emission lines and $H_2$ in absorption have provided strong evidence that the warm $H_2$ is extended in sources selected from the *ISO* studies. Using the echelle spectrometer, TEXES, Richter et al. (2002) obtained observations of six sources, three of which have reported *ISO* $H_2$ detections (Thi et al. 2001b): HD163296, AB Aur and GG Tau. They obtained upper limits on the line fluxes from five sources, with a possible 2 sigma detection of the $H_2$ $J = 3 \rightarrow 1$ S(0) line in AB Aur and conclude that the majority of the $H_2$ emission detected by *ISO* is extended on scales of 5 arcsec or more. The far-UV spectrum of $\beta$ Pic presented by Lecavelier des Etangs et al. (2001) shows a complete absence of $H_2$ absorption lines, contrary to expectations if large quantities of $H_2$ are present within the edge-on dust disk.

These observations have a significant impact on the understanding of the debris disks around main sequence stars. The modelling of dust disks around main sequence stars presented in Chapter 3 assumes that there is little gas in the disks, and hence

| Object | Date | Wavelength $\mu$m | Slit width pixels | Pixel scale on-sky arcsec | Integration time seconds |
|---|---|---|---|---|---|
| AB Aur | 29 Dec 2001 | 12.279 | 2 | 0.59×0.24 | 1900 |
| | 29 Dec 2001 | 17.035 | 2 | 0.50×0.28 | 3400 |
| CQ Tau | 30 Dec 2001 | 17.035 | 4 | 0.50×0.28 | 5900 |

**Table 5.1:** Summary of observations. The long axis of the pixel scale refers to the direction along the slit; the pixel scale perpendicular to this direction is different due to anamorphic demagnification (Schweizer 1979).

the gas forces are negligible. However, if the detection of large quantities of gas in main sequence debris disks is real, then this modelling is likely to be seriously flawed. It is therefore important to establish whether the tentative detection of $H_2$ in disks surrounding main sequence targets is real or not. This chapter presents ground based observations made using the high resolution mid-IR spectroscopy mode of MICHELLE, the mid-IR echelle spectrometer on the ground-based United Kingdom Infrared Telescope (UKIRT). The observations are of two pre-main sequence stars, CQ Tau (distance 100 pc) and AB Aur (distance 142 pc), both of which have good *ISO* detections and one of which (AB Aur) was also observed by Richter et al. (2002). Though it would have been desirable to observe main sequence targets with an *ISO* $H_2$ detection, poor weather and target availability meant that only pre-main sequence targets could feasibly be observed. However, this serves as a check on the methods employed by Thi et al. (2001b), and the results shed light on the nature of all the $H_2$ detections in their sample.

## 5.2 Observations and data reduction

Mid-IR echelle spectroscopy of AB Aur and CQ Tau was carried out on 2001 December 29 and 30 using MICHELLE (Glasse et al. 1997) on UKIRT. AB Aur and CQ Tau were observed in the $H_2$ $J = 3 \rightarrow 1$ transition ($\lambda = 17.035$ $\mu$m), providing direct comparison with the *ISO* observations. AB Aur was also observed in the $H_2$ $J = 4 \rightarrow 2$ transition ($\lambda = 12.279$ $\mu$m). The $H_2$ $J = 2 \rightarrow 0$ transition ($\lambda = 28.221$ $\mu$m) was used in the *ISO* observations, but is not readily accessible from the ground due to the structure of the atmospheric transmission at 28 $\mu$m. Table 5.1 shows the details of the observations.

The echelle grating on MICHELLE was used to provide maximum sensitivity to the $H_2$ lines, which are expected to be unresolved. AB Aur was observed with a 2-pixel slit

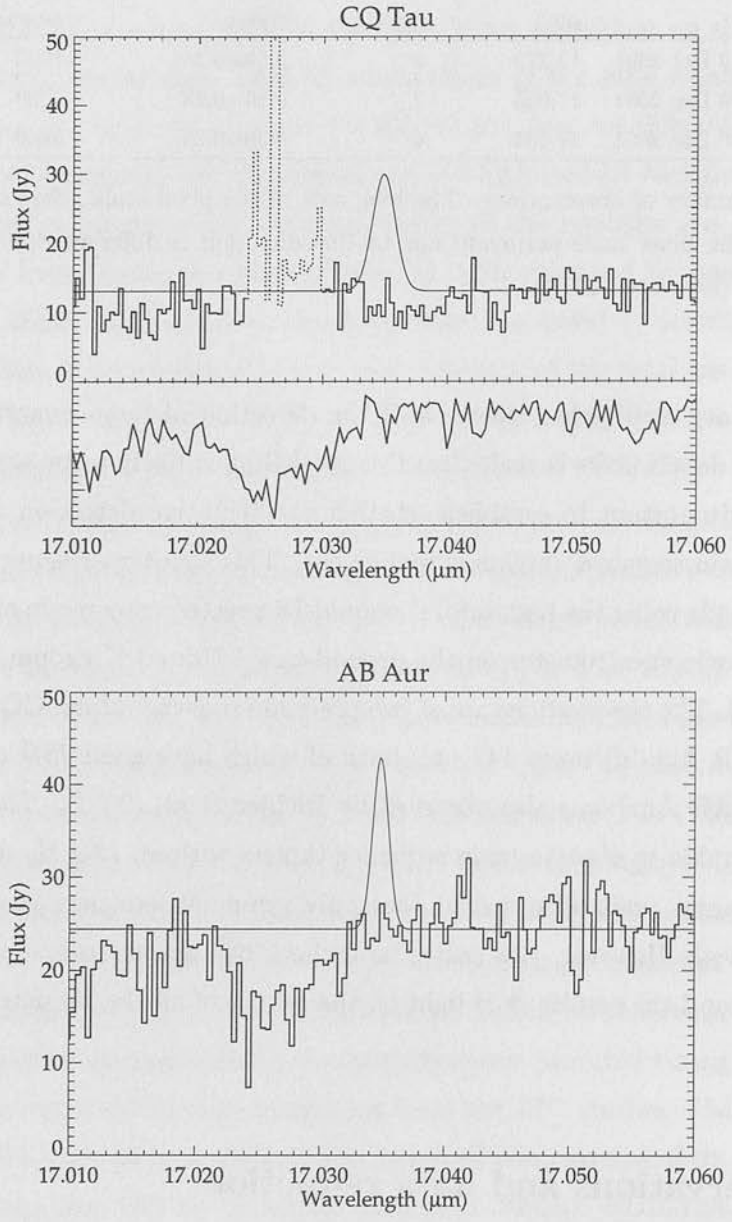


**Figure 5.1:** Spectra of the $H_2$ $J = 3 \rightarrow 1$ transition for AB Aur and CQ Tau, with an optimal extraction. For comparison, gaussians are shown with the same integrated flux as the *ISO* measurements reported in Thi et al. (2001b), assuming an intrinsic line width of 20 km $s^{-1}$. The CQ Tau spectrum has been masked out at regions of high noise (shown by the use of dotted lines); the lower panel shows the standard star observation, scaled from 0.0 to 1.0, to demonstrate that the masked regions correspond to atmospheric absorption lines. For AB Aur, the standard star observation was saturated, which causes the variability in the continuum level.

width; CQ Tau with a 4-pixel slit width. The resolving power was $R = 15\,200$ at 12 $\mu$m and $R = 18\,600$ ($R = 9\,300$) at 17 $\mu$m for a two (four) pixel wide slit; as a result the $H_2$ lines are well separated from the bright sky lines. A single order from the grating is selected using blocking filters.

Because the data were taken in high resolution spectroscopy mode, the signal from the warm sky and optics is much fainter than for the imaging data discussed in Chapter 4. In addition, the sky emission is spectrally resolved into discreet sky lines, and variability in the sky is restricted to variation in the strength of these lines. This means that it is possible to make observations without using chopping, so long as the interesting part of the target's spectrum is well separated from any sky lines. The point-like sources were all observed by nodding along the 70 arcsec long slit, which was orientated north-south on the sky. The separation of the two beams was 15 arcsec and the dwell-time in each beam was 40 seconds.

The data reduction software was written in the IDL programing language, and is similar to the system used to reduce imaging data described in Chapter 5. Aside from the obvious difference that the here the dataset is spectroscopic and not chopped, the other major difference is that because the sky signal is much weaker due to the high dispersion, it was not possible to create a flatfield using variation in the sky level. Instead, the flatfield was based on observations of the standard star.

To reduce the data, pairs of frames from different nod positions were subtracted, giving a set of difference frames each containing a positive and a negative version of the source. In each frame, the positive and negative versions were combined to give a single 2D spectrum. The noise was then assessed by measuring the variance of each pixel through all the frames. This noise map was used to make a bad pixel mask, where any particularly noisy pixels (more than 50% worse than the median noise level) were flagged as being bad. At this stage a sky subtraction was done, by fitting a simple function to each column in each frame. This function was by default a straight line with a gradient, but if a column had several bad pixels, a constant was subtracted instead. In fitting the sky function, pixels containing emission from the source were masked out. Before the set of 2D spectra were combined into a final image, the dataset was despiked using an iterative sigma cut. To do this, all of the 2D spectra were compared, and data points were flagged as bad if they were further than a specified number of standard deviations from the mean of their pixel. This sigma cut was done three times with threshold settings of 6, 4 and 3 sigma.

Once a final 2D spectrum had been produced, 1D spectra were extracted in two

| Object | Wavelength | Line flux | | |
|---|---|---|---|---|
| | $\mu$m | $\times 10^{-14}$ ergs s$^{-1}$ cm$^{-2}$ | | |
| | | Wide extraction | Optimal extraction | *ISO* Result |
| AB Aur | 12.297 | $5.4 \pm 3.8$ | $4.8 \pm 2.1$ | |
| | 17.035 | $< 14.6$ | $< 8.9$ | $30 \pm 9$ |
| CQ Tau | 17.035 | $< 13.0$ | $< 6.7$ | $40 \pm 12$ |

**Table 5.2:** Summary of results. All upper limits are 3 sigma. *ISO* results are taken from Thi et al. (2001b).

ways: a wide extraction which summed all the emission in a 6.5 arcsec region centred on the source, and an optimal extraction of the continuum. The optimal extraction method takes a weighted mean of the pixels around the source, giving more weight where the continuum is brighter. This method gives the lowest possible noise on the continuum level, but if the $H_2$ emission region is more extended than the continuum emission then it will underestimate the $H_2$ line flux. An example of the two methods is shown in Figures 5.2 and 5.3. For both extraction methods a sky subtraction was done first, estimating the residual sky signal in each column using pixels between 3.5 and 7 arcsec from the source. The noise on the final 1D spectra were estimated by measuring the variation in the continuum in regions away from sky lines and the expected location of the $H_2$ line. This noise estimate was chosen instead of using the measured noise map, as it will include all detector effects (e.g. systemic variation in the dark current), which would not show up otherwise.

Standard stars were observed and reduced in the same way as the science targets. The final spectrum for each object was divided through by a standard spectrum to remove wavelength dependant variations in atmospheric and instrumental transmission. The standard stars were observed using the same rows on the detector as the sources, and division by the standard effectively flat-fields the detector. For the 17 $\mu$m observations of AB Aur the standard star observation was saturated, so this correction was not possible. This causes variation in the continuum level, but would not prevent the detection of a narrow emission line.

Wavelength calibration was obtained by measuring the positions of sky lines, and comparing the positions to a model sky spectrum. One sigma errors on the wavelength calibration are estimated to be about one pixel ($\sim 3 \times 10^{-4}$ $\mu$m), largely due to the difficulty in centroiding the broad sky lines. The spectra were shifted to the object's rest frame, accounting for the radial velocity of the Earth and object's heliocentric radial

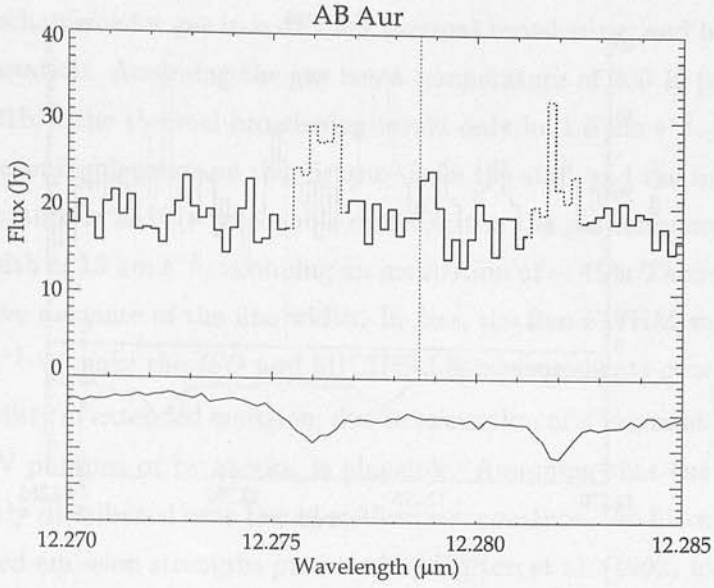


**Figure 5.2:** Spectra of the $H_2$ $J = 4 \rightarrow 2$ transition for AB Aur, using optimal extraction. The vertical dotted line shows to the expected location of the transition. Noisy regions have been masked out and the standard star is shown in the lower panel, as in Figure 1.

velocity (+8.9 km $s^{-1}$ for AB Aur and +22.6 km $s^{-1}$ for CQ Tau (Barbier-Brossat and Figon 1999)). Flux calibration was based on the observed continuum level and published continuum flux measurements from Thi et al. (2001b) for both the 17 $\mu$m spectra and Richter et al. (2002) for the AB Aur 12 $\mu$m spectrum.

## 5.3 Results

Figures 5.1 and 5.2 show the final spectra produced using an optimal extraction. At the location of sky lines the noise increases dramatically, so these regions have been masked out (i.e. they were not used when estimating the continuum level and the overall noise). On the 17 $\mu$m figures a gaussian with the total line flux measured by Thi et al. (2001b) is shown, to allow comparison between the *ISO* results and the new spectra. As the *ISO* observations do not resolve the line, an intrinsic line width of 20 km $s^{-1}$ is assumed (see Section 5.4 for discussion of this value), with an instrumental width of 16 km $s^{-1}$ for AB Aur and 32 km $s^{-1}$ for CQ Tau, giving a total width of 26 km $s^{-1}$ and 38 km $s^{-1}$ respectively. The MICHELLE sensitivities should have produced a clear detection of the line if all of the flux in the 14 × 27 arcsec *ISO* beam were contained within the extracted MICHELLE beam, as expected for emission from an unresolved

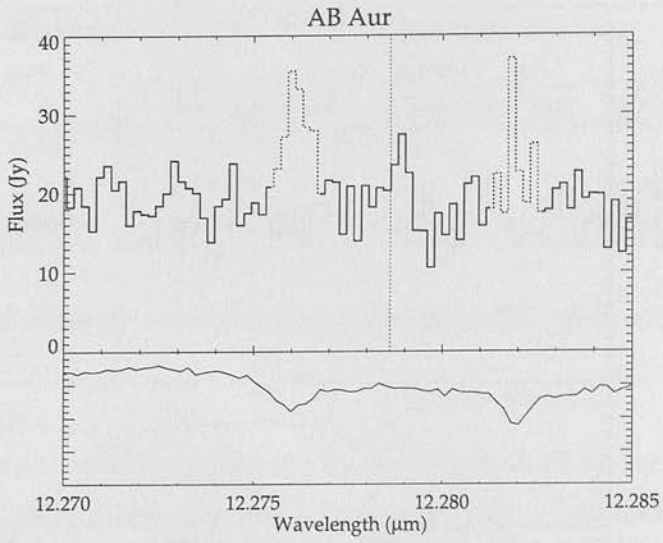


**Figure 5.3:** As for figure 5.2, but including all flux within a 6.5 arcsec region centred on the source instead of using the optimal extraction method.

disk.

To estimate the line flux, all of the flux within a 40 km $s^{-1}$ wide bin centred on the systemic velocity was summed, after subtracting the continuum level. Fluxes and upper limits for all extraction methods are shown in Table 5.2. There is no evidence of $H_2$ emission in either of the 17 $\mu$m spectra. The 12 $\mu$m optimally extracted spectrum gives flux of $4.8 \pm 2.1$ ergs $s^{-1}$ $cm^{-2}$, but as this is only a 2.3 sigma result should not be regarded as a definite detection. However, this result is consistent with the tentative detection by Richter et al. (2002), who measure $(2.0 \pm 1.0) \times 10^{-14}$ ergs $s^{-1}$ $cm^{-2}$ with a width of 10.5 km $s^{-1}$.

## 5.4 Discussion

Despite the enhanced sensitivity to narrow emission lines from a point-like source, these new spectra of AB Aur and CQ Tau show no convincing detections of either the 0-0 S(1) or 0-0 S(2) lines. In order for the 0-0 S(1) $H_2$ emission to be detectable by *ISO* but not by MICHELLE, the emission would have to be either spectrally broad or spatially extended. These two explanations are considered in turn.

The spectral resolving power of the *ISO* observations is R $(= \frac{\lambda}{\delta\lambda}) = 2400$, and the $H_2$ lines Thi et al. (2001b) observed are unresolved. In calculating upper limits, the lines are assumed to have an intrinsic width of 20 km $s^{-1}$. The dominant line

broadening mechanisms for gas in a disk are thermal broadening, and bulk motion due to the disk's rotation. Assuming the gas has a temperature of 200 K (as estimated by Thi et al. (2001b)), the thermal broadening would only be 1.5 km $s^{-1}$. The amount of rotational broadening depends on the distance from the star, and the inclination of the disk. If the distance is 2AU (a reasonable choice, given the gas temperature of 200 K), this gives a width of 15 km $s^{-1}$, assuming an inclination of $\sim 45°$. Therefore, 20 km $s^{-1}$ is a conservative estimate of the line width. In fact, the line FWHM would have to be over 100 km $s^{-1}$ to make the *ISO* and MICHELLE measurements consistent.

The possibility of extended emission, due to excitation of a remnant cloud of molecular gas by UV photons or by shocks, is plausible. Assuming that the *ISO* measured flux is uniformly distributed over the $14 \times 27$ arcsec aperture, the fluxes are consistent with UV-excited emission strengths predicted by Burton et al. (1992) for moderate UV field strengths ($10^3 - 10^4$ times that of the interstellar medium) and moderate densities ($n_{H_2} \sim 10^3 - 10^4 cm^{-3}$). The sky subtraction region used on the MICHELLE observations (3.5 – 7 arcsec radius) means that they are insensitive to emission from any source bigger than around 3.5 arcsec. The hypothesis of extended emission is strengthened for AB Aur since a map of $^{12}CO$ $3 \rightarrow 2$ shows an extended molecular cloud around the central source, with a size of at least 30 arcsec (Thi et al. 2001b). For CQ Tau, no $^{12}CO$ $3 \rightarrow 2$ line was detected, but this could be reconciled with extended $H_2$ emission if the CO has been destroyed by photodissociation (Dent et al. 1995).

In interpreting the results, an important question concerns the optical depth of the dust disk. If the dust is optically thick at the observed wavelengths and the gas and dust are at the same temperature, then the gas would be equally likely to absorb or emit a photon, so no emission line would be produced. Line emission will only occur if there are gaps in the dust disk, or if there is a hot atmosphere above the disk. Though these situations are quite plausible, only a small fraction of the gas in the disk would be observed in this case, and any calculation of the gas mass would underestimate the true mass. It is therefore essential that the optical depth of the disk is known in order to correctly interpret the results.

The optical depth of the disks can be estimated from radiative transfer models based on the SED of the disks. Natta et al. (2001) made models of the disk SEDs for both AB Aur and CQ Tau, and their fitted parameters can be used to determine whether the disks are optically thick at 12 and 17 $\mu$m. Based on their estimates of disk mass and disk radius, and using the usual assumption that the dust opacity at 1.3 mm is $\kappa_{1.3mm} = 0.01$ $cm^2$ $g^{-1}$, the average optical depth of the disks at 1.3 mm is 0.03 for AB

Aur and 0.24 for CQ Tau. Then, using a power law dust opacity index ($\kappa \propto \lambda^{-\beta}$, where $\beta$ was estimated to be 2.0 for AB Aur and 1.0 for CQ Tau in Natta et al. 2001), the optical depth can be estimated at shorter wavelengths. This indicates that the disks become optically thick at wavelengths shorter than 200 $\mu$m for AB Aur and 300 $\mu$m for CQ Tau. Both disks must therefore have a high optical depth at 12 and 17 $\mu$m.

This result has two important implications. Firstly, this means that the upper limits on line flux cannot be used to calculate upper limits on the mass of $H_2$ in the disk, as most of the gas in the disk is hidden by the optically thick dust. The $H_2$ line in the 12 $\mu$m AB Aur spectrum (if confirmed) must arise from a hot atmosphere above the disk, or from gaps in the dust disk. Secondly, if the lines detected by *ISO* do arise in the disk, then only a small fraction of the gas was observed and the total gas mass must be much higher than was estimated.

In conclusion, a search for pure rotational $H_2$ emission lines from the circumstellar disks of AB Aur and CQ Tau has been undertaken. Emission from AB Aur is tentatively detected, but there is no evidence for emission from CQ Tau. The likely reason for this non-detection is that the disks are optically thick in the mid-IR. The upper limits on line flux are significantly smaller than previous line flux estimates based on *ISO* observations, which suggests that the emission detected by *ISO* is extended on scales of at least 6 arcsec (or $>$ 60AU).

Mapping the emission over the area covered of the *ISO* beam is one approach to confirming these conclusions. Detecting the faint extended emission will require a considerable gain in sensitivity over these observations, such as is anticipated using MICHELLE on the Gemini North 8-m telescope.

# Chapter 6

# Conclusion

Understanding the Vega phenomenon is a challenging task, and a variety of observational and theoretical techniques must be brought together to get a complete picture of the processes which are taking place. This thesis has described three observational projects aimed at studying Vega-type disks, and theoretical modelling of disk SEDs using realistic dust grain models. The main conclusions of this work are summarised here.

The first part of the thesis presented new sub-mm observations of Vega excess stars, and modelling for all known Vega excess stars which have sub-mm data. Several resolved disks were modelled, and this showed that different objects require very different dust grain properties to get a good fit. In particular, the dust grains around older stars tend to have lower porosity than those around younger stars. This may indicate that collisions in the disks have reprocessed the initially fluffy grains into a more solid form. $\epsilon$ Eri appears to be deficient in small dust grains compared to the best fitting model, which may be due to factors which affect the size distribution of grains close to the radiation pressure blowout limit. The model was also applied to several unresolved disks, with the aim of estimating the disk size. However, the large diversity in dust composition for the resolved disks meant that it was impossible to make a reliable assumption as to the composition of the grains in the unresolved disks, and there is corresponding uncertainty in the estimated disk size. In addition, the poor fit for $\epsilon$ Eri shows that the model cannot always account for the SED even if the disk size is known. These two factors mean that it may not be possible to determine a disk's size without

actually resolving it.

The second part of the thesis described mid-IR observations designed to directly resolve the disks around several nearby main sequence stars, and hence obtain a direct measurement of the disk size. An analytical model of the telescope PSF was developed and fitted to observations of standard stars, and this model was used to establish whether the science observations were consistent with a point source, or if they showed evidence for a resolved disk. Though the observations failed to resolve any of the targets, techniques were developed to reduce imaging data of marginally resolved disks, and the observations have provided a clearer idea of what is required for a successful program in the future. Observations at 20 $\mu$m are likely to be essential to resolve most disks, and given that weather conditions adequate for such observations are rare at most observing sites, flexible scheduling is important to ensure that 20 $\mu$m observations are made whenever the conditions are good enough. For marginally resolved disks, frequent PSF observations are necessary, and narrow bandpass filters are needed to avoid colour effects due to the difference in colour between the disk and the PSF star.

Finally, in the third part of the thesis I presented the results of a search for molecular hydrogen using MICHELLE, the mid-IR echelle spectrometer at the UK Infrared Telescope. Due to weather constraints, the observations focused on two pre-main sequence stars, AB Aur and CQ Tau. No significant emission lines were detected from either star, but the upper limits on line flux were significantly smaller than those measured from existing *ISO* observations, which suggests that the emission detected by *ISO* is extended on scales of at least 6 arcsec, and does not come from the disk as previously thought. These observations showed that ground based searches for molecular hydrogen are definitely viable: this was a successful project in spite of poor weather conditions. A larger observing program is a natural next step, including stars with a variety of different ages and spectral types. Given that T Tauri and HAeBe systems are likely to have be optically thick dust disks, the best candidates for this type of project are probably the transitional disks like $\beta$ Pic and HR4796, as for these targets a direct measurement of the $H_2$ mass should be possible.

## 6.1 Future observations

Progress in the study of Vega disks depends most critically on improving the quality of the observations. The following are perhaps the most important areas.

- **Asymmetries.** One of the most interesting aspects of Vega-type disks are the clumps and warps that have been detected in the resolved disks. Better images are urgently needed, firstly to confirm that the asymmetries are real, and secondly to provide detailed constraints to help determine what is causing them. More resolved disks are also required to see how common these asymmetries are. SOFIA is likely to be the most important instrument for this type of work in the near future, because of its high resolution ($\sim$ 3 arcsec at 30 $\mu$m).

- **Surveys of the Vega-type population.** Future surveys, including the upcoming surveys by SIRTF and eventually ALMA, are needed to tie down the basic details of the Vega-type disk population. In particular, the evolution of the population must be quantified more accurately, as well as the effects of stellar metallicity and binarity.

- **Planet + disk searches.** There is presently very little overlap between the Vega disk population and the extrasolar planet population; this may be a real effect, or it may be due to the selection effects involved. To resolve this problem, Vega disk searches must be made more sensitive in order to detect the faint disks around cooler, older stars, and planet searches must be extended to hotter, younger stars. For disk searches, SIRTF should make significant progress in this direction; for planet searches, the astrometric technique will be useful on stars regardless of their age and spectral type.

- **Dust grain evolution.** The tentative detection of porosity evolution discussed in Chapter 3 is a very important discovery, if it turns out to be real. However, further observations are required to increase the size of the sample and hence confirm a statistically significant effect. This means spatially resolving more disks.

- **Gas content of debris disks.** Understanding the gas content of debris disks is essential for dynamical modelling. Extending the $H_2$ work from Chapter 5 to a large sample of debris disks at different ages would be significant help in this respect. The key aims would be to determine which process removes the gas from the disk, and what timescale this happens on.

## 6.2 Future theory

From a theoretical point of view, there are several key areas that are in need of attention.

- **Velocity evolution.** In order to build large planetesimals, Vega disks must previously have had low collisional velocities. However, the current state of the disks indicate that they now have high collisional velocities. Kenyon and Bromley (2001) showed that gravitational stirring by a planet can produce the observed change in collisional velocity, but if this is the only explanation, then all Vega disks must contain an embedded planet, or at least have had one in the past. Further work is needed to determine whether this model can explain the observed properties of the Vega type disk population, in particular the timescale for the onset of the collisional cascade, and the subsequent evolution in disk flux.

- Dust **production mechanism.** Modelling is needed to determine what the dust production mechanism is in disks like $\beta$ Pic and HR4796. These disks are warm enough that sublimation could be an important process, but collisional dust production is also likely to be significant. For $\beta$ Pic, significant constraints are given by the observations of gas in the disks (Brandeker et al. 2004), so it should be possible to include the details of both dust and gas production.

- **Size distribution model.** The size distribution model used in Chapter 3 is known to be too simplistic near the blowout limit, and a more complete model would include the detail of dust creation, destruction and transport in this size regime. However, such a model would introduce several extra free parameters (critically, the collisional velocities of the grains) which are currently very difficult to constrain observationally.

## 6.3 Final word

The future for Vega disk studies certainly looks interesting, but it also looks difficult. The field is still quite limited by the lack of sensitive, high resolution instruments in the mid-IR, far-IR and sub-mm. Though SOFIA is likely to provide the next step in this direction, for longer wavelengths and higher resolutions observers will have to wait for ALMA and JWST, neither of which are expected to see first light before 2011. From a theoretician's point of view this is also a significant problem, as any realistic model of a Vega disk includes a large number of parameters which have few observational constraints. The likely remedy is to focus on younger disks (around 10–20 Myr) such as $\beta$ Pic and HR4796. These objects emit strongly in the mid-IR, and so observers will be able to take advantage of both conventional mid-IR imaging on 10 meter class

telescopes, and mid-IR interferometry with VLTI and Keck. The younger objects are also likely to give insight into the key processes which shape Vega disks, including the evolution of gas within the disk, and the transition from constructive to destructive collisions.

# Bibliography


Adams, F. C. and Benz, W.: 1992, in *ASP Conf. Ser. 32: IAU Colloq. 135: Complementary Approaches to Double and Multiple Star Research*, pp 185–+

Adams, F. C. and Lin, D. N. C.: 1993, in *Protostars and Planets III*, pp 721–748

Archibald, E. N., Wagg, J. W., and Jenness, T.: 2000, http://www.jach.hawaii.edu/JACdocs/JCMT/SCD/SN/ 002.2/

Artymowicz, P.: 1989, in *Dynamics of Astrophysical Discs*, pp 43–+

Artymowicz, P.: 1997, *Annual Review of Earth and Planetary Sciences* **25**, 175

Augereau, J. C., Lagrange, A. M., Mouillet, D., and Ménard, F.: 1999a, A&A **350**, L51

Augereau, J. C., Lagrange, A. M., Mouillet, D., Papaloizou, J. C. B., and Grorod, P. A.: 1999b, A&A **348**, 557

Augereau, J. C., Nelson, R. P., Lagrange, A. M., Papaloizou, J. C. B., and Mouillet, D.: 2001, A&A **370**, 447

Aumann, H. H., Beichman, C. A., Gillett, F. C., de Jong, T., Houck, J. R., Low, F. J., Neugebauer, G., Walker, R. G., and Wesselius, P. R.: 1984, ApJ **278**, L23

Aumann, H. H. and Probst, R. G.: 1991, ApJ **368**, 264

Backman, D. E. and Paresce, F.: 1993, in *Protostars and Planets III*, pp 1253–1304

Barbier-Brossat, M. and Figon, P.: 1999, *VizieR Online Data Catalog* **3213**, 0

Barrado y Navascués, D., Stauffer, J. R., Song, I., and Caillault, J.-P.: 1999, ApJ **520**, L123

Bary, J. S., Weintraub, D. A., and Kastner, J. H.: 2002, ApJ **576**, L73

Beckwith, S. V. W., Henning, T., and Nakagawa, Y.: 2000, *Protostars and Planets IV* pp 533–+

Beckwith, S. V. W. and Sargent, A. I.: 1991, ApJ **381**, 250

Beichman, C. A., Neugebauer, G., Habing, H. J., Clegg, P. E., and Chester, T. J.: 1988a, in *NASA RP-1190, Vol. 1 (1988)*, pp 0–+

Beichman, C. A., Neugebauer, G., Habing, H. J., Clegg, P. E., and Chester, T. J. (eds.): 1988b, *Infrared astronomical satellite (IRAS) catalogs and atlases. Volume 1: Explanatory supplement*

Birkinshaw, M.: 1994, in *ASP Conf. Ser. 61: Astronomical Data Analysis Software and Systems III*, pp 249–+

Boccaletti, A., Augereau, J.-C., Marchis, F., and Hahn, J.: 2003, ApJ **585**, 494

Bodenheimer, P. and Lin, D. N. C.: 2002, *Annual Review of Earth and Planetary Sciences* **30**, 113

Bohren, C. F. and Huffman, D. R.: 1983, *Absorption and scattering of light by small particles*, New York: Wiley, 1983

Boss, A. P.: 1997, *Science* **276**, 1836

Boss, A. P.: 2003, ApJ **599**, 577

Brandeker, A., Liseau, R., Olofsson, G., and Fridlund, M.: 2004, A&A **413**, 681

Brittain, S. D., Rettig, T. W., Simon, T., Kulesa, C., DiSanti, M. A., and Dello Russo, N.: 2003, ApJ **588**, 535

Burns, J. A., Lamy, P. L., and Soter, S.: 1979, *Icarus* **40**, 1

Burrows, C. J., Krist, J. E., Stapelfeldt, K. R., and WFPC2 Investigation Definition Team: 1995, *Bulletin of the American Astronomical Society* **27**, 1329

Burton, M. G., Hollenbach, D. J., and Tielens, A. G. G.: 1992, ApJ **399**, 563

Campo Bagatin, A., Cellino, A., Davis, D. R., Farinella, P., and Paolicchi, P.: 1994, Planet. Space Sci. **42**, 1079

Clampin, M., Krist, J. E., Ardila, D. R., Golimowski, D. A., Hartig, G. F., Ford, H. C., Illingworth, G. D., Bartko, F., Benítez, N., Blakeslee, J. P., Bouwens, R. J., Broadhurst, T. J., Brown, R. A., Burrows, C. J., Cheng, E. S., Cross, N. J. G., Feldman, P. D., Franx, M., Gronwall, C., Infante, L., Kimble, R. A., Lesser, M. P., Martel, A. R., Menanteau, F., Meurer, G. R., Miley, G. K., Postman, M., Rosati, P., Sirianni, M., Sparks, W. B., Tran, H. D., Tsvetanov, Z. I., White, R. L., and Zheng, W.: 2003, AJ **126**, 385

Clampin, M., Krist, J. E., Golimowski, D. A., Ardila, D. R., Bartko, F., Benítez, N., Blakeslee, J. P., Bouwens, R., Broadhurst, T. J., Brown, R. A., Burrows, C., Cheng, E., Cross, N., Feldman, P. D., Ford, H. C., Franx, M., Gronwall, C., Hartig, G., Illingworth, G. D., Infante, L., Kimble, R. A., Lesser, M., Martel, A. R., Menanteau, F., Meurer, G. R., Miley, G., Postman, M., Rosati, P., Sirianni, M., Sparks, W. B., Tran, H. D., Tsvetanov, Z. I., White, R. L., and Zheng, W.: 2002, *American Astronomical Society Meeting* **201**, 0

de Pater, I. and Lissauer, J.: 2001, *Planetary Sciences*, Planetary Sciences, by Imke de Pater and Jack Lissauer. Cambridge University Press, 2001, 544 pp.

Dent, W. R. F., Greaves, J. S., Mannings, V., Coulson, I. M., and Walther, D. M.: 1995, MNRAS **277**, L25

Dermott, S. F., Grogan, K., Gustafson, B. A. S., Jayaraman, S., Kortenkamp, S. J., and Xu, Y. L.: 1996, in *ASP Conf. Ser. 104: IAU Colloq. 150: Physics, Chemistry, and Dynamics of Interplanetary Dust*, pp 143–+

Dohnanyi, J. W.: 1969, J. Geophys. Res. **74**, 2531

Dunne, L. and Eales, S. A.: 2001, MNRAS **327**, 697

Durda, D. D. and Dermott, S. F.: 1997, *Icarus* **130**, 140

Durda, D. D., Greenberg, R., and Jedicke, R.: 1998, *Icarus* **135**, 431

Duvert, G., Guilloteau, S., Ménard, F., Simon, M., and Dutrey, A.: 2000, A&A **355**, 165

Fajardo-Acosta, S. B., Beichman, C. A., and Cutri, R. M.: 2000, ApJ **538**, L155

Fajardo-Acosta, S. B., Stencel, R. E., and Backman, D. E.: 1997, ApJ **487**, L151+

Fajardo-Acosta, S. B., Stencel, R. E., Backman, D. E., and Thakur, N.: 1999, ApJ **520**, 215

Fajardo-Acosta, S. B., Telesco, C. M., and Knacke, R. F.: 1998, AJ **115**, 2101

Fisher, R. S., Telesco, C. M., Piña, R. K., Knacke, R. F., and Wyatt, M. C.: 2000, ApJ **532**, L141

Fruchter, A. S. and Hook, R. N.: 2002, PASP **114**, 144

Gillett, F. C.: 1986, in *ASSL Vol. 124: Light on Dark Matter*, pp 61–69

Glasse, A. C., Atad-Ettedgui, E. I., and Harris, J. W.: 1997, in *Proc. SPIE Vol. 2871, p. 1197-1203, Optical Telescopes of Today and Tomorrow, Arne L. Ardeberg; Ed.*, Vol. 2871, pp 1197–1203

Gliese, W.: 1969, *Veroeffentlichungen des Astronomischen Rechen-Instituts Heidelberg* **22**, 1

Golimowski, D. A., Durrance, S. T., and Clampin, M.: 1993, ApJ **411**, L41

Grady, M. M.: 2003, *Astronomy and Geophysics* **44**, 9

Gray, R. O. and Corbally, C. J.: 1994, AJ **107**, 742

Greaves, J. S., Holland, W. S., Moriarty-Schieven, G., Jenness, T., Dent, W. R. F., Zuckerman, B., McCarthy, C., Webb, R. A., Butner, H. M., Gear, W. K., and Walker, H. J.: 1998, ApJ **506**, L133

Greaves, J. S. and Wyatt, M. C.: 2003, MNRAS **345**, 1212

Greenberg, J. M.: 1982, in *IAU Colloq. 61: Comet Discoveries, Statistics, and Observational Selection*, pp 131–163

Greenberg, J. M.: 1998, A&A **330**, 375

Greenberg, J. M. and Hage, J. I.: 1990, ApJ **361**, 260

Habing, H. J., Dominik, C., Jourdain de Muizon, M., Laureijs, R. J., Kessler, M. F., Leech, K., Metcalfe, L., Salama, A., Siebenmorgen, R., Trams, N., and Bouchet, P.: 2001, A&A **365**, 545

Harper, D. A., Loewenstein, R. F., and Davidson, J. A.: 1984, ApJ **285**, 808

Harvey, P. M., Wilking, B. A., and Joy, M.: 1984, Nature **307**, 441

Hatzes, A. P., Cochran, W. D., McArthur, B., Baliunas, S. L., Walker, G. A. H., Campbell, B., Irwin, A. W., Yang, S., Kürster, M., Endl, M., Els, S., Butler, R. P., and Marcy, G. W.: 2000, ApJ **544**, L145

Hayashi, C., Nakazawa, K., and Adachi, I.: 1977, PASJ **29**, 163

Hayashi, C., Nakazawa, K., and Nakagawa, Y.: 1985, in *Protostars and Planets II*, pp 1100–1153

Heap, S. R., Lindler, D. J., Lanz, T. M., Cornett, R. H., Hubeny, I., Maran, S. P., and Woodgate, B.: 2000, ApJ **539**, 435

Heinrichsen, I., Walker, H. J., Klaas, U., Sylvester, R. J., and Lemke, D.: 1999, MNRAS **304**, 589

Hobbs, L. M., Vidal-Madjar, A., Ferlet, R., Albert, C. E., and Gry, C.: 1985, ApJ **293**, L29

Holland, W. S., Cunningham, C. R., Gear, W. K., Jenness, T., Laidlaw, K., Lightfoot, J. F., and Robson, E. I.: 1998a, Proc. SPIE **3357**, 305

Holland, W. S., Greaves, J. S., Dent, W. R. F., Wyatt, M. C., Zuckerman, B., Webb, R. A., McCarthy, C., Coulson, I. M., Robson, E. I., and Gear, W. K.: 2003, ApJ **582**, 1141

Holland, W. S., Greaves, J. S., Zuckerman, B., Webb, R. A., McCarthy, C., Coulson, I. M., Walther, D. M., Dent, W. R. F., Gear, W. K., and Robson, I.: 1998b, Nature **392**, 788

Hollenbach, D. J., Yorke, H. W., and Johnstone, D.: 2000, *Protostars and Planets IV* pp 401–+

Jayawardhana, R., Fisher, S., Hartmann, L., Telesco, C., Pina, R., and Fazio, G.: 1998, ApJ **503**, L79+

Jayawardhana, R., Holland, W. S., Kalas, P., Greaves, J. S., Dent, W. R. F., Wyatt, M. C., and Marcy, G. W.: 2002, ApJ **570**, L93

Jourdain de Muizon, M., Laureijs, R. J., Dominik, C., Habing, H. J., Metcalfe, L., Siebenmorgen, R., Kessler, M. F., Bouchet, P., Salama, A., Leech, K., Trams, N., and Heske, A.: 1999, A&A **350**, 875

Jura, M.: 1991, ApJ **383**, L79+

Kalas, P., Graham, J. R., Beckwith, S. V. W., Jewitt, D. C., and Lloyd, J. P.: 2002, ApJ **567**, 999

Kamp, I. and Bertoldi, F.: 2000, A&A **353**, 276

Kenyon, S. J. and Bromley, B. C.: 2001, AJ **121**, 538

Knacke, R. F., Fajardo-Acosta, S. B., Telesco, C. M., Hackwell, J. A., Lynch, D. K., and Russell, R. W.: 1993, ApJ **418**, 440

Koerner, D. W., Chandler, C. J., and Sargent, A. I.: 1995, ApJ **452**, L69+

Koerner, D. W., Ressler, M. E., Werner, M. W., and Backman, D. E.: 1998, ApJ **503**, L83+

Koerner, D. W., Sargent, A. I., and Ostroff, N. A.: 2001, ApJ **560**, L181

Kondo, Y. and Bruhweiler, F. C.: 1985, ApJ **291**, L1

Krivov, A. V., Mann, I., and Krivova, N. A.: 2000, A&A **362**, 1127

Kruegel, E. and Siebenmorgen, R.: 1994, A&A **288**, 929

Kuchner, M. J. and Holman, M. J.: 2003, ApJ **588**, 1110

Lachaume, R., Dominik, C., Lanz, T., and Habing, H. J.: 1999, A&A **348**, 897

Lagage, P. O. and Pantin, E.: 1994, Nature **369**, 628

Lagrange, A.-M., Beust, H., Mouillet, D., Deleuil, M., Feldman, P. D., Ferlet, R., Hobbs, L., Lecavelier Des Etangs, A., Lissauer, J. J., McGrath, M. A., McPhate, J. B., Spyromilio, J., Tobin, W., and Vidal-Madjar, A.: 1998, A&A **330**, 1091

Lagrange, A. M., Ferlet, R., and Vidal-Madjar, A.: 1987, A&A **173**, 289

Lagrange, A. M., Vidal-Madjar, A., Deleuil, M., Emerich, C., Beust, H., and Ferlet, R.: 1995, A&A **296**, 499

Lang, K. R.: 1992, *Astrophysical Data I. Planets and Stars.*, Springer-Verlag, Berlin Heidelberg New York

Laor, A. and Draine, B. T.: 1993, ApJ **402**, 441

Larwood, J. D. and Kalas, P. G.: 2001, MNRAS **323**, 402

Laureijs, R. J., Jourdain de Muizon, M., Leech, K., Siebenmorgen, R., Dominik, C., Habing, H. J., Trams, N., and Kessler, M. F.: 2002, A&A **387**, 285

Lazzaro, D., Sicardy, B., Roques, F., and Greenberg, R.: 1994, *Icarus* **108**, 59

Lecavelier Des Etangs, A., Perrin, G., Ferlet, R., Vidal Madjar, A., Colas, F., Buil, C., Sevre, F., Arlot, J. E., Beust, H., Lagrange Henri, A. M., Lecacheux, J., Deleuil, M., and Gry, C.: 1993, A&A **274**, 877

Lecavelier Des Etangs, A., Vidal-Madjar, A., and Ferlet, R.: 1996, A&A **307**, 542

Lecavelier des Etangs, A., Vidal-Madjar, A., Roberge, A., Feldman, P. D., Deleuil, M., André, M., Blair, W. P., Bouret, J.-C., Désert, J.-M., Ferlet, R., Friedman, S., Hébrard, G., Lemoine, M., and Moos, H. W.: 2001, Nature **412**, 706

Li, A. and Greenberg, J. M.: 1997, A&A **323**, 566

Li, A. and Greenberg, J. M.: 1998, A&A **331**, 291

Li, A. and Lunine, J. I.: 2003a, ApJ **594**, 987

Li, A. and Lunine, J. I.: 2003b, ApJ **590**, 368

Li, A., Lunine, J. I., and Bendo, G. J.: 2003, ApJ **598**, L51

Lin, D. N. C., Bodenheimer, P., and Richardson, D. C.: 1996, Nature **380**, 606

Liseau, R.: 1999, A&A **348**, 133

Liseau, R. and Artymowicz, P.: 1998, A&A **334**, 935

Lissauer, J. J.: 1993, ARA&A **31**, 129

Lisse, C., Schultz, A., Fernandez, Y., Peschke, S., Ressler, M., Gorjian, V., Djorgovski, S. G., Christian, D. J., Golisch, B., and Kaminski, C.: 2002, ApJ **570**, 779

Mannings, V. and Barlow, M. J.: 1998, ApJ **497**, 330

Mannings, V., Boss, A. P., and Russell, S. S.: 2000, *Protostars and Planets IV*

Mannings, V. and Emerson, J. P.: 1994, MNRAS **267**, 361

Mannings, V. and Sargent, A. I.: 2000, ApJ **529**, 391

Marcy, G. W. and Butler, R. P.: 1998, ARA&A **36**, 57

Marsh, K. A., Silverstone, M. D., Becklin, E. E., Koerner, D. W., Werner, M. W., Weinberger, A. J., and Ressler, M. E.: 2002, ApJ **573**, 425

Mizuno, H.: 1980, *Progress of Theoretical Physics* **64**, 544

Moffat, A. F. J.: 1969, A&A **3**, 455

Moshir, M.: 1989, *IRAS Faint Source Survey, Explanatory supplement version 1 and tape*, Pasadena: Infrared Processing and Analysis Center, California Institute of Technology, 1989, edited by Moshir, M.

Moshir, M., Kopan, G., Conrow, T., McCallon, H., Hacking, P., Gregorich, D., Rohrbach, G., Melnyk, M., Rice, W., Fullmer, L., White, J., and Chester, T.: 1990, BAAS **22**, 1325

Mouillet, D., Lagrange, A. M., Augereau, J. C., and Ménard, F.: 2001, A&A **372**, L61

Mouillet, D., Lagrange, A.-M., Beuzit, J.-L., and Renaud, N.: 1997a, A&A **324**, 1083

Mouillet, D., Larwood, J. D., Papaloizou, J. C. B., and Lagrange, A. M.: 1997b, MNRAS **292**, 896

Nakamura, R. and Hidaka, Y.: 1998, A&A **340**, 329

Natta, A., Prusti, T., Neri, R., Wooden, D., Grinin, V. P., and Mannings, V.: 2001, A&A **371**, 186

Olofsson, G., Liseau, R., and Brandeker, A.: 2001, ApJ **563**, L77

Oudmaijer, R. D., van der Veen, W. E. C. J., Waters, L. B. F. M., Trams, N. R., Waelkens, C., and Engelsman, E.: 1992, A&AS **96**, 625

Ozernoy, L. M., Gorkavyi, N. N., Mather, J. C., and Taidakova, T. A.: 2000, ApJ **537**, L147

Pantin, E., Lagage, P. O., and Artymowicz, P.: 1997, A&A **327**, 1123

Paresce, F. and Burrows, C.: 1987, ApJ **319**, L23

Piétu, V., Dutrey, A., and Kahane, C.: 2003, A&A **398**, 565

Pollack, J. B., Hollenbach, D., Beckwith, S., Simonelli, D. P., Roush, T., and Fong, W.: 1994, ApJ **421**, 615

Przygodda, F., van Boekel, R., Àbrahàm, P., Melnikov, S. Y., Waters, L. B. F. M., and Leinert, C.: 2003, A&A **412**, L43

Quillen, A. C. and Thorndike, S.: 2002, ApJ **578**, L149

Richter, M. J., Jaffe, D. T., Blake, G. A., and Lacy, J. H.: 2002, ApJ **572**, L161

Robberto, M., Meyer, M. R., Natta, A., and Beckwith, S. V. W.: 1999, in *ESA SP-427: The Universe as Seen by ISO*, pp 195–+

Roberge, A., Lecavelier des Etangs, A., Grady, C. A., Vidal-Madjar, A., Bouret, J.-C., Feldman, P. D., Deleuil, M., Andre, M., Boggess, A., Bruhweiler, F. C., Ferlet, R., and Woodgate, B.: 2001, ApJ **551**, L97

Roques, F., Scholl, H., Sicardy, B., and Smith, B. A.: 1994, *Icarus* **108**, 37

Savoldini, M. and Galletta, G.: 1994, A&A **285**, 467

Schneider, G., Smith, B. A., Becklin, E. E., Koerner, D. W., Meier, R., Hines, D. C., Lowrance, P. J., Terrile, R. J., Thompson, R. I., and Rieke, M.: 1999, ApJ **513**, L127

Schweizer, F.: 1979, PASP **91**, 149

Scott, S. E., Fox, M. J., Dunlop, J. S., Serjeant, S., Peacock, J. A., Ivison, R. J., Oliver, S., Mann, R. G., Lawrence, A., Efstathiou, A., Rowan-Robinson, M., Hughes, D. H., Archibald, E. N., Blain, A., and Longair, M.: 2002, MNRAS **331**, 817

Shu, F. H., Adams, F. C., and Lizano, S.: 1987, ARA&A **25**, 23

Shuping, R. Y., Bally, J., Morris, M., and Throop, H.: 2003, ApJ **587**, L109

Smith, B. A. and Terrile, R. J.: 1984, *Science* **226**, 1421

Song, I., Caillault, J.-P., Barrado y Navascués, D., and Stauffer, J. R.: 2001, ApJ **546**, 352

Song, I., Caillault, J.-P., Barrado y Navascués, D., Stauffer, J. R., and Randich, S.: 2000, ApJ **533**, L41

Spangler, C., Sargent, A. I., Silverstone, M. D., Becklin, E. E., and Zuckerman, B.: 2001, ApJ **555**, 932

Stauffer, J. R., Hartmann, L. W., and Barrado y Navascues, D.: 1995, ApJ **454**, 910

Stencel, R. E. and Backman, D. E.: 1991, ApJS **75**, 905

Supulver, K. D. and Lin, D. N. C.: 2000, *Icarus* **146**, 525

Sylvester, R. J., Dunkin, S. K., and Barlow, M. J.: 2001, MNRAS **327**, 133

Sylvester, R. J., Skinner, C. J., Barlow, M. J., and Mannings, V.: 1996, MNRAS **279**, 915

Takeuchi, T. and Artymowicz, P.: 2001, ApJ **557**, 990

Takeuchi, T. and Lin, D. N. C.: 2002, ApJ **581**, 1344

Takeuchi, T. and Lin, D. N. C.: 2003, ApJ **593**, 524

Tanaka, H., Inaba, S., and Nakazawa, K.: 1996, *Icarus* **123**, 450

Telesco, C. M., Fisher, R. S., Piña, R. K., Knacke, R. F., Dermott, S. F., Wyatt, M. C., Grogan, K., Holmes, E. K., Ghez, A. M., Prato, L., Hartmann, L. W., and Jayawardhana, R.: 2000, ApJ **530**, 329

Thébault, P., Augereau, J. C., and Beust, H.: 2003, A&A **408**, 775

Thi, W. F., Blake, G. A., van Dishoeck, E. F., van Zadelhoff, G. J., Horn, J. M. M., Becklin, E. E., Mannings, V., Sargent, A. I., van den Ancker, M. E., and Natta, A.: 2001a, Nature **409**, 60

Thi, W. F., van Dishoeck, E. F., Blake, G. A., van Zadelhoff, G. J., Horn, J., Becklin, E. E., Mannings, V., Sargent, A. I., van den Ancker, M. E., Natta, A., and Kessler, J.: 2001b, ApJ **561**, 1074

Throop, H. B., Bally, J., Esposito, L. W., and McCaughrean, M. J.: 2001, *Science* **292**, 1686

Valenti, J. A., Johns-Krull, C. M., and Linsky, J. L.: 2000, ApJS **129**, 399

van Boekel, R., Waters, L. B. F. M., Dominik, C., Bouwman, J., de Koter, A., Dullemond, C. P., and Paresce, F.: 2003, A&A **400**, L21

van der Bliek, N. S., Prusti, T., and Waters, L. B. F. M.: 1994, A&A **285**, 229

Vidal-Madjar, A., Ferlet, R., Hobbs, L. M., Gry, C., and Albert, C. E.: 1986, A&A **167**, 325

Wahhaj, Z., Koerner, D. W., Ressler, M. E., Werner, M. W., Backman, D. E., and Sargent, A. I.: 2003, ApJ **584**, L27

Walker, H. J. and Heinrichsen, I.: 2000, *Icarus* **143**, 147

Walker, H. J. and Wolstencroft, R. D.: 1988, PASP **100**, 1509

Weidenschilling, S. J.: 1980, *Icarus* **44**, 172

Weinberger, A. J., Becklin, E. E., Schneider, G., Smith, B. A., Lowrance, P. J., Silverstone, M. D., Zuckerman, B., and Terrile, R. J.: 1999, ApJ **525**, L53

Weinberger, A. J., Rich, R. M., Becklin, E. E., Zuckerman, B., and Matthews, K.: 2000, ApJ **544**, 937

Weissman, P. R.: 1984, *Science* **224**, 987

Wilner, D. J., Holman, M. J., Kuchner, M. J., and Ho, P. T. P.: 2002, ApJ **569**, L115

Wolf, S., Gueth, F., Henning, T., and Kley, W.: 2002, ApJ **566**, L97

Wyatt, M. C.: 1999, *Ph.D. Thesis*

Wyatt, M. C.: 2003, ApJ **598**, 1321

Wyatt, M. C. and Dent, W. R. F.: 2002, MNRAS **334**, 589

Wyatt, M. C., Dermott, S. F., Telesco, C. M., Fisher, R. S., Grogan, K., Holmes, E. K., and Piña, R. K.: 1999, ApJ **527**, 918

Yamashita, T., Handa, T., Omodaka, T., Kitamura, Y., Kawazoe, E., Hayashi, S. S., and Kaifu, N.: 1993, ApJ **402**, L65

Zuckerman, B. and Becklin, E. E.: 1993, ApJ **414**, 793

Zuckerman, B., Forveille, T., and Kastner, J. H.: 1995, Nature **373**, 494